FAKULTÄT FÜR MASCHINENWESEN LEHRSTUHL

LEHRSTUHL FÜR AERODYNAMIK UND STRÖMUNGSMECHANIK

Conservative sharp interface methods for incompressible multi-phase flow

Jian Luo

Vollständiger Abdruck der von der Fakultät für Maschinenwesen der Technischen Universität München zur Erlangung des akademischen Grades eines

Doktor-Ingenieurs

genehmigten Dissertation.

Vorsitzender:		Prof. Dr.-Ing. Hans-Jakob Kaltenbach
Prüfer der Dissertation:	1.	Priv.-Doz Dr.-Ing. Xiangyu Hu
	2.	Prof. Dr. Bing Wang
	3.	Prof. Dr.-Ing. Nikolaus A. Adams

Die Dissertation wurde am 24.03.2016 bei der Technischen Universität München eingereicht und durch die Fakultät für Maschinenwesen am 15.06.2016 angenommen.

Declaration

I hereby declare that except where specific reference is made to the work of others, the contents of this dissertation are original and have not been submitted in whole or in part for consideration for any other degree or qualification in this, or any other university. This dissertation is my own work and contains nothing which is the outcome of work done in collaboration with others, except as specified in the text and Acknowledgements.

Jian Luo

24.03.2016

Abstract

This cumulative thesis concerns numerical techniques for incompressible multi-phase flow. Strategies for accurate and robust simulations are suggested. In particular, a conservative sharp interface method is for incompressible flows with viscous and surface tension effects, a curvature boundary condition is for a moving contact line and an efficient formulation of the scale-separation approach for multi-scale modeling of interfacial flow.

In incompressible multi-phase flow, surface tension forces and viscosity forces play important roles. To treat these two forces sharply at the phase interface, I develop a conservative sharp-interface method based on Ref. [37] by employing a weakly compressible model. The method is simple, mass conserving and capable of handling flows with large density and viscosity ratios and high surface tension. Since the viscosity jump at the material interface is directly imposed by an interface-flux term, momentum conservation is ensured regardless of capillary effects. Furthermore, a subcell-resolution method for volume-fraction evaluation is developed to achieve accurate interface reconstruction. A number of two and three dimensional numerical examples, are considered to demonstrate that the present method is able to simulate a wide range of flow problems with good robustness and high accuracy.

When the interface of two immiscible fluids meets a solid wall, a fundamental difficulty in the numerical treatment of the contact line arises with the conventional no-slip boundary condition, as it leads to inconsistent, grid-dependent results. In this thesis, we present a curvature boundary condition to circumvent the difficulties of previous approaches on explicitly imposing the contact angle and with respect to mass-loss artifacts near the wall boundary. While employing the asymptotic theory of Cox for imposing an effective curvature directly at the wall surface, the present method avoids a mismatch between the exact and the numerical contact angles. Simulations on drop spreading and multi-phase

flow in a channel show that the present method achieves grid-convergent results and ensures mass conservation, and delivers good agreement with theoretical, numerical and experimental data.

Another difficulty encountered with multi-phase method is multi-scale problem, especially in the drop breakup or splash, where the involving length scales can span at least several orders. To separate the scales and then treat them differently, we propose an efficient formulation of the scale-separation approach which has been developed by Han et al. [24] based on the level-set technique. Instead of shifting the entire level-set field twice as in the original method, the improved method identifies the non-resolved interface structures from two auxiliary level-sets close to the interface. Non-resolved structures are separated from the interface by a localized re-distancing method, which increases the computational efficiency considerably compared to the original global reinitialization procedure. Several tests for two-phase flow problems, involving simple and complex interface structures, are carried out to show that the present method maintains sharper interface structures than the original method, and achieves effective scale-separation.

Kurzfassung

Diese kumulative Dissertation betrifft numerische Verfahren für inkompressible Mehrphasenströmungen. Strategien für die genaue und robuste Simulationen werden vorgeschlagen. Insgesamt werden ein konservatives scharfes Schnittstellenverfahren für inkompressible Strömungen mit viskosen und Oberflächenspannungseffekte, eine Krümmungsbegrenzungsbedingung für eine bewegete Kontaktlinie und eine effiziente Formulierung des Skalentrennungs Ansatz für die mehrskalige Modellierung des Grenzflächenstroms präsentiert.

In inkompressiblen Mehrphasenströmung, spielen Oberflächenspannungskäfte und Viskositätskräfte eine wichtige Rolle. Um diese beiden Kräfte scharf an der Phasengrenzfläche zu behandeln, wird eine konservative scharfe Interface-Methode basiered auf Referenz [37] unter eine schwach komprimierbaren Modell entwickelt. Das Verfahren ist einfach, Masse erhaltend und in der Lage Ströme mit hohen Dichte und Viskositäts Verhältnissen und hohen Oberflächenspannungen zu handeln. Da der Viskositätsprung an der Materialschnittstelle direkt über einen schnittstellefluss augepräst wird, wird die Impulserhaltung gewährleistet trotz der Kapillarwirkung. Des Weiterhin wird ein Subzellenauflösungsverfahren für die Volumenfraktionauswertung entwickelt, um eine genaue Rekonstruktion der Schnittstelle zu erreichen. Eine Reihe von zwei- und dreidimensionalen numerischen Beispielen werden präsentiert, dass die vorliegende Methode in der Lage ist, um einen weiten Bereich von Strömungsproblemen mit guter Robustheit und hohe Genauigkeit zu simulieren. Wenn die Grenzfläche von zwei unmischbaren Flüssigkeiten auf eine feste Wand trifft, ergibt sich eine grundlegende Schwierigkeit bei der numerischen Behandlung der Kontaktlinie mit der herkömmlichen haftbedingung. Es führt zu inkonsistenten, Gitter abhängigen Ergebnissen. In dieser Dissertation, stellen wir eine Krümmungs Randbedingung, die Schwierigkeiten früherer Ansätze auf ausdrücklich zur Einführung des Kontaktwinkels und in Bezug auf Massenverlust Artefakte in der nähe der Wand

Grenze umzugehen. Das vorliegende Verfahren vermeidet eine Diskrepanz zwischen dem exakten und dem numerischen Kontaktwinkel. Simulationen Tropfenverteilung und Kanalmehrphasenströmung zeigen, dass das vorliegende Verfahren netzkonvergente Ergebnisse erreicht und die Massenerhaltung gewährleistet. Es liefert eine gute Übereinstimmung mit den theoretischen, numerischen und experimentellen vergleichdaten. Eine weitere Schwierigkeit die bei Mehrphasenferfahren auftritt ist das Multiskalenproblem. Um die Waage zu trennen und sie dann anders zu behandeln, schlagen wir eine effiziente Formulierung des Scale-Trennung Ansatzes von Han et al. [24] auf der Grundlage der Level-Set-Technik. Anstatt das gesamte Level-Set-Feld doppelt zu verschieben, wie identifiziert das verbesserte Verfahren die nicht aufgelöste Schnittstellenstrukturen von zwei zusätzliche Level sets nahe der Schnittstelle. Nichtaufgelöster Strukturen werden von der Grenzfläche durch eine lokales Neudistanzierungsverfahren getrennt, was die Recheneffizienz deutlich gegenüber dem ursprünglichen globalen Reinitialisierungverfahren erhöht. Mehrere Tests für Zweiphasenströmungsprobleme, einfacher und komplexer Schnittstellenstrukturen, werden um zu zeigen durchgeführt, dass das vorliegende Verfahren schärfere Grenzfläche Strukturen aufrechterhält als das ursprüngliche Verfahren und wirksame Skalen-Trennung erzielt.

Acknowledgements

I am very grateful for the opportunity I have been given to do PhD studies at the Institute of Aerodynamics and Fluid Mechanics, Technische Universität München (TUM). I also wish to express my sincere gratitude to the Chinese Scholarship Council (CSC) for their financial support of my studies in Germany.

I would like to thank my supervisor PD Dr. Xiangyu Hu for his constant support throughout my graduate studies. He was very patient to introduce and teach me various numerical schemes pertaining to multi-phase flows. His advices and constructive criticism helped me all the time to solve the confusions and break the difficulties. His good research habits and accurate and strict research attitude set an example for my future research.

I am also very grateful to Prof. Dr. Nikolaus A. Adams for having been my co-advisor, who listened to research progress and provided useful suggestions at weekly group meetings. As the institute director, he also made much efforts to provide me many facilities. Without him this work would have been difficult to complete.

My gratitude extends to all my colleagues in the Institute of Aerodynamics and Fluid Mechanics, especially Dr. K. K. So, Luhui Han, Lin Fu, Shucheng Pan, Felix Schranner. They offered heartfelt help and showed their kindness when I discussed with them. I will miss the group meeting on Thursday and Friday. I like that kind of discussion environment.

I'm particularly thankful for the support of my friends here in München. My life has been rich because of the great friends I have made and sustained during my time in graduate school. I would cherish our friendships in my whole life.

Lastly, I would like to thank my parents, my sister and my grandparents for their constant support and encouragement. Their loves are my strongest motivation! I also want to give many thanks to my wife Dr. Zhen Bi. Her seriousness of life and support gave me a lot of confidence.

Table of contents

Nomenclature

Notation

CFL Courant-Friedrich-Lewy

CLSVOF Coupled level-set and volume of fluid method

CSIM Conservative sharp-interface method

DIM Diffuse-interface method

NS Navier–Stokes equation

PDE Partial differential equation

PF phase field method

RK Runge-Kutta method

SIM Sharp-interface method

TVD Total variation diminishing

VOF volume of fluid method

WENO Weighted essentially non-oscillatory

Dimensionless groups

Ca Capillary number

Oh Ohnesorge number

Re	Reynolds number
We	Weber number

Greek Symbols

α	Volume fraction
δ	Dirac delta function
Γ	Phase interface
ι	Fictitious time
κ	Curvature
μ	Viscosity
Ω	Flow domain
ρ	Density
σ	Surface tension
θ_e	Static contact angle
θ_m	Macroscopic angle contact angle
θ_m	Microscopic angle contact angle
φ	Level-set value

Chapter 1

Introduction

1.1 Multi-phase flow problem

Multi-phase flow research is an important topic, which has directed towards the understanding of the phenomena occurring in a wide range of industrial applications. Examples include jet coating, ink jet printing, lab-on-a-chip devices, and liquid phase sintering. Fig. 1.1 shows a typical process of jet coating, where a jet exits the nozzle orifice, breaks into a small droplet, and then it impacts a solid surface and spreads to thin coat. This process involves some fundamental challenges in the simulation, such as filament breakup, droplet generation and moving contact line

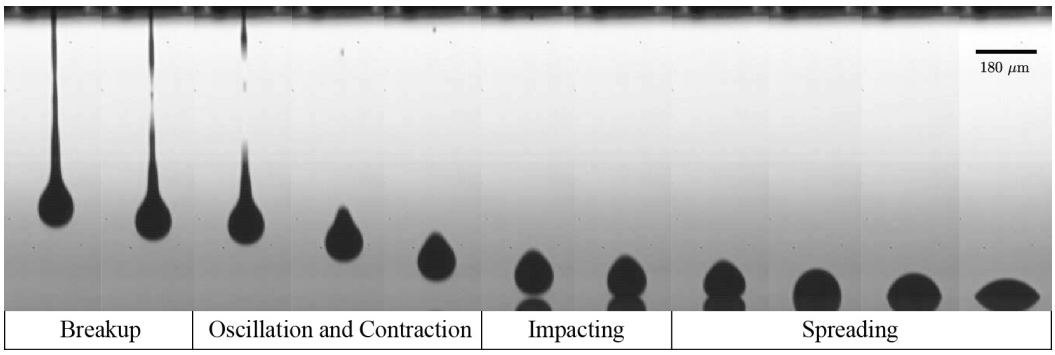

Fig. 1.1 The process of jet coating, taken from Bolleddula [3].

In the breakup of a liquid filament, Surface-tension forces and viscous forces play important roles, where the interface evolution is governed by the competition between these two forces [87]. The relative importance of surface tension and viscosity can be expressed through the Ohnesorge

number $Oh = \mu\sqrt{\rho\sigma R}$, where μ, ρ, and σ are the viscosity, density, and surface tension of the liquid, respectively, and R denotes the radius of the filament. Whether the filament condenses into the main drop, or breaks up into satellite drops can be predicted from the aspect ratio and Ohnesorge number [8, 32]. Fig. 1.2 shows examples of typical liquid filaments with a range of different aspect ratios. In each case, the evolution of the filaments is illustrated with a serial of images. The shortest filaments always condensed into single drops for all values of Oh, while for the highest values of Oh, the filaments never broke up regardless of their aspect ratio. Therefore, accurate treatments of surface tension forces and viscous forces, especially at the phase interface, are required to capture these subtle behaviors.

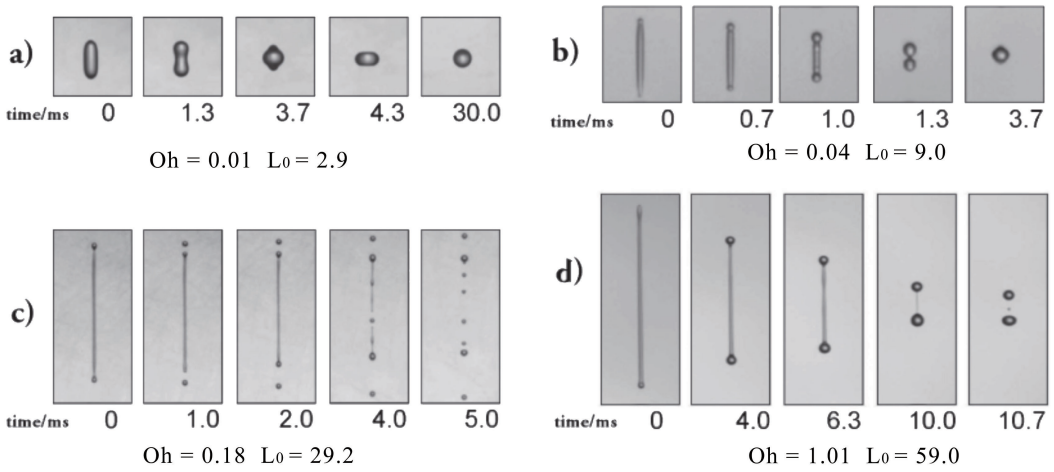

Fig. 1.2 Breakup of liquid filaments, taken from Castrejón-Pita et al. [8].

The behavior of drops impacting on a solid surface can be characterized into three main modes: deposition, bouncing and splashing [3]. The experiments of Rioboo et al. revealed the possible outcomes of drop impact on a dry wall, including three main modes and three otherwise transition modes [59], as shown in Fig. 1.3. These various modes come from the interactions of initial drop speed, ambient pressure, wall surface roughness, drop viscosity and surface tension. The hydrodynamics of this problem has been widely studied, both experimentally [52] and theoretically [4]. One of challenges in these phenomena is the treatment of moving contact line and dynamic contact angle. Several theoretical models [13, 63] and empirical models [18, 67] have been proposed and compared well with experiment. However, a fundamental difficulty in the numerical treatment of the contact line arises when confronted with the conventional no-slip boundary condition, as it leads to inconsistent,

grid-dependent results [21, 72]. Hence, a special treatment of interface at the vicinity of moving contact line is needed to tackle this problem.

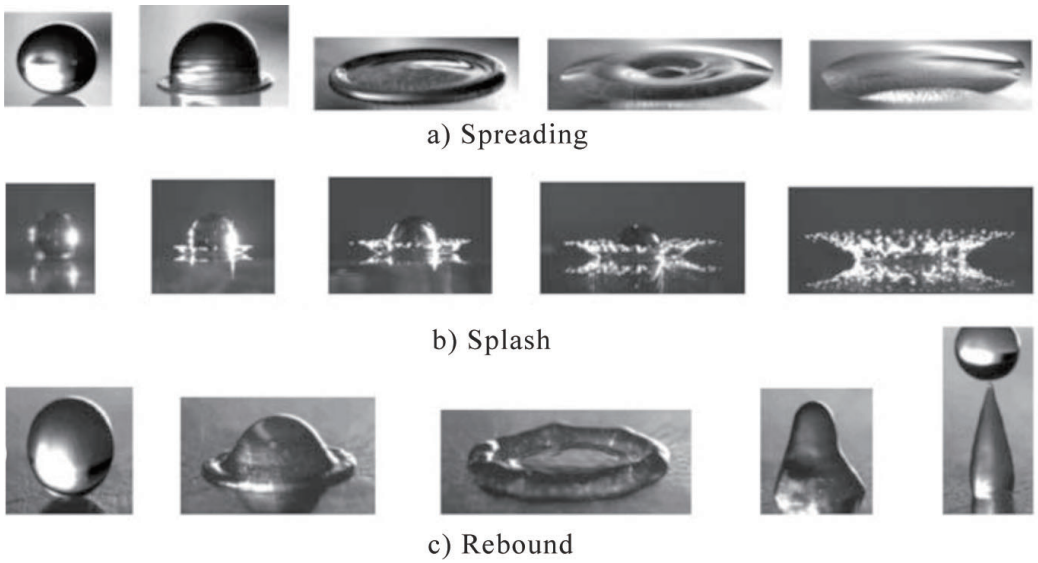

Fig. 1.3 Morphology of drop impact on a solid surface, taken from Rioboo et al. [59].

Another issue associated with drop generation, such as filament breakup (e.g. Fig. 1.2c) and drop splash (e.g. Fig. 1.3c), is the multi-scale problem. One need to resolve length scales that can span at least several orders, which poses a great computational challenge. Adaptive mesh refinement [45] and multi-resolution methods [23, 26], even with local time stepping, do not sufficiently reduce computational cost to enable accurate routine simulations of complex interfacial flows. A promising approach is to separate them from the current spatial resolution and treat them differently, e.g. structures smaller than the given grid size (referred to as unresolved structures) can be separated and converted into Lagrangian particles. Therefore, the scheme associated with scale separation should be built to identify and separate unresolved interface structures.

1.2 Phase-interface representation

The representation and evolution of the phase-interface is essential to the numerical simulation of multi-phase flow involving immiscible phase-interfaces. Existing interface representation techniques can essentially be divided into two classes, namely interface-tracking methods and interface-capturing methods.

In interface-tracking, interfaces are represented explicitly, e.g. front tracking methods [82, 83] and marker methods [64, 81]. These methods can efficiently locate the interface position by interface markers or track the moving boundary by adjusting the position of the nodes on the interface. However, they encounter difficulties for large interface deformations and topology changes, and require a special treatment of the interface marker distribution when the interface is stretched.

In interface-capturing, there is no explicit representation of the interface, but the location of the interface is represented implicitly by a scalar field, e.g. volume of fluid method (VOF) [31], phase field (PF) method [39] and level-set method [55]. Compared to the interface-tracking methods these methods handle topological changes such as merging and breaking natrually. All such changes can be captured by a continuous evolution of the scalar function defining the interface implicitly.

In VOF method, a volume of fluid function gives the volume fraction of each fluid in every computational cell. The cells that are intersected by the interface will have a volume fraction between zero and one. The main advantage of VOF methods is the exact conservation of mass when computing incompressible flow. One main drawback of VOF methods is the smearing of the interface by the numerical diffusion, which is due to the use of total-variation-diminishing (TVD) schemes [25] to preserve the volume-fraction boundedness (for the step-profile of volume fraction at the interface). Furthermore, computations of accurate normal and curvature approximations are not straightforward.

The PF method is based on fluid free energy, where a conserved order parameter or phase-field is introduced to characterize the two different phases. This order parameter changes rapidly but smoothly in the thin interfacial region and is mostly uniform in the bulk phases. Analog to the VOF method, the interfacial location is defined between the contour levels of this order parameter. The interface is updated by the Cahn–Hilliard equation [7]. This equation involving fourth-order derivatives with respect to the order parameter, makes its numerical treatment more complex as compared to the Navier–Stokes (NS) equation which involves only second-order derivatives. Another issue with the PF method is the resolution of the interface thickness, which usually spans several grid cells.

The level-set method is one of non-smeared interface-capture methods. A signed-distance function (level-set function) specifies the distance of a discretization point to a nearby interface. Hence the interface is defined sharply by the zero-level-set of this function. From the level-set function the curvature of the interface and the surface tension can be calculated with high accuracy. However, a

main drawback of the level-set method is lack of discrete conservation. Various attempts are applied to improve the mass conservation in the level-set method. For example, Sussman et al. constrain the interface during the reinitialization procedure to conserve the volume bounded by the zero-level-set [75]. However, the mass enclosed by the zero level-set is not conserved in the advection step. Several hybrid methods have also been developed with the aim of improving the mass conservation, such as the particle level-set method [16, 85], and the coupled level-set and volume of fluid method (CLSVOF) [46, 77]. While these approaches increase the computational complexity, and compromise the simplicity of the pure level-set method, especially in three dimensions. A conservative level-set based sharp-interface method was introduced by Hu et al. [37], where the underlying conservative scheme on a Cartesian grid is modified for computational cells that are cut by the interface. To ensure numerical stability for small cells, a conservative mixing procedure is proposed to redistribute the flux to neighbour cells, which avoids an unstructured mesh near the interface. This method is simple for implementation and extension to higher dimensions, which is hence used and further developed in this thesis.

1.3 Objective

After choosing the representation of the phase-interface, it is followed by the corresponding methods to handle the specific phenomena at the interface, such as computations of the velocity and the pressure at the phase-interface (referred to a interface interaction), the treatment of moving contact line and the scheme of scale separation.

In general, there are two established approaches for modeling interface interactions, the diffuse-interface method (DIM) and the sharp-interface method (SIM). With the diffuse-interface method the interface is represented by an artificial region with limited thickness, where the transition from one phase to the other is smooth. While the diffuse-interface methods are conceptually simple, the artificial mixing region may generate nonphysical artifacts, such as parasitic flows near a static interface by surface tension and wrongly predicted instability growth rates of viscous interfacial flow. With the sharp-interface method, the interface as well as the interface interactions are all localized at the infinitely thin interface. Various SIMs have been proposed, as reviewed in Paper I, but they

have more or less deficiencies and limitations, such as complexity, no mass conservation and difficult extension to three dimensions. Therefore, we develop a conservative sharp-interface method (CSIM) based on [37] for incompressible multi-phase flows by employing a weakly compressible model. The viscosity jump at the material interface is directly imposed by an interface-flux term, and the pressure jump due to surface tension is imposed consistently after solving the constrained Riemann problem. Moreover, the extension to three dimensions is straightforward.

When the interface of two immiscible fluids meets a solid wall, a difficulty associated with contact line appears in simulations, i.e. the consistency with the conventional no-slip boundary condition. Various approaches have been proposed to alleviate this problem, as summarized in Paper II. The efficient approaches are to model the microscopic region near the contact line based on hydrodynamic theories and to resolve only the macroscopic region away from the contact line. Grid-independent results have been obtained by using Cox's theory [13] to built the relationship between microscopic angle to the macroscopic angle. However, a complex, implicit integral function should be solved in Cox's theory, which is either replaced by a simplified form or obtained numerically. Moreover, imposing the contact angle explicitly can spuriously displace the zero level-set and the location of contact line, and thus induce large mass-conservation errors. To overcome these problems, we impose a curvature boundary condition for predicting moving contact line, where the effective curvature is formulated explicitly based on the asymptotic theories of Cox.

Small scales and non-resolved interface segments are generated during filament breakup or drop splash. To avoid resolving the entire range of length scales, an effective approach is to separate them from well-resolved field and treated them individually. To author's knowledge, only two approaches have been proposed: one is based on the refined level-set grid method [29], the other is the constrained stimulus–response procedure [24]. As pointed out in Paper III, the first one has low efficiency, because it requires a two-grid system to check non-resolved cells. The second method separate resolved and non-resolved interface segments upon different responds when they are subjected to small shifts of the level-set field. Though this procedure is effective, shifting the level-set and re-initialization twice in the entire field are quite time consuming, especially when the non-resolved interface structures compose only very small portion of the entire interface. To speed up the procedure of scale separation,

we propose an efficient multi-scale model to avoid shifts of the level-set and additional re-initialization operations.

This work focus on tackling above challenges in numerical simulation of incompressible multi-phase flow, specifically, the treatments of surface tension and viscosity, moving contact line and scale separation. The new methods should have lower computational cost and higher accuracy than those currently available proposed strategies. Accurate simulations can contribute to understanding of the phenomena occurring in multi-phase flow, and hence to the improvement of flow control in engineering.

The following chapter gives an introduction to the present CSIM as well as the level-set method for phase-interface representation. Chapter 3 first gives a short literature review and then summaries the present methods on each problem, including a CSIM for incompressible multi-phase flow, a curvature boundary condition for moving contact line and efficient implementation of scale separation for multi-scale modeling. Finally, Chapter 4 makes a conclusion on the state of proposed methods.

Chapter 2

Conservative sharp-interface method

The CSIM is formulated following a standard finite volume approach, in which the underlying finite-volume scheme operating on a Cartesian grid is modified by considering computational cells being cut by the interface. The level-set approach is the method of choice here to capture the interface, since it allows for an easy and straightforward calculation of the geometrical properties of the interfaces, and it handles topology changes of the interface automatically. A main drawback of the level-set method is the lack of discrete conservation properties, which has been overcome by combining with the finite volume approach [37]. An essential key of this method is to handle the cut cells, such as interface flux in cut cells, curvature in cut cells, small and empty cut cells, volume fraction of cut cells and non-resolved cut cells.

2.1 Governing flow Equations

In multi-phase problems, the flow field of each phase is updated separately with the standard finite volume approach. For incompressible flows, a weakly compressible model is employed, where an explicit link between pressure and density is established other than solving for the Poisson equation for the pressure. Weighted essentially non-oscillatory scheme (WENO) [41] is applied to flux reconstruction, and TVD Runge-Kutta scheme [68] is used for time integration.

2.1.1 Finite volume method for multi-phase flow

For the weakly compressible model the governing equations can be written as

$$\frac{\partial \mathbf{U}}{\partial t} + \nabla \cdot \mathbf{F} = \nabla \cdot \mathbf{F}_v + \mathbf{a}_s, \tag{2.1}$$

where $\mathbf{U}$ is the density of mass and momentum; $\mathbf{F}$ represents the convective fluxes, and $\mathbf{F}_v$ the viscous fluxes. Note that the right-hand side of Eq. (2.1) vanishes when it represents the continuity equation. The surface-tension force is given by

$$\mathbf{a}_s = \sigma \kappa \delta \mathbf{N} \tag{2.2}$$

where σ, κ, $\mathbf{N}$ are surface tension, curvature and normal direction of the interface, respectively. δ_n is the Dirac delta distribution

$$\delta(x) = \begin{cases} +\infty & \varphi = 0 \\ 0 & \varphi \neq 0 \end{cases}, \quad \int_{-\infty}^{+\infty} \delta(x) dx = 1, \tag{2.3}$$

defined in the normal direction of the interface.

The flow domain Ω is divided by a time-dependent interface Γ into two sub-domains Ω^1 and Ω^2, which denote the regions occupied by $fluid1$ and $fluid2$, as shown in Fig. 2.1. We solve Eq. (2.1) for each fluid in respective its sub-domain $\Omega^m (m = 1,2)$, as in Hu et al. [37], on a two-dimensional collocated Cartesian grid with spacing Δx and Δy. Integrating Eq. (2.1) over a computational cell and applying the Gauss's theorem yields

$$\begin{aligned} &\int_n^{n+1} dt \int_{\Delta_{i,j} \bigcap \Omega^m} dxdy \frac{\partial \mathbf{U}}{\partial x} + \int_n^{n+1} dt \int_{\partial(\Delta_{i,j} \bigcap \Omega^m)} dxdy \mathbf{F} \cdot \mathbf{n} \\ &= \int_n^{n+1} dt \int_{\partial(\Delta_{i,j} \bigcap \Omega^m)} dxdy \mathbf{F}_v \cdot \mathbf{n} + \int_n^{n+1} dt \int_{\Delta\Gamma_{i,j}} dxdy \mathbf{F}_s \cdot \mathbf{n}, \end{aligned} \tag{2.4}$$

where $\Delta_{i,j} = \Delta x \Delta y$ is the cell volume; $\Delta_{i,j} \bigcap \Omega^m$ can be represented as $\alpha_{i,j} \Delta_{i,j}$, where $\alpha_{i,j}$ is the time dependent volume fraction of fluid m and satisfies $1 \geq \alpha \geq 0$. $\partial(\Delta_{i,j} \bigcap \Omega^m)$ denotes the faces of cell i, j wetted by fluid m, including the interface segment contained in the cell, and $\mathbf{F}_s$ is an additional flux at the interface due to surface tension. The surface of $\partial(\Delta_{i,j} \bigcap \Omega^m)$ with normal direction $\mathbf{n}$

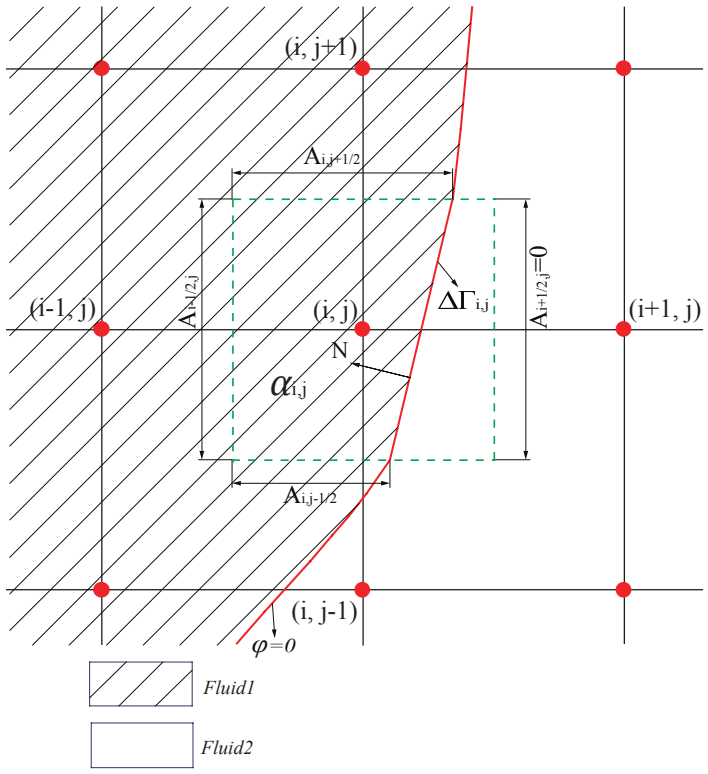

Fig. 2.1 Schematic of discretization for a cut cell (i, j) on a collocated grid: the red dot indicates the cell center, the red line indicates the interface, the green dash line indicates the cell face, $\alpha_{i,j}$ denotes the volume fraction occupied by $fluid1$ in cut cell (i, j), A denotes the cell-face aperture, N is the normal direction of the interface and $\Delta\Gamma_{i,j}$ the segment of the interface.

can be represented by two parts. One part is the combination of four segments (2D) of the cut cell faces, which can be written as $A_{i+1/2,j}\Delta y, A_{i,j+1/2}\Delta x, A_{i-1/2,j}\Delta y$ and $A_{i,j-1/2}\Delta x$, where $1 \geq A \geq 0$ is the time-dependent cell-face aperture. The second, denoted as $\Delta\Gamma_{i,j}$, is the segment of the interface Γ inside of cell (i, j). For simplicity, a typical discretization with explicit first-order forward time difference (see Sec. 2.1.4 for the higher-order scheme) of Eq. (2.4) can be written in the following form,

$$\begin{aligned}
\alpha_{i,j}^{n+1}\mathbf{U}_{i,j}^{n+1} = \alpha_{i,j}^{n}\mathbf{U}_{i,j}^{n} &+ \frac{\Delta t}{\Delta x \Delta y}\left[\hat{\mathbf{X}}\left(\Delta\Gamma_{i,j}\right) + \hat{\mathbf{X}}_{v}\left(\Delta\Gamma_{i,j}\right) + \hat{\mathbf{X}}_{s}\left(\Delta\Gamma_{i,j}\right)\right] \\
&+ \frac{\Delta t}{\Delta x}\left[A_{i-1/2,j}\hat{\mathbf{F}}_{i-1/2,j} - A_{i+1/2,j}\hat{\mathbf{F}}_{i+1/2,j}\right] \\
&+ \frac{\Delta t}{\Delta y}\left[A_{i,j-1/2}\hat{\mathbf{F}}_{i,j-1/2} - A_{i,j+1/2}\hat{\mathbf{F}}_{i,j+1/2}\right] \\
&+ \frac{\Delta t}{\Delta x}\left[A_{i-1/2,j}\hat{\mathbf{F}}_{vi-1/2,j} - A_{i+1/2,j}\hat{\mathbf{F}}_{vi+1/2,j}\right] \\
&+ \frac{\Delta t}{\Delta y}\left[A_{i,j-1/2}\hat{\mathbf{F}}_{vi,j-1/2} - A_{i,j+1/2}\hat{\mathbf{F}}_{vi,j+1/2}\right],
\end{aligned} \tag{2.5}$$

where Δt is the time step size. $\mathbf{U}_{i,j}$ denotes cell-averaged density of conservative quantities of mass and momentum of the considered fluid, and $\alpha_{i,j}\mathbf{U}_{i,j}$ are the conservative quantities in the cut cell. $\hat{\mathbf{X}}$ is the average inviscid momentum flux across the interface, and $\hat{\mathbf{X}}_\nu$ denotes the momentum flux due to viscous force. $\hat{\mathbf{X}}_s$ is the momentum flux due to the interfacial pressure jump induced by surface tension. The detailed formulation of these interface fluxes $(\hat{\mathbf{X}}, \hat{\mathbf{X}}_\nu, \hat{\mathbf{X}}_s)$ is presented in Paper I.

For a small cut cell or an empty cell, i.e. $\alpha < 0.5$, a stable fluid state may be unobtainable based on the time step calculated according to the full grid size Courant-Friedrich-Lewy (CFL) condition. A mix procedure is introduced to mix the conservative quantities with their neighbors [37]. The exchanges of the conservative quantities are calculated according to the averaged values in mixing operations. Then the conservative quantities for one fluid in the near interface cells are updated by

$$\alpha_{i,j}^{n+1}\mathbf{U}_{i,j} = \left(\alpha_{i,j}^{n+1}\mathbf{U}_{i,j}\right)^* + \sum \mathbf{M}, \tag{2.6}$$

where $\left(\alpha_{i,j}^{n+1}\mathbf{U}_{i,j}\right)^*$ is the conservative quantities at time step $n+1$ before mixing, and the second term on the right hand side represents the sum of all mixing operations on cell (i, j). Note that conservation is maintained since the conservative quantities in a small cell obtained from a target cell corresponds to a loss of its neighboring cell. The extension of Eq. (2.5) to three dimensions is straightforward.

2.1.2 Equation of state

To close the governing equations, one should relate the pressure and density. If incompressibility is strictly required, the Poisson equation is commonly solved, which is rather time-consuming. Here, we employ a weakly compressible model for incompressible multi-phase flows with sacrificing little incompressibility, where an explicit link pressure and density is established. Such model is widely used, e.g. with smoothed particle hydrodynamics (SPH) [33, 47] and the lattice Boltzmann method [11]. Moreover, the weakly compressible model has been applied recently for a systematic study of the coarse-grained prediction for a range of turbulent and non-turbulent incompressible flows [66].

In the present implementation, we use the Tait's equation that enforces very low density variation and is efficient to compute [12]. Tait's equation has the form

$$\begin{aligned} p &= B[(\frac{\rho}{\rho_0})^{\gamma} - 1] + p_0 \\ B &= \frac{\rho_0 |v_f|^2}{\gamma M^2} \end{aligned}, \tag{2.7}$$

where ρ_0 and p_0 are the density and pressure of fluids at the reference condition, respectively. γ is artificial specific heat ratio. For the liquid-gas system, typical adopted values are $\gamma_l = 7.15$ and $\gamma_g = 1.4$, respectively. The parameter B governs the density fluctuation $|\Delta\rho|/\rho$ with $\Delta\rho = \rho - \rho_0$. As known that, the density variation in fluid flow is $\propto M^2$, where M is Mach number, which results in the following relation,

$$\frac{|\Delta\rho|}{\rho} \propto \frac{|v_f|^2}{c_s^2} \tag{2.8}$$

where v_f denotes an expected order of magnitude of the fluid velocity for the consider problem, c_s is the artificial sound speed in the fluid, $c_s = \sqrt{\frac{\gamma B}{\rho}}$. Typically, the density variation is allowed with the order of 1%. The parameters γ, B and ρ_0 are chosen to ensure that the Mach number satisfies $M = \frac{|v_f|}{c} \approx 0.1$.

2.1.3 Numerical flux reconstruction

The numerical fluxes, convective flux $\hat{\mathbf{F}}$ and diffusive flux $\hat{\mathbf{F}}_v$ in Eq. (2.5), are calculated separately. In two dimensions they can be written as

$$\begin{aligned} \hat{\mathbf{F}} &= \begin{pmatrix} \rho(\mathbf{v}\cdot\mathbf{n}) \\ \rho u(\mathbf{v}\cdot\mathbf{n}) + p n_x \\ \rho v(\mathbf{v}\cdot\mathbf{n}) + p n_y \end{pmatrix}; \hat{\mathbf{F}}_v = \begin{pmatrix} 0 \\ -\tau_{xx} n_x + \tau_{xy} n_y \\ -\tau_{xy} n_x + \tau_{yy} n_y \end{pmatrix}; \mathbf{n} = n_x\mathbf{i} + n_y\mathbf{j}; \mathbf{v} = u\mathbf{i} + v\mathbf{j}; \\ \tau_{xx} &= \mu\left(\frac{4}{3}\frac{\partial u}{\partial x} - \frac{2}{3}\frac{\partial v}{\partial y}\right); \tau_{xy} = \tau_{yx} = \mu\left(\frac{\partial u}{\partial y} - \frac{\partial v}{\partial x}\right); \tau_{yy} = \mu\left(\frac{4}{3}\frac{\partial v}{\partial y} - \frac{2}{3}\frac{\partial u}{\partial x}\right) \end{aligned}, \tag{2.9}$$

where $\mathbf{n}$ is unit (outward) normal on the cell face, $\mathbf{v}$ is the fluid velocity and τ the viscous stress.

Since the governing equations (2.4) are a system of conservation laws, the convective fluxes $\hat{\mathbf{F}}$ can be approximated using WENO methodology. Specifically, the Roe approximation is used for the

characteristic decomposition at the cell faces, the Lax-Friedrichs formulation is used for the numerical fluxes. To achieve very small numerical dissipation relative to original WENO scheme, Hu et al. [38] proposed an adaptive central-upwind weighted essentially non-oscillatory scheme. Such scheme adapts between central and upwind schemes smoothly by a new weighting relation based on blending the smoothness indicators of the optimal higher order stencil and the lower order upwind stencils.

In order to construct the appropriate diffusive flux function, we need the values of τ_{xx}, τ_{xy} and $\mathbf{v}$ at the cell faces which are center between the grid points. First the higher order centered difference is applied to calculate the u_x, u_y, v_x, v_y at the cell center with the neighboring grid points, and then using the arithmetic average to define viscous stresses at the cell faces.

2.1.4 Temporal discretization

To advance the governing equations in time, a temporal discretization is needed. A common way is to discretize with respect to the spatial variables, and then combine the semi-discretization with standard time discretization methods. When the flow is truly transient, flow characters changes rapidly over time. Explicit time discretization schemes are popular alternatives to solving these cases other than the implicit method. Moreover, it is relatively easy to construct schemes of higher-order. To improve the numerical stability, the total variation diminishing (TVD) Runge-Kutta method is chosen for temporal discretization [68]. Such scheme guarantees that no spurious oscillations are produced as a consequence of the higher-order accurate temporal discretization as long as no spurious oscillations are produced.

There are certain limitations for the size of the time step, when an explicit method is used. When the time step is too large, numerical instabilities occur. Defining a fixed time step in the beginning of a numerical simulation bears the danger of either chosen a too small time step, which weighs heavy on the computational resources. Or the time step is too large, resulting in a diverging solution. The most efficient solution is to use adaptive time-stepping. Here the maximum values for the velocities, the viscosity and the volume and surface forces are calculated at each time step. With this information, the size of the next time step is determined. The time-step is set according to [77],

$$\Delta t = CFL \cdot \min\left(\frac{\Delta x}{|u^n| + c^n}, \frac{\rho^n \Delta x^2}{\mu}, \sqrt{\frac{\rho^n}{8\pi\sigma}}\Delta x^{\frac{3}{2}}\right), \tag{2.10}$$

where c^n is the artificial sound speed at time step n. We set CFL$=0.6$ for all our simulations.

2.2 Level-set method

The LS method is chosen to represent the phase-interface for its simple and strong capability of handing large interface deformations and topological changes. The location of interface is represented implicitly by the zero level-set, and a Hamilton-Jacobi equation is solved for updating the implicit interface. The volume fraction, interface segment and cell-aperture in Eq. (2.5) can be reconstructed from the level-set function. The interface curvature can be obtained directly from the level-set function as well, except for the cut cell containing a contact line.

2.2.1 Level-set function

The level-set function, φ, which describes the signed distance from the interface to each cell center, is used to track the interface. The zero-level set, i.e. $\varphi = 0$, represents the interface Γ, and the phases are distinguished by the change of the sign. That results in following properties,

$$\varphi(\vec{x},t) = \begin{cases} > 0 & \text{if } \vec{x} \in \text{Phase1}, \\ = 0 & \text{if } \vec{x} \in \Gamma, \\ < 0 & \text{if } \vec{x} \in \text{Phase2}, \end{cases} . \tag{2.11}$$

The level-set field is advanced by [17]

$$\frac{\partial \varphi}{\partial t} + \mathbf{u} \cdot \nabla \varphi = 0, \tag{2.12}$$

where $\mathbf{u}$ represents the velocity for the level-set obtained with the interface interaction model [35]. The spatial derivatives are approximated by an upwind method based on the sign of $\mathbf{u}$. At each grid point, define φ_x^- as a backward difference and φ_x^+ as a forward difference. If $u_i > 0$, approximate φ_x with φ_x^+. If $u_i < 0$, approximate φ_x with φ_x^-. When $u_i = 0$, the $u_i(\varphi_x)$ term vanishes, and φ_x does not need to be approximated.

Practical experience suggests that level-set methods are sensitive to spatial accuracy [53], implying that the high-order accurate WENO method is required to get a more accurate approximation for φ_x^- and φ_x^+. And a 2nd-order TVD Runge–Kutta scheme is preferred for temporal discretization to obtain accurate numerical solutions.

When the interface evolves under the external velocity field the level-set function can become irregular and loose its signed distance property. In order to avoid this, the level-set function needs to be reinitialized. The reinitialization needs to reset the level-set function without actually changing the location of the interface. Here, a partial differential equation (PDE) based reinitialization equation is solved [17],

$$\frac{\partial \varphi}{\partial \iota} + \mathrm{S}(\varphi)\,(\varphi)\,(|\nabla \varphi| - 1) = 0, \tag{2.13}$$

where $\mathrm{S}(\varphi)$ is the smoothed sign function by Peng et al. [56],

$$\mathrm{S}(\varphi) = \frac{\varphi}{\sqrt{\varphi^2 + |\varphi_\mathrm{x}|^2(\Delta \mathrm{x})}}. \tag{2.14}$$

The signed distance property is recovered by solving Eq. 2.14 until steady, where ι is fictitious time, such as $\Delta \iota = dx/2$.

2.2.2 Volume fraction of cut cell

With the standard level-set technique, the volume fraction $\alpha_{i,j}^+$ for the phase corresponding to $\varphi > 0$ can be estimated by a smoothed Heaviside function $\alpha_{i,j}^+ = H(\varphi, \varepsilon)$ where ε is a tunable parameter that determines the size of the bandwidth of numerical smearing [76]. And the volume fraction $\alpha_{i,j}^-$ for the phase corresponding to $\varphi > 0$ can be calculated by the relation by $\alpha_{ij}^- = 1 - \alpha_{i,j}^+$. According to volume fraction, the cells can be classified into three types: cells with volume fraction larger than 0.5 are normal cells, cells with volume fraction less than 0.5 but non-zero are small cells, and otherwise they are empty cells. As addressed in Sec. 2.1.1, a mix procedure is introduced to maintain the stability when updating the small cells or empty cells.

To obtain accurate volume fraction, Lauer et al. [42] employed the marching-square approach to determine the interface topology. Although 16 cases exist in $2D$, there are 256 cases when extending it to $3D$ by the corresponding way, marching cubes [44]. They are complex and computationally costly

due to the necessity of identifying the correct topology, especially with the presence of ambiguous topology.

To overcome this difficulty, a subcell-resolution interface-reconstruction scheme is proposed in Paper I, which avoids complex case-selections for identifying the topology of the interface, and its extension to $3D$ is straightforward.

2.2.3 Interface curvature

The interface curvature in a cut cell is defined by $\kappa = \nabla \cdot \left(\frac{\nabla \varphi}{|\nabla \varphi|} \right)$, which can be rewritten, in three dimension, as

$$\begin{aligned} \kappa = & \frac{\varphi_{xx} + \varphi_{yy} + \varphi_{zz}}{\left(\varphi_x^2 + \varphi_y^2 + \varphi_z^2 + \varepsilon\right)^{1/2}} \\ & - \frac{\varphi_x^2 \varphi_{xx} + \varphi_y^2 \varphi_{yy} + \varphi_z^2 \varphi_{zz} + 2\left(\varphi_x \varphi_y \varphi_{xy} + \varphi_x \varphi_z \varphi_{xz} + \varphi_y \varphi_z \varphi_{yz}\right)}{\left(\varphi_x^2 + \varphi_y^2 + \varphi_z^2 + \varepsilon\right)^{3/2}}, \end{aligned} \tag{2.15}$$

where ε is a small positive number to avoid division by zero [61]. Note that the curvature in two dimensions is obtained by setting all derivatives with subscript z to zero. Since all the partial derivatives in Eq. (2.15) are usually computed at the cell center with standard central difference schemes, the curvature κ is estimated at the cell center. Therefore, this value is corrected for the distance of the cell center from the interface by approximating the interface locally by a circle or sphere in Paper I.

A difficulty arises with the presence of the contact line at the solid wall. The curvature at the contact line cannot be obtained directly through Eq. (2.15), since the stencil of central differences for the cell adjacent to the wall would contain ghost cells in the wall. Close to the contact line, the balance between viscous stresses and capillary forces primarily determines the interface profile. The curvature at the contact line should be reconstructed to respect above balance. Cox [13] provides a general hydrodynamic description of a moving contact line, where the interface profile presents a logarithmic dependence on the Capillary number. Therefore, an effective curvature is estimated based on the asymptotic theory of Cox in Paper II, where the moving of the contact line is attributed to the updating of the level-set field.

2.2.4 Non-resolved cut cell

Another issue associated with multi-phase flow is the non-resolved interface problems, because it manifest singularities at the interface, which may give rise to errors for calculating volume fractions and interface curvatures. For a given spatial resolution with the grid size h, the phase-interface segments with magnitude of η can be categorized into resolve ones by $\eta > h$ and non-resolved ones by $\eta < h$. As shown in Fig. 2.2(a), the cells marked by blue stars are non-resolved cut cells due to the corresponding scale smaller than a grid size. An effective approach is to separate them from well-resolved field, otherwise the error of estimating these geometry properties would lead to erroneous or even numerically unstable simulations. Fig. 2.2(b) shows the reconstructed interface after filtering the non-resolved cut cell. It is found that there are singularities at the interface, the geometry properties are can be estimated from the level-set function again.

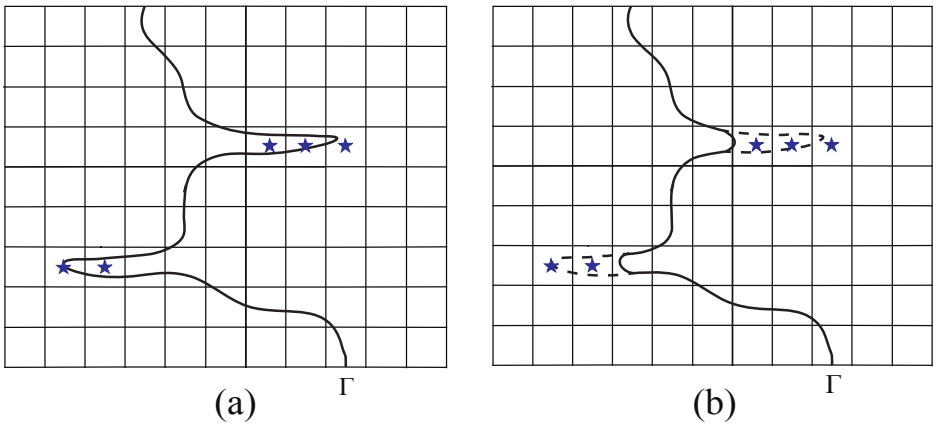

Fig. 2.2 Identification of the non-resolved cut cells in two dimensions: (a) the initial interface with non-resolved cut cells (blue stars); (b) interface reconstruction (dash line) by filtering non-resolved cut cells.

Non-resolved interface segments are often presented as drops and thin filaments with length scale close to the grid size h. In the level-set field, they take a common property that is lack of consistency among the level-sets near the interface. Such property is corresponding to the large discrepancies that induced by the non-resolved interface segments when subjected to a small shift of the level-set field. With this observation, Han et al. [24] established a relationship that allows for identifying non-resolved interface segments from their response to a small constant shift of the level-set, called "stimulus". Scale separation is achieved implicitly and efficiently by incorporating a stimulus-response

operation into the process of level-set reinitialization. Due to sign-dependence of the procedure for identification of all non-resolved interface segments, two stimuli in opposite directions are required. Obviously, shifting the level-set and re-initialization twice in the entire field are quite time consuming, especially when the non-resolved interface structures compose only very small portion of the entire interface. To speed up the procedure of scale separation, an efficient multi-scale model is presented in Paper III, where a criterion is established to identify the non-resolved interface structures.

Chapter 3

Accomplishments

In this chapter, the extension of the conservative sharp-interface method to incompressible multi-phase flows and its application for moving contact line are presented. In multi-phase flows, each fluid has individual density and viscosity, and surface tension forces act at the interfaces. In paper I, we proposed a sharp-interface method to treat the viscous forces and surface tension forces sharply at the interface. Paper II is concerned with mesh convergency in the simulation of moving contact line problems. An issue appears when applying conventional no-slip boundary conditions at the vicinity of the contact line, which leads to grid-dependent simulation results, i.e. dependent on the grid sizes. A curvature boundary condition is proposed to overcome this problem. Another issue associated with multi-phase flows is the multi-scale problem, which gives rise to erroneous or even numerically unstable simulations. An efficient approach for the multi-scale problems is to separate the scales and then treat them differently. In Paper III, the original scale separation method is developed to improve the computational efficiency.

3.1 A conservative sharp interface method for incompressible multi-phase flow

The treatment of surface tension forces and viscous forces at the interface is essential of simulation of incompressible multiphase flow problems. Here, we give an overview of some existing numerical methods, and then summarize the proposed method in Paper I.

3.1.1 State of the art

Surface tension forces and viscous forces often play important roles in many natural phenomena and engineering processes. For example, in the deformation of liquid drop in shear flow, the details of liquid shape is governed by the capillary force [69], and during the liquid filament contracting, whether it separates into satellite drops or condenses into a single drop depends on the Ohnesorge number [8]. An accurate approximation of them is essential for simulations of multi-phase flow problems. How this force is modeled and approximated strongly influences the quality of the approximation of the velocity field and the pressure, especially in the problems involving large density and viscosity ratios and high surface tension. In general, there are two developed approaches: one is the DIM; the other is the SIM.

With the DIM, an artificial mixture or smeared zone close to the interface is created, where the transition from one phase to the other is smooth. For the material properties, such as viscosity and density, are treated by the use of smooth functions in the mixture zone, which can be represented as a volume fraction [31] or a Heaviside-function [78]. For imposing surface tension at the interface, a widespread used approach is the continuum surface force method [5], where the surface tension is regularized by a delta function obtained from the volume fraction or a smooth Heaviside function [78] and as a source term in the Navier–Stokes equations. While the diffuse-interface methods are conceptually simple, the smoothed zone may be prone to generate nonphysical flows, especially in surface tension dominated flows [40, 64] or viscous dominated flows [49, 50].

With the SIM, the representation of interface and interface interactions are both treated in a sharp way. Various approaches have been developed to obtain a sharp interface representation. Examples of such approaches include arbitrary Lagrangian Eulerian methods [30] where the interface is a coordinate line which evolves and deforms at the local flow velocity, front-tracking method [83] and marker method [64] in which the interface can be explicitly capture by interface markers, and the level-set method [78] where the interface is defined as the zero contour of a signed-distance function.

The level-set method is a simple interface capturing method and possesses strong capability of handling large interface deformations and topological changes in a straightforward way [54]. A main drawback of the level-set method is lack of discrete conservation, many attempts therefore have been

proposed to remedy it. Some hybrid methods, such as the particle level-set method [16, 85] and the CLSVOF [46, 77] have been developed. While these approaches increase computational complexity they also compromise the simplicity of the pure level-set method. To avoid being coupled with other method, Glimm [20] introduced a conservative method based on a grid intersection technique with the assumption of no topological change in the solution. A fully conservative level-set method for compressible flows capable of dealing with topological interface changes was introduced by Hu et al. [37]. In this method the underlying conservative scheme on a Cartesian grid is modified for computational cells that are cut by the interface.

Moreover, sharp-interface methods require fully coupled treatments of surface tension and viscous forces at the interface singularity. With the interest of applying the singular surface tension force at the interface, Sussman [79] treated it as a Dirichlet boundary condition when solving the two-domain pressure-Poisson equation. Flowing the ghost fluid method, Bo [2] modeled the surface tension as a pressure jump in Riemann problems. Nourgaliev at al. [49] modeled surface-tension and viscous-stress for incompressible flows by applying jump conditions at the interface for density, viscosity and pressure. However, discrete mass conservation is not ensured in these methods. A mass conservative sharp-interface method by employing an unstructured mesh near the interface has been developed by Chang et al. [10]. While this method has been demonstrated to be accurate and efficient for computing surface tension and viscous forces for two-dimensional problems, an extension to three dimensions may, however, be challenging, especially when the interface and thus also the unstructured meshes becomes very complex, as in most practical applications.

3.1.2 Summary of the presented method

In Paper I, we develop a conservative sharp interface method based on [37] for incompressible flows with viscous and surface tension effects. Employing a weakly compressible framework, the method is simple, mass conserving and capable of handling flows with large density and viscosity ratios and high surface tension. Moreover, both surface tension and viscous forces are treated sharply at the interface.

For viscous stress at the interface, the present method imposes the viscosity jump directly on the momentum flux across the interface. Based on two assumptions: (a) in a neighborhood of the

interface the velocity distribution is linear within each fluid; (b) the viscous stress is continuous at the interface, an effective viscosity in the cut cell is provided via harmonic mean with respect to the volume fractions of the two fluids. As now we can obtain viscous stress directly from the velocity difference across the interface. Since the viscosity jump is imposed at the interface directly on the momentum flux across the interface, momentum conservation and the ability of handling large viscosity ratios are ensured. The extension to three dimensions is straightforward.

For surface tension, a constrained Riemann problem is solved to impose the pressure jump at the interface. Combining with the effective viscosity by assuming continuous viscous stress across the interface, the surface tension effect contributes to the pressure jump at the interface only. The interface pressures for individual fluids and the interface velocity are all obtained by solving the constrained Riemann problem. Then, the interfacial momentum flux is ensured. The present approach also applies to a free surface boundary, just assuming that one fluid is subjected to the free surface condition. Note that, due to the non-conservative form of the surface-tension model, the implementation of pressure jump does not satisfy momentum conservation. However, since the present formulation is based on a conservative sharp-interface method, it maintains the so called zero-order consistency.

In addition, a subcell-resolution scheme by refining the cut cell recursively is used to improve the accuracy of calculating cell-face aperture and volume fraction. First, cut cells are divided into two types: simple-interface cells in which the interface is a single connected patch, and complex-interface cells in which the interface possibly has multiple unconnected patches, e.g. the cell is cut by the interface more than one time. A complex-interface cell is identified by checking the inconsistency of the local-gradient estimations of the level-set at the cell center, obtained by forward and by backward differences. A complex-interface cell is refined recursively into subcells until each subcell is a simple-interface cell or the relative error reaches a certain threshold. Subsequently, the volume fraction and apertures on the original cut cell are computed by combining the results from all subcells.

The viscosity model is validated through a typical case of shear flow with two viscous horizontal fluid layers. Comparisons with the exact solution show that the present method predict agreement velocity profile of the fully developed flow, even when a sharp kink appears at the interface. A static drop in equilibrium is considered to validate the proposed surface tension model, the errors between the prediction and exact solution takes nearly second-order accuracy with mesh refinement. The

oscillation of a drop under surface tension allows to access the prediction of capillary instabilities, the error of the predicted oscillation period is much smaller than that reported in [57]. To access the capability of handling coupled effects of viscosity and surface tension, a drop deforming in a Couette shear flow is simulated. The obtained results are in good agreement with those in Hu et al. [36] and Zhou et al. [90]. The simulation of two-fluid Poiseuille flow illustrates the great capability of predicting the instabilities in the linear range as well as in the non-linear region. The last test is the liquid filament contraction and breakup, which is simulated to assess the capability of the present method for three dimensional configurations with coupled effects of viscosity and surface tension. The obtained results are in very good agreement with the experiment [8] and previously published data [48].

My contribution to this work was the development of the method and the corresponding computer code for its implementation. I performed simulations and analyzed the results, and wrote the manuscript for the publication.

3.2 Curvature boundary condition for a moving contact line

Simulation of flow involving a contact line moving along a no-slip solid surface is complicated, which are prone to generate grid-dependent simulation results when encountered with the conventional no-slip boundary condition. Here, we give an overview of some existing numerical methods to overcome this difficulty, and then summarize the proposed method in Paper II.

3.2.1 State of the art

An interface separating two fluids may also be in contact with a solid surface where the liquid wets the solid surface. The line where the interface separating the two fluids intersects the solid surface is called the contact line. If we consider a liquid drop on a solid substrate, there are three different phases present. Therefore, there are three surface tensions that need to be considered: solid-liquid, liquid-gas, and solid-gas. For the equilibrium drop, it respects the Young's equations, however, the difficulties arise when subjected to the moving contact line. There are two fundamental difficulties in the numerical treatment of the contact line [21]. The first is associated with the conventional

no-slip boundary condition, which leads to, i.e. dependent on the grid sizes. The second is due to the resolution challenge on describing the near-wall phase-interface profile.

To obtained grid-independent simulation results various approaches are proposed, such as the slip model [80], the precursor film model [63], the diffusive interface model [89], and the multi-scale model combing molecular dynamics and diffusive interface [58]. Whether getting grid-convergent results or nor is related to respective prescribed parameters in above models, e.g. slip length in the slip model, film thickness in the precursor film model and interfacial thickness in the diffusive interface model. In order to obtain mesh convergency results, the mesh grid should reach specific length scale corresponding to prescribed parameters. With the framework of the slip model, the grid size should be smaller than the introduced slip length. In practical, slip length is usually inferred to be of nano-meter scale, however, using extremely fine meshes could require enormous computational resource [15].

To solve the flows with moving contact lines with reasonable mesh grids, the microscopic region is usually modeled based on hydrodynamic theories, which circumvents extremely small mesh grid to obtain grid-independent simulation results. Schönfeld and Hardt [65] obtained almost mesh independent results in the case of capillary rise by combined model with a macroscopic slip and a localized close to the contact line, where such body force is inferred from the hydrodynamic theory in the microscopic region. Similar mesh-independent results are obtained in [1] of Afkhami and Zaleski by modeling the dynamic contact angle based on an analog to Cox's theory, where the applied contact angle boundary condition is presented as a function of mesh size. Sui and Spelt [74] extended this method to cover viscous and inertial regimes by considering higher-order terms in Cox' theory. One difficulty of such methods based on Cox's theory is to solve the complex, implicit integral function relating the microscopic angle to the macroscopic angle, which is either replaced by a simplified form [1, 15] or resorted to numerical approaches [74].

The phase-interface near wall at the contact line should be specified to compute the curvature. In numerical simulations, imposing an apparent contact angle is a common way to define the interface in the vicinity of the contact line [88]. Afkhami reconstructed a height function at the contact line based on the contact angle to estimate the curvature of the interface for their VOF [1]. Also, in Sui's mesh convergent approach, an iterative procedure is used to impose the contact angle for their level-set method [74]. However, imposing a contact angle can move the contact line from its previous

position, which may violate the conservation of mass and lead to parasitic currents. To remedy artificial movement of the contact line, Spelt [71] and Walker [84] proposed to track the contact line explicitly, and Rocca [60] applied a modified reinitialization routine for the level-set based on the Hamilton-Jacobi equation in the vicinity of the contact line.

3.2.2 Summary of the presented method

In Paper II, we present a curvature boundary condition for simulating multi-phase flow involving moving contact line. To obtain mesh convergency results, the microscopic region near the contact line is modeled based on Cox's theory as that of [74]. Differently, an effective curvature is formulated explicitly based on the asymptotic theories of Cox [13], which avoids solving the complex, implicit integral function. Meanwhile, no artificial moving of the contact line occurs, so the conservation of mass is ensured.

The fluid fields is updated by the conservative sharp interface method in Paper I. For the boundary condition of fluid field at the solid in the presence of moving contact line, the conventional no-slip boundary condition is applied without any modification. The phase-interface is captured by the level-set method for its simplicity of handling large interface deformations and topological changes. Within a level-set framework, the interface curvature in a cut-cell far away from the moving contact line can be obtained directly from the level-set function. However, the curvature cannot be obtained directly from the level-set function at the contact line, since the level-set functions are not defined therein when using the central differences. Alternatively, the curvature in a cut-cell with moving contact line is provided by the curvature boundary condition

This effective curvature at moving contact line is formulated based on the asymptotic theories of Cox [13]. Close to the contact line, the balance between viscous stresses and capillary forces primarily determines the interface profile. Cox provides a general hydrodynamic description of a moving contact line, where the interface profile presents a logarithmic dependence on the Capillary number (Ca). Hence, we could define a macroscopic contact angle at a small height above the wall. The average curvature in the cut cell with contact line can be estimated based on this macroscopic contact angle. Finally, the relationship between the curvature and Cox's theory is established, where an extra-curvature is introduced into the original curvature. If the contact line reaches an static

equilibrium, this extra-curvature vanishes. It is possible to extend the curvature boundary condition to axisymmetry and three dimensions, where an addition curvature should be provided, i.e. radial curvature in axisymmetry and planar curvature in three dimensions.

The equilibrium shape of a water drop on a wall is first considered demonstrating the capabilities of the presented method for static contact angle problems. In the absence of gravity, the simulation recover the theory that the equilibrium shape of the water drop is a circular cap respecting the preset static contact angle at the wall [14]. Furthermore, in the presence of gravity the simulation results are in good agreement with the asymptotic solutions, where the shape of the water drop is determined by a balance between surface tension and gravity [14]. Then we perform two channel flows involving two immiscible fluids, displacement flow and couette flow. To check the spatial convergence of present method, the computational domain is discretized with increasing resolutions. The temporal evolution of the interface profile suggest about second-order convergency with mesh refinement. In the case of displacement flow in a channel, there is almost no visible difference between the present result and theoretical predication. Moveover, several cases with various viscosity ratios are conducted to manifest the performance merits, where the effective curvature can be formulated explicitly and avoids solving the integral function and determining the inverse function. Finally, we conduct a numerical simulation of the drop spreading in axisymmetric coordinates and compare the simulation results with experiments to validate the present method. The simulation is in agreement with the experiment [91]. And the mesh convergence test shows that the computed wetting length agrees well with Tanner's law. The presence of a little discrepancy prompts us to built a model for the microscopic contact angle in the future. In addition, the mass conservation is validated in this case.

My contribution to this work was the development of the method and the corresponding computer code for its implementation. I performed simulations and analyzed the results, and wrote the manuscript for the publication.

3.3 Efficient formulation of scale separation for multi-scale modeling

Small scales and non-resolved interface segments are generated during the interface evolution, and are prone to introduce numerical fluctuations in calculation of the geometry properties and to yield

inaccurate results due to the scale-dependent dynamics. Therefore, an effective approach is to separate them from well-resolved field and treated them individually. Here, we give an overview of some existing numerical methods on scale separation, and then summarize the proposed method in Paper III.

3.3.1 State of the art

There is a growing interest to accurately model and simulate multi-phase flow phenomena. Phenomena such as shock bubble interaction [37], drop impact [19] and spray atomization [6, 29] require handling of a wide range of physical scales in numerical simulation, which poses a great challenge to resolve all the length scales. Even adaptive mesh refinement [45] and multi-resolution [23, 26] are not able to tackle for expensive computational cost. Another issue associated with multi-scale problems due to scale-dependent dynamics implies very different physical phenomena acting at different length scales [34]. For example, a pressure disturbance propagates across a large scale with pure-material sound speed but small scale with a mixture sound speed. The underlying mechanism depends on whether there is local mechanical non-equilibrium (microscopic view with resolved interface), mechanical equilibrium (macroscopic view with unresolved interface) or thermodynamic equilibrium (macroscopic view with miscible interface) between the two fluids. Therefore, an efficient approach for the multi-scale problems is to separate the scales and then treat them differently.

With the sharp interface methods [17, 37], accurate modeling of interface interaction is important. To estimate the states of fluids at the interface, the geometrical parameters, such as normal direction, curvature and volume fraction is essential. For a given spatial resolution with the grid size h, the phase-interface segments with magnitude of η can be categorized into resolve ones by $\eta > h$ and non-resolved ones by $\eta < h$. In presence of non-resolved interface segments, the reconstruction of these parameters would fail based on the given grid resolution. To to overcome this difficulty, there are two established approaches to separate resolved and non-resolved interface segments: one is based on a Refined level-set grid method [27–29]; the other is the constrained stimulus-response procedure [24]. In the Refined level-set grid method, the level-set equations are solved on a separate, refined grid, compared to the resolution grids for fluids. The scale separation is achieved by checking the difference of volume fractions measured on a coarse grid and a refined grid, respectively [34].

The refinement-based method, however, requires refined resolution for the level-set, which increases computational cost as well as coding complexity.

With the constrained stimulus-response procedure scale separation is achieved on the same resolution grids as fluids. As pointed out in [24], resolved and non-resolved interface segments act differently when they are subjected to a small constant shift of the level-set. Based on this observation separation of these scales can be achieved through a stimulus-response operation during level-set re-initialization. Though this procedure is effective, shifting the level-set and re-initialization twice in the entire field are quite time consuming, especially when the non-resolved interface structures compose very small portion of the entire interface. Moreover, the smoothing effect of the interface is associated with a criterion defined in constrained re-initialization, where this criterion is formulated to select the anchored and unanchored cells to avoid undesirable displacements of well-resolved interface segments.

3.3.2 Summary of the presented method

In Paper III, we modify the stimulus-response procedure to improve the computational efficiency. The non-resolved interface structures are identified by examining the consistency between the auxiliary and zero level-sets, and the resolved structures are separated by a localized re-distance approach to avoid the entire-field operation of the re-initialization.

In the level-set field, non-resolved interface segments are often presented as drops and thin filaments, which take a common property that is lack of consistency among the level-sets near the interface. Such property is corresponding to the large discrepancies that induced by the non-resolved interface segments when subjected to a small shift of the level-set field. With this observation, we establish a criterion to identify under-resolvable interface segments from the well-resolved ones. First, we sketch two auxiliary level-sets, and then define two types of cut cells associated with such auxiliary level-sets: positive auxiliary cut cells intersected by the positive auxiliary level-set and negative auxiliary cut cells intersected by the positive one. The cut cell associated with non-resolved interface segments can be identified by checking the auxiliary cut cells in its neighborhood. In the monotonic region where the interface is well resolved, there are both positive and negative auxiliary cut cells in

their nearest neighbors. For the cut cell associated with the non-resolvable interface segment, there is only either positive or negative auxiliary cut cell in its nearest neighbors.

After the cut cells containing non-resolved interface segments are identified, one should assign a reasonable level-set value for these cells to remove all the non-resolved structure and reconstruct a well-resolved interface around the non-resolved region. Here, the level-set value of these cut cells are estimated directly from a re-distance method. First, the cut cells who contain non-resolved interface segments are classified into two categories according to the type of auxiliary cut cells in its neighborhood. Then the level-set value of cut cells that contain non-resolved interface segments can be simply estimated based on the minimum distance to the corresponding auxiliary level-sets. We calculate all the distance to the corresponding auxiliary cut cells and choose a minimum one as the level-set value of this cut cell. When the level-set value of all non-resolved cut cell are resetted, the non-resolved structures are filtered out and a well-resolved interface is obtained. Note that the present method does not apply level-set shifting and re-initialization in the entire level-set domain as in [24], it increases the computational efficiency considerably. Meanwhile, a specific criterion to select the anchored and unanchored cells for the constraint re-initialization is not needed with the absence of re-initialization.

A canonical advection test of a circle in a single vortex flow is carried out to exam the smoothing effect of the present method on the interface as well as computational cost. Compared with scale separation procedure in [24], not only more interface segments are remained, but also the present method achieve a speed up of 2.3 times on scale separation. To demonstrate that the present method has no effect on the well-resolved interface structure, we carry out a two-dimensional simulation of an underwater explosion. The simulation results are the same with those in [23]. Compared with the results obtained without scale separation, no interface segments is removed due to the well-resolved interface. To validate the present method on handling the complex interface, we consider a shock bubble interaction problem. The results are in good agreement with previous numerical work of [23, 51, 62, 70] and the experiment [22]. To verify mesh convergency of the present method, we consider a case of liquid filament break-up under the gravity and capillary effects. This problem has been studied both experimentally [9, 86] and numerically [24, 57, 73]. The simulation results

suggests at least second order convergency with mesh refinement. Furthermore, the results recovers the expected potential flow scaling law [43].

My contribution to this work was the development of the method and the corresponding computer code for its implementation. I performed simulations and analyzed the results, and wrote the manuscript for the publication.

Chapter 4

Conclusions

In this work, three numerical methods are developed to tackle several issues in numerical simulations of incompressible multi-phase flow. A conservative sharp interface method is used to deal with the viscous forces and surface tension forces sharply at the interface. A curvature boundary condition is presented for simulating multi-phase flow problems with moving contact line. In addition, an efficient formulation is developed to separate non-resolved interface segments of the multi-scale problem.

Employing a weakly compressible framework, the original conservative interface method is developed for incompressible flows. Since the method is constructed based on its compressible version, the original conservative interfacial-flux formulation and simplicity are maintained. By a subcell-resolution method for evaluating the volume fraction and cell face aperture of computational cell cut by interface, the accuracy of interface reconstruction is ensured without resorting to complex and consuming operations for identifying ambiguous topologies. Moreover, it contributes to the numerical stability. The viscous stress at the interface is directly imposed on the interfacial-flux to ensure conservative of momentum by a simple formulation of effective viscosity. The pressure jump due to surface tension is imposed consistently after solving the constrained Riemann problem. While the numerical results of a number of validation tests show that the method is robust, accurate, and capable of handling large density and viscosity ratios and high surface tension, the simulations of extensive two- and three-dimensional example problems compared with experiments or previous results suggest that the method can be applied to a large range of flow problems.

Based on the asymptotic theory of Cox, a curvature boundary condition is derived for simulating multi-phase flow problems with moving contact line. The curvature is explicitly defined and valid for variable viscosity ratios. Furthermore, since the present method does not prescribe the value of the contact angle explicitly, the contact-line evolution is determined by the flow field directly, and artifacts by mass-conservation errors are avoided. The numerical model has been tested by comparison with analytical solutions, previous numerical simulations or experiments for several typical problems, including the equilibrium shape of a drop on a wall, displacement flow in a channel, Couette flow in a channel and drop spreading on a wall. The simulation results show that the present method leads to grid-convergent results and ensures mass conservation. Furthermore, while the simulation with the present method is in good agreement with experimental data and theory.

We have developed a new formulation for scale separation to improve the computational efficiency for multi-scale sharp interface modeling of multi-phase flows. Based on the observation that there is lack of topological consistency between the auxiliary and zero level-sets for the non-resolved interface segments, the cut cell associated with non-resolved interface segments are identified explicitly by checking the auxiliary cut cells in its neighborhood. Non-resolved structures are removed and the corresponding level-set field is reconstructed by a localized re-distancing method. Several typical numerical examples are simulated to validate the performance of the present scale separation method. The results show that the current approach is able to handle complex interface evolution. Compared to Han et al. [24], the present method decreases the over-smoothing effect of the original method and achieves a considerable computational speed up. Furthermore, the simulations of the filament-breakup case on with increasing grid resolutions verifies the physical consistency of the present scale-separation method.

Combining these methods together, the new conservative sharp interface method is already successfully applied to challenging problems, such as liquid filament contraction and breakup or predicting the interfacial instabilities involving Rayleigh–Taylor and viscous Kelvin–Helmholtz flows. However, some problems are still open. As pointed out in Paper II, a small discrepancy presents in comparison to the experiment, because the microscopic contact angle is simply set to the constant static angle. In fact, the microscopic angle rather varies with capillary number and kinetic energy dissipation, For the further improvement, a model for the microscopic contact angle are required as well as to

consider contact angle hysteresis. In addition, as stated in Paper III, the non-resolved interface segments are simply deleted after they are identified by a scale separation procedure. Actually, a model should be built to handle these segments, including the evolution of them, interaction with resolved interface and collision between each other.

References

[1] Afkhami, S., Zaleski, S., and Bussmann, M. (2009). A mesh-dependent model for applying dynamic contact angles to VOF simulations. *Journal of Computational Physics*, 228(15):5370–5389.

[2] Bo, W., Liu, X., Glimm, J., and Li, X. (2011). A robust front tracking method: Verification and application to simulation of the primary breakup of a liquid jet. *SIAM Journal on Scientific Computing*, 33(4):1505–1524.

[3] Bolleddula, D., Berchielli, A., and Aliseda, A. (2010). Impact of a heterogeneous liquid droplet on a dry surface: Application to the pharmaceutical industry. *Advances in colloid and interface science*, 159(2):144–159.

[4] Bonn, D., Eggers, J., Indekeu, J., Meunier, J., and Rolley, E. (2009). Wetting and spreading. *Reviews of Modern Physics*, 81(2):739–805.

[5] Brackbill, J., Kothe, D. B., and Zemach, C. (1992). A continuum method for modeling surface tension. *Journal of computational physics*, 100(2):335–354.

[6] Bremond, N. and Villermaux, E. (2006). Atomization by jet impact. *Journal of Fluid Mechanics*, 549(-1):273.

[7] Cahn, J. W. and Hilliard, J. E. (1958). Free energy of a nonuniform system. i. interfacial free energy. *The Journal of chemical physics*, 28(2):258–267.

[8] Castrejon-Pita, A. A., Castrejon-Pita, J. R., and Hutchings, I. M. (2012). Breakup of liquid filaments. *Physical Review Letters*, 108(7):074506. PRL.

[9] Castrejón-Pita, J. R., Castrejón-Pita, A. A., Hinch, E. J., Lister, J. R., and Hutchings, I. M. (2012). Self-similar breakup of near-inviscid liquids. *Physical Review E*, 86(1):15301.

[10] Chang, C.-H., Deng, X., and Theofanous, T. G. (2013). Direct numerical simulation of interfacial instabilities: A consistent, conservative, all-speed, sharp-interface method. *Journal of Computational Physics*.

[11] Chen, S. and Doolen, G. D. (1998). Lattice boltzmann method for fluid flows. *Annual review of fluid mechanics*, 30(1):329–364.

[12] Colagrossi, A. and Landrini, M. (2003). Numerical simulation of interfacial flows by smoothed particle hydrodynamics. *Journal of Computational Physics*, 191:448–475.

[13] Cox, R. G. (1986). The dynamics of the spreading of liquids on a solid surface. Part 1. Viscous flow. *Journal of Fluid Mechanics*, 168:169–194.

[14] Dong, S. (2012). On imposing dynamic contact-angle boundary conditions for wall-bounded liquid–gas flows. *Computer Methods in Applied Mechanics and Engineering*, 247-248:179–200.

[15] Dupont, J.-B. and Legendre, D. (2010). Numerical simulation of static and sliding drop with contact angle hysteresis. *Journal of Computational Physics*, 229(7):2453–2478.

[16] Enright, D., Fedkiw, R., Ferziger, J., and Mitchell, I. (2002). A hybrid particle level set method for improved interface capturing. *Journal of Computational Physics*, 183(1):83–116.

[17] Fedkiw, R. P., Aslam, T., Merriman, B., and Osher, S. (1999). A non-oscillatory eulerian approach to interfaces in multimaterial flows (the ghost fluid method). *Journal of Computational Physics*, 152(2):457–492.

[18] Fries, N. and Dreyer, M. (2008). The transition from inertial to viscous flow in capillary rise. *Journal of colloid and interface science*, 327(1):125–128.

[19] Fuster, D. and Agbaglah, G. (2009). Numerical simulation of droplets, bubbles and waves: state of the art. *Fluid dynamics research*, 41(6):065001.

[20] Glimm, J., Li, X., Liu, Y., Xu, Z., and Zhao, N. (2003). Conservative front tracking with improved accuracy. *SIAM Journal on Numerical Analysis*, 41(5):1926–1947.

[21] Griebel, M. and Klitz, M. (2014). Simulation of droplet impact with dynamic contact angle boundary conditions. In Griebel, M., editor, *Singular Phenomena and Scaling in Mathematical Models*, pages 297–325. Springer International Publishing.

[22] Haas, J. and Sturtevant, B. (1987). Interaction of weak shock waves with cylindrical and spherical gas inhomogeneities. *Journal of Fluid Mechanics*, pages 41–76.

[23] Han, L., Hu, X., and Adams, N. (2014). Adaptive multi-resolution method for compressible multi-phase flows with sharp interface model and pyramid data structure. *Journal of Computational Physics*, 262:131–152.

[24] Han, L., Hu, X., and Adams, N. (2015). Scale separation for multi-scale modeling of free-surface and two-phase flows with the conservative sharp interface method. *Journal of Computational Physics*, 280:387–403.

[25] Harten, A. (1983). High resolution schemes for hyperbolic conservation laws. *Journal of computational physics*, 49(3):357–393.

[26] Hejazialhosseini, B., Rossinelli, D., Bergdorf, M., and Koumoutsakos, P. (2010). High order finite volume methods on wavelet-adapted grids with local time-stepping on multicore architectures for the simulation of shock-bubble interactions. *Journal of Computational Physics*, 229(22):8364–8383.

[27] Herrmann, M. (2005). Refined level set grid method for tracking interfaces. *Annual Research Briefs, Center for Turbulence*.

[28] Herrmann, M. (2008). A balanced force refined level set grid method for two-phase flows on unstructured flow solver grids. *Journal of Computational Physics*, 227(4):2674–2706.

[29] Herrmann, M. (2010). A parallel Eulerian interface tracking/Lagrangian point particle multi-scale coupling procedure. *Journal of Computational Physics*, 229(3):745–759.

[30] Hirt, C., Amsden, A., and Cook, J. (1997). An arbitrary lagrangian–eulerian computing method for all flow speeds. *Journal of Computational Physics*, 135(2):203–216.

[31] Hirt, C. W. and Nichols, B. D. (1981). Volume of fluid (vof) method for the dynamics of free boundaries. *Journal of computational physics*, 39(1):201–225.

[32] Hoath, S. D., Jung, S., and Hutchings, I. M. (2013). A simple criterion for filament break-up in drop-on-demand inkjet printing. *Physics of Fluids*, 25:21701.

[33] Hu, X. and Adams, N. (2006). A multi-phase SPH method for macroscopic and mesoscopic flows. *Journal of Computational Physics*, 213(2):844–861.

[34] Hu, X., Adams, N., Herrmann, M., and Iaccarino, G. (2010a). Multi-scale modeling of compressible multi-fluid flows with conservative interface method. In *Proceedings of the Summer Program*, page 301.

[35] Hu, X. and Khoo, B. (2004). An interface interaction method for compressible multifluids. *Journal of Computational Physics*, 198(1):35–64.

[36] Hu, X. Y. and Adams, N. A. (2007). An incompressible multi-phase SPH method. *Journal of Computational Physics*, 227(1):264–278.

[37] Hu, X. Y., Khoo, B. C., Adams, N. A., and Huang, F. L. (2006). A conservative interface method for compressible flows. *Journal of Computational Physics*, 219(2):553–578.

[38] Hu, X. Y., Wang, Q., and Adams, N. A. (2010b). An adaptive central-upwind weighted essentially non-oscillatory scheme. *Journal of Computational Physics*, 229(23):8952–8965.

[39] Jacqmin, D. (2000). Contact-line dynamics of a diffuse fluid interface. *Journal of Fluid Mechanics*, 402:57–88.

[40] Jamet, D., Torres, D., and Brackbill, J. (2002). On the theory and computation of surface tension: the elimination of parasitic currents through energy conservation in the second-gradient method. *Journal of Computational Physics*, 182(1):262–276.

[41] Jiang, G. and Shu, C. (1996). Efficient implementation of weighted eno schemes. *Journal of Computational Physics*, 126:202–228.

[42] Lauer, E., Hu, X., Hickel, S., and Adams, N. (2012). Numerical modelling and investigation of symmetric and asymmetric cavitation bubble dynamics. *Computers and Fluids*, 69:1–19.

[43] Lister, J. R. and Stone, H. A. (1998). Capillary breakup of a viscous thread surrounded by another viscous fluid. *Physics of Fluids (1994-present)*, 10(11):2758–2764.

[44] Lorensen, W. E. and Cline, H. E. (1987). Marching cubes: A high resolution 3d surface construction algorithm. *SIGGRAPH Comput. Graph.*, 21(4):163–169.

[45] Miniati, F. and Colella, P. (2007). Block structured adaptive mesh and time refinement for hybrid, hyperbolic+< i> n</i>-body systems. *Journal of Computational Physics*, 227(1):400–430.

[46] Ménard, T., Tanguy, S., and Berlemont, A. (2007). Coupling level set/vof/ghost fluid methods: Validation and application to 3d simulation of the primary break-up of a liquid jet. *International Journal of Multiphase Flow*, 33(5):510–524.

[47] Monaghan, J. J. (1994). Simulating free surface flows with sph. *Journal of computational physics*, 110(2):399–406.

[48] Notz, P. and Basaran, O. (2004). Dynamics and breakup of a contracting liquid filament. *Journal of Fluid Mechanics*, 512(1):223–256.

[49] Nourgaliev, R., Liou, M., and Theofanous, T. (2008). Numerical prediction of interfacial instabilities: Sharp interface method (sim). *Journal of Computational Physics*, 227(8):3940–3970.

[50] Nourgaliev, R., Theofanous, T., and Wiri, S. (2006a). Short communications:"direct numerical simulations of two-layer viscosity-stratified flow, by qing cao, kausik sarkar, ajay k. prasad, ijmf (2004) 30, 1485-1508". *International Journal of Multiphase Flow*.

[51] Nourgaliev, R. R., Dinh, T.-N., and Theofanous, T. G. (2006b). Adaptive characteristics-based matching for compressible multifluid dynamics. *Journal of Computational Physics*, 213(2):500–529.

[52] Oron, A., Davis, S. H., and Bankoff, S. G. (1997). Long-scale evolution of thin liquid films. *Reviews of modern physics*, 69(3):931.

[53] Osher, S. and Fedkiw, R. (2003). *Level Set Methods and Dynamic Implicit Surfaces*, volume 153. Springer Science & Business Media.

[54] Osher, S. and Fedkiw, R. P. (2001). Level set methods: an overview and some recent results. *Journal of Computational physics*, 169(2):463–502.

[55] Osher, S. and Sethian, J. A. (1988). Fronts propagating with curvature-dependent speed: algorithms based on hamilton-jacobi formulations. *Journal of computational physics*, 79(1):12–49.

[56] Peng, D., Merriman, B., Osher, S., Zhao, H., and Kang, M. (1999). A pde-based fast local level set method. *Journal of Computational Physics*, 155(2):410–438.

[57] Perigaud, G. and Saurel, R. (2005). A compressible flow model with capillary effects. *Journal of Computational Physics*, 209(1):139–178.

[58] Qian, T., Wang, X.-P., and Sheng, P. (2003). Molecular scale contact line hydrodynamics of immiscible flows. *Physical Review E*, 68(1):016306.

[59] Rioboo, R., Tropea, C., and Marengo, M. (2001). Outcomes from a drop impact on solid surfaces. *Atomization and Sprays*, 11(2):155–165.

[60] Rocca, G. D. and Blanquart, G. (2014). Level set reinitialization at a contact line. *Journal of Computational Physics*, 265:34–49.

[61] Salac, D. and Lu, W. (2008). A local semi-implicit level-set method for interface motion. *Journal of Scientific Computing*, 35(2):330–349.

[62] Sambasivan, S. K. and UdayKumar, H. (2010). Sharp interface simulations with local mesh refinement for multi-material dynamics in strongly shocked flows. *Computers and Fluids*, 39(9):1456–1479.

[63] Savva, N. and Kalliadasis, S. (2011). Dynamics of moving contact lines: A comparison between slip and precursor film models. *EPL (Europhysics Letters)*, 94(6):64004.

[64] Scardovelli, R. and Zaleski, S. (1999). Direct numerical simulation of free-surface and interfacial flow. *Annual Review of Fluid Mechanics*, 31(1):567–603.

[65] Schönfeld, F. and Hardt, S. (2009). Dynamic contact angles in cfd simulations. *Computers & Fluids*, 38(4):757–764.

[66] Schranner, F. S., Hu, X. Y., and Adams, N. A. (2013). A physically consistent weakly compressible high-resolution approach to underresolved simulations of incompressible flows. *Computers and Fluids*.

[67] Shikhmurzaev, Y. D. (2007). *Capillary flows with forming interfaces*. CRC Press.

[68] Shu, C.-W. and Osher, S. (1988). Efficient implementation of essentially non-oscillatory shock-capturing schemes. *Journal of Computational Physics*, 77(2):439–471.

[69] Sibillo, V., Pasquariello, G., Simeone, M., Cristini, V., and Guido, S. (2006). Drop deformation in microconfined shear flow. *Physical review letters*, 97(5):054502.

[70] So, K. K., Hu, X. Y., and Adams, N. A. (2012). Anti-diffusion interface sharpening technique for two-phase compressible flow simulations. *Journal of Computational Physics*, 231(11):4304–4323.

[71] Spelt, P. D. M. (2005). A level-set approach for simulations of flows with multiple moving contact lines with hysteresis. *Journal of Computational Physics*, 207(2):389–404.

[72] Sprittles, J. E. and Shikhmurzaev, Y. D. (2013). Finite element simulation of dynamic wetting flows as an interface formation process. *Journal of Computational Physics*, 233(1):34–65.

[73] Suh, Y. and Son, G. (2009). A sharp-interface level-set method for simulation of a piezoelectric inkjet process. *Numerical Heat Transfer, Part B: Fundamentals*, 55(4):295–312.

[74] Sui, Y. and Spelt, P. D. M. (2013). An efficient computational model for macroscale simulations of moving contact lines. *Journal of Computational Physics*.

[75] Sussman, M. and Fatemi, E. (1999). An efficient, interface-preserving level set redistancing algorithm and its application to interfacial incompressible fluid flow. *SIAM Journal on scientific computing*, 20(4):1165–1191.

[76] Sussman, M., Fatemi, E., Smereka, P., and Osher, S. (1998). An improved level set method for incompressible two-phase flows. *Computers & Fluids*, 27(5):663–680.

[77] Sussman, M. and Puckett, E. G. (2000). A coupled level set and volume-of-fluid method for computing 3d and axisymmetric incompressible two-phase flows. *Journal of Computational Physics*, 162(2):301–337.

[78] Sussman, M., Smereka, P., and Osher, S. (1994). A level set approach for computing solutions to incompressible two-phase flow. *Journal of Computational physics*, 114(1):146–159.

[79] Sussman, M., Smith, K., Hussaini, M., Ohta, M., and Zhi-Wei, R. (2007). A sharp interface method for incompressible two-phase flows. *Journal of Computational Physics*, 221(2):469–505.

[80] Tanner, L. H. (1979). The spreading of silicone oil drops on horizontal surfaces. *Journal of Physics D: Applied Physics*, 12(9):1473.

[81] Torres, D. and Brackbill, J. (2000). The point-set method: front-tracking without connectivity. *Journal of Computational Physics*, 165(2):620–644.

[82] Tryggvason, G., Bunner, B., Esmaeeli, A., Juric, D., Al-Rawahi, N., Tauber, W., Han, J., Nas, S., and Jan, Y.-J. (2001). A front-tracking method for the computations of multiphase flow. *Journal of Computational Physics*, 169(2):708–759.

[83] Unverdi, S. O. and Tryggvason, G. (1992). A front-tracking method for viscous, incompressible, multi-fluid flows. *Journal of computational physics*, 100(1):25–37.

[84] Walker, C. and Müller, B. (2013). Contact line treatment with the sharp interface method. *MekIT*, 11:451–462.

[85] Wang, Z., Yang, J., and Stern, F. (2009). An improved particle correction procedure for the particle level set method. *Journal of Computational Physics*, 228(16):5819–5837.

[86] Webster, D. R. and Longmire, E. K. (2001). Jet pinch-off and drop formation in immiscible liquid–liquid systems. *Experiments in fluids*, 30(1):47–56.

[87] Wijshoff, H. (2010). The dynamics of the piezo inkjet printhead operation. *Physics reports*, 491(4):77–177.

[88] Wörner, M. (2012). Numerical modeling of multiphase flows in microfluidics and micro process engineering: a review of methods and applications. *Microfluidics and Nanofluidics*, 12(6):841–886.

[89] Yue, P. and Feng, J. J. (2011). Can diffuse-interface models quantitatively describe moving contact lines? *The European Physical Journal Special Topics*, 197(1):37–46.

[90] Zhou, H. and Pozrikidis, C. (1993). The flow of suspensions in channels: single files of drops. *Physics of Fluids A: Fluid Dynamics*, 5:311.

[91] Zosel, A. (1993). Studies of the wetting kinetics of liquid drops on solid surfaces. *Colloid and Polymer Science*, 271(7):680–687.

Appendix A:

I

Article I

J. Luo, X.Y. Hu N.A. Adams

A conservative sharp interface method for incompressible multiphase flow

In *Journal of Computational Physics*, Volume 284, 1 March 2015, pp. 547-565, DOI http://dx.doi.org/10.1016/j.jcp.2014.12.044.

Contribution: My contribution to this work was the development of the method and the corresponding computer code for its implementation. I performed simulations and analyzed the results, and wrote the manuscript for the publication.

ELSEVIER LICENSE
TERMS AND CONDITIONS

Aug 09, 2016

This Agreement between Jian Luo ("You") and Elsevier ("Elsevier") consists of your license details and the terms and conditions provided by Elsevier and Copyright Clearance Center.

License Number	3924740854517
License date	Aug 09, 2016
Licensed Content Publisher	Elsevier
Licensed Content Publication	Journal of Computational Physics
Licensed Content Title	A conservative sharp interface method for incompressible multiphase flows
Licensed Content Author	J. Luo,X.Y. Hu,N.A. Adams
Licensed Content Date	1 March 2015
Licensed Content Volume Number	284
Licensed Content Issue Number	n/a
Licensed Content Pages	19
Start Page	547
End Page	565
Type of Use	reuse in a thesis/dissertation
Intended publisher of new work	other
Portion	full article
Format	both print and electronic
Are you the author of this Elsevier article?	Yes
Will you be translating?	No
Order reference number	
Title of your thesis/dissertation	Conservative sharp interface methods for incompressible multi-phase flow
Expected completion date	Apr 2016
Estimated size (number of pages)	100
Elsevier VAT number	GB 494 6272 12
Requestor Location	Jian Luo Youyi West Road 127 P.O. Box 638 Xi'an, Shaanxi 710072 China Attn: Jian Luo
Total	0.00 EUR
Terms and Conditions	

Journal of Computational Physics 284 (2015) 547–565

Contents lists available at ScienceDirect

Journal of Computational Physics

www.elsevier.com/locate/jcp

A conservative sharp interface method for incompressible multiphase flows

J. Luo, X.Y. Hu *, N.A. Adams

Institute of Aerodynamics and Fluid Mechanics, Technische Universität München, 85747 Garching, Germany

ARTICLE INFO

Article history:
Received 28 April 2014
Received in revised form 17 December 2014
Accepted 27 December 2014
Available online 6 January 2015

Keywords:
Multiphase flow
Sharp interface
Weakly compressible
Surface tension
Level-set
Volume fraction

ABSTRACT

In this work, we develop a conservative sharp interface method based on [25] for incompressible flows with viscous and surface tension effects. Employing a weakly compressible framework, the method is simple, mass conserving and capable of handling flows with large density and viscosity ratios and high surface tension. Since the viscosity jump at the material interface is directly imposed by an interface-flux term, momentum conservation is ensured when capillary effects are absent. Furthermore, a subcell-resolution method for volume-fraction evaluation is developed to achieve accurate interface reconstruction. A number of two and three dimensional numerical examples, are considered to demonstrate that the present method is able to simulate a wide range of flow problems with good robustness and high accuracy.

1. Introduction

In multiphase flows, surface-tension forces and viscous forces often play important roles. For example, the deformation of liquid drops in shear flow is governed by the competition between surface-tension forces and viscous forces [49]. From a numerical perspective, surface tension leads to a singular force only acting at the interface, and differences of density or viscosity introduce discontinuities of material properties across the interface. The treatment of interactions at the interface is a challenge for numerical models of multiphase flows.

In general, there are two established approaches for modeling interface interactions, the diffuse-interface method and the sharp-interface method. With the diffuse-interface method the interface is represented by an artificial region with limited thickness, where the transition from one phase to the other is smooth. Material properties, such as viscosity and density, are represented by a smooth function, such as the volume fraction [20] or a Heaviside function [52]. For computing surface tension, a widespread approach is the continuum-surface-force method [4], where the singular surface tension force is regularized by a delta function obtained from the volume fraction or a smooth Heaviside function [52]. While the diffuse-interface methods are conceptually simple, the artificial mixing region may generate nonphysical artifacts, such as parasitic flows near a static interface by surface tension and wrongly predicted instability growth rates of viscous interfacial flows [45,26,38,37]. With the sharp-interface method, the interface as well as the interface interactions are all localized at the infinitely thin interface. Various approaches have been developed to obtain a sharp interface representation. Examples of such approaches include the arbitrary Lagrangian Eulerian (ALE) method [19], where the interface is represented by the computational mesh which evolves and deforms with the flow, the front-tracking method [54,45] where the interface

* Corresponding author.
E-mail addresses: Jian.Luo@tum.de (J. Luo), Xiangyu.Hu@tum.de (X.Y. Hu), Nikolaus.Adams@tum.de (N.A. Adams).

http://dx.doi.org/10.1016/j.jcp.2014.12.044
0021-9991/

is represented explicitly by interface markers, and the level-set method [52], where the interface is defined as the zero level-set of a signed-distance function.

While the level-set method is simple and shares algorithmic similarities with the diffuse-interface method, it is able to handle large interface deformations and topological changes in a straight-forward way [39]. A main drawback of the level-set method is the lack of discrete conservation properties. For incompressible flow this problem has been addressed by hybrid methods, such as the particle level-set method [11,55] and the coupled level-set and volume-of-fluid method (CLSVOF) [51,34]. While these approaches increase computational complexity they also compromise the simplicity of the pure level-set method. To maintain simplicity Glimm et al. [16] introduced a conservative method based on a grid intersection technique for compressible flow without topological interface changes. A fully conservative level-set based sharp-interface method for compressible flows capable of dealing with topological interface changes was introduced by Hu et al. [25]. In this method the underlying conservative scheme on a Cartesian grid is modified for computational cells that are cut by the interface. A mixing procedure is introduced to avoid a time-step restriction due to small or empty cells. In order to calculate the numerical fluxes and fluid states associated with cut cells, the cell-face aperture and volume fraction are reconstructed from the level-set function. While the simple algorithm used by the original method [25] is suitable only for two-dimensional reconstruction, more elaborate marching square or marching cube [32] algorithms are required for accurate reconstruction in three dimensions. The difficulty is that these algorithms are either not accurate due to ambiguous topology or they are complex and computationally costly due to the necessity of identifying the correct topology [29].

Sharp-interface methods require fully coupled treatments of surface tension and viscous forces at the interface singularity. Sussman et al. [50] treated the pressure jump introduced by surface tension in incompressible flows by a Dirichlet boundary condition when solving the two-domain pressure-Poisson equation. Bo et al. [1] modeled the surface tension in compressible flow as a pressure jump within the Riemann problem between the real fluid state and its corresponding ghost fluid state, following the ghost fluid method [13]. Nourgaliev et al. [37] modeled surface-tension and viscous-stress for incompressible flows by applying jump conditions at the interface for density, viscosity and pressure. However, discrete mass conservation is not ensured in these methods. A mass conservative sharp-interface method by employing an unstructured mesh near the interface has been developed by Chang et al. [8]. While this method has been demonstrated to be accurate and efficient for computing surface tension and viscous forces for two-dimensional problems, an extension to three dimensions may, however, be challenging, especially when the interface and thus also the unstructured meshes becomes very complex, as in most practical applications.

In this paper we develop a conservative sharp-interface method based on Ref. [25] for incompressible multiphase flows by employing a weakly compressible model, which is widely used e.g. in smoothed particle hydrodynamics (SPH) [35,21] and the lattice Boltzmann method [9]. Moreover, the weakly compressible model has been applied recently to study a range of turbulent and non-turbulent incompressible flows [46]. From the original method for compressible multi-phase flow the present method inherits the property of mass conservation and the ability of handling large density ratios. Unlike the effective-viscosity approach in the diffusive-interface method [28,31], where a mixture viscosity is used to represent the effective viscosity of the entire mixture cell cut by the interface, the present method imposes the viscosity jump at the interface directly on the momentum flux across the interface to ensure momentum conservation and the ability of handling large viscosity ratios. For interface reconstruction, a subcell-resolution scheme by refining the cut cell recursively is used to calculating cell-face aperture and volume fraction. Such scheme avoids the complicated topology-identification operations in marching cube algorithms, and eliminates the error due to ambiguous topology. It also is much easier to program than marching-square or marching-cube schemes, where 16 cases in two-dimensions and 256 cases in three-dimensions have to be identified [32].

In Section 2, we give an overview of the conservative sharp-interface method for simulating incompressible flows with the weakly compressible model. We briefly review the level-set method for the interface representation, and propose a subcell-resolution scheme to calculate the volume fraction and cell-face apertures in Section 3. In Section 4, we present the method for calculating the viscous stress at the interface, a momentum-flux based surface tension formulation. The overall method is validated with numerical examples in two and three dimensions in Section 5, and concluding remarks are given in Appendix A.

2. Weakly compressible sharp interface method

For the weakly compressible model the governing equations can be written as

$$\frac{\partial \mathbf{U}}{\partial t} + \nabla \cdot \mathbf{F} = \nabla \cdot \mathbf{F}_v + \mathbf{a}_s, \tag{1}$$

where $\mathbf{U}$ is the vector of mass and momentum densities; $\mathbf{F}$ represents the convective fluxes, and $\mathbf{F}_v$ the viscous fluxes. Note that the right-hand side of Eq. (1) vanishes when it represents the continuity equation. For momentum conservation, the surface-tension force is given by

$$\mathbf{a}_s = \sigma \kappa \delta_n \mathbf{N} \tag{2}$$

where σ, κ, $\mathbf{N}$ are surface tension, curvature and normal direction of the interface, respectively. δ_n is a Dirac delta function defined in the normal direction of the interface.

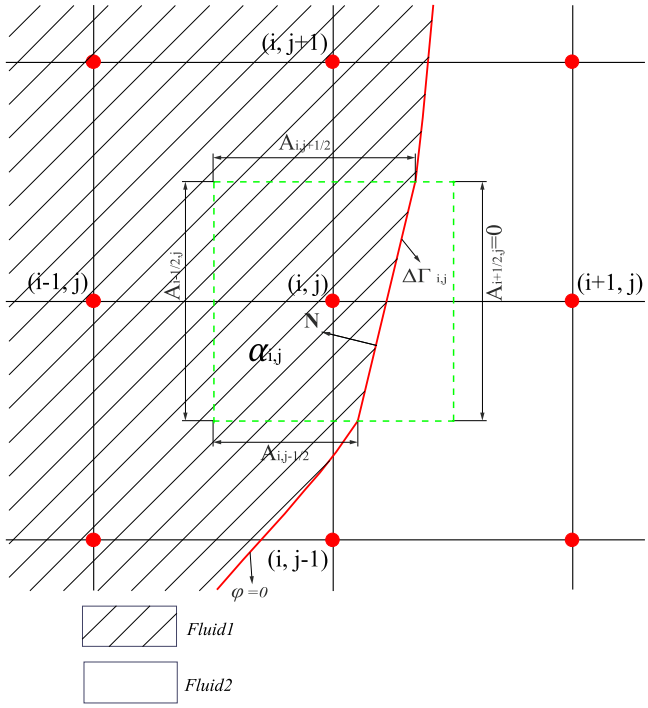

Fig. 1. Schematic of discretization for a cut cell (i, j) on a collocated grid: the red dot indicates the cell center, the red line indicates the interface, the green dashed line indicates the cell face, $\alpha_{i,j}$ denotes the volume fraction occupied by *fluid*1 in cut cell (i, j), A denotes the cell-face aperture, $\mathbf{N}$ is the normal direction of the interface and $\Delta\Gamma_{i,j}$ the segment of the interface. (For interpretation of the references to color in this figure legend, the reader is referred to the web version of this article.)

To close the governing equations an artificial equation of state relating the pressure and density is used. Here, we use Tait's equation

$$p = B\left[\left(\frac{\rho}{\rho_0}\right)^{\gamma} - 1\right] + p_0$$
$$B = \frac{\rho_0 |v_f|^2}{\gamma M^2}, \tag{3}$$

where M is the Mach number, γ is an artificial specific-heat ratio, v_f denotes a characteristic flow velocity, ρ_0 and p_0 are reference density and pressure, respectively. The artificial sound speed is $c = \sqrt{\frac{\gamma B}{\rho}}$. To impose incompressibility, we choose the parameters γ, B and ρ_0 such that the Mach number satisfies $M = \frac{|v_f|}{c} \approx 0.1$.

The flow domain Ω is divided by a time-dependent interface Γ into two sub-domains Ω^1 and Ω^2, which denote the regions occupied by *fluid*1 and *fluid*2, as shown in Fig. 1. We solve Eq. (1) for each fluid in its respective sub-domain Ω^m $(m = 1, 2)$, as in Hu et al. [25], on a two-dimensional collocated Cartesian grid with spacing Δx and Δy. Integrating Eq. (1) over a computational cell and applying the Gauss' theorem yields

$$\int_n^{n+1} dt \int_{\Delta_{i,j} \bigcap \Omega^m} dxdy \frac{\partial \mathbf{U}}{\partial x} + \int_n^{n+1} dt \int_{\partial(\Delta_{i,j} \bigcap \Omega^m)} dxdy \mathbf{F} \cdot \mathbf{n}$$
$$= \int_n^{n+1} dt \int_{\partial(\Delta_{i,j} \bigcap \Omega^m)} dxdy \mathbf{F}_v \cdot \mathbf{n} + \int_n^{n+1} dt \int_{\Delta\Gamma_{i,j}} dxdy \mathbf{F}_s \cdot \mathbf{n}, \tag{4}$$

where $\Delta_{i,j} = \Delta x \Delta y$ is the cell volume; $\Delta_{i,j} \cap \Omega^m$ can be represented as $\alpha_{i,j}\Delta_{i,j}$, where $\alpha_{i,j}$ is the time dependent volume fraction of fluid m and satisfies $1 \geq \alpha \geq 0$. $\partial(\Delta_{i,j} \cap \Omega^m)$ denotes the faces of cell i, j wetted by fluid m, including the interface segment contained in the cell, and $\mathbf{F}_s$ is an additional flux at the interface due to surface tension. The surface $\partial(\Delta_{i,j} \cap \Omega^m)$ with surface normal $\mathbf{n}$ can be represented by two parts. One part is the combination of four segments (in two-dimensions) of the cut cell faces, which can be written as $A_{i+1/2,j}\Delta y$, $A_{i,j+1/2}\Delta x$, $A_{i-1/2,j}\Delta y$ and $A_{i,j-1/2}\Delta x$, where $1 \geq A \geq 0$ is the time-dependent cell-face aperture. The second, denoted as $\Delta\Gamma_{i,j}$, is the segment of the interface Γ inside of cell (i, j). Hence, Eq. (4) can be rewritten in the following form, using explicit first-order forward time difference,

$$\begin{aligned}\alpha_{i,j}^{n+1}\mathbf{U}_{i,j}^{n+1} = \alpha_{i,j}^{n}\mathbf{U}_{i,j}^{n} &+ \frac{\Delta t}{\Delta x\Delta y}\left[\hat{\mathbf{X}}(\Delta\Gamma_{i,j}) + \hat{\mathbf{X}}_{\nu}(\Delta\Gamma_{i,j}) + \hat{\mathbf{X}}_{s}(\Delta\Gamma_{i,j})\right] \\ &+ \frac{\Delta t}{\Delta x}[A_{i-1/2,j}\hat{\mathbf{F}}_{i-1/2,j} - A_{i+1/2,j}\hat{\mathbf{F}}_{i+1/2,j}] \\ &+ \frac{\Delta t}{\Delta y}[A_{i,j-1/2}\hat{\mathbf{F}}_{i,j-1/2} - A_{i,j+1/2}\hat{\mathbf{F}}_{i,j+1/2}] \\ &+ \frac{\Delta t}{\Delta x}[A_{i-1/2,j}\hat{\mathbf{F}}_{\nu i-1/2,j} - A_{i+1/2,j}\hat{\mathbf{F}}_{\nu i+1/2,j}] \\ &+ \frac{\Delta t}{\Delta y}[A_{i,j-1/2}\hat{\mathbf{F}}_{\nu i,j-1/2} - A_{i,j+1/2}\hat{\mathbf{F}}_{\nu i,j+1/2}],\end{aligned} \tag{5}$$

where Δt is the time step size. $\mathbf{U}_{i,j}$ denotes cell-averaged vector of mass and momentum densities of the considered fluid, and $\alpha_{i,j}\mathbf{U}_{i,j}$ are the conservative quantities in the cut cell. $\hat{\mathbf{X}}$ is the average inviscid momentum flux across the interface, and $\hat{\mathbf{X}}_{\nu}$ denotes the momentum flux due to the viscous force. $\hat{\mathbf{X}}_{s}$ is the momentum flux due to the interfacial pressure jump induced by surface tension. Note that all the interface fluxes ($\hat{\mathbf{X}}, \hat{\mathbf{X}}_{\nu}, \hat{\mathbf{X}}_{s}$) vanish when Eq. (5) discretizes the continuity equation. All the terms on the right-hand side are calculated at time step n. Note that the extension of Eq. (5) to three dimensions is straightforward. Specifically, one needs to calculate cell-face apertures, volume fraction and interface patch in a in three-dimensional cut cell, which is detailed in Section 3.2. Also note that, as shown in Hu et al. [25], discrete global conservation is maintained for flows without capillary effects.

In this paper, the governing equations of the individual fluids are discretized by a 5th-order WENO-LLF scheme [27] and 2nd-order TVD Runge–Kutta time integration [48]. The time-step is set according to [51],

$$\Delta t = CFL\cdot\min\left(\frac{\Delta x}{|u^n| + c^n}, \frac{\rho^n\Delta x^2}{\mu}, \sqrt{\frac{\rho^n}{8\pi\sigma}}\Delta x^{\frac{3}{2}}\right), \tag{6}$$

where c^n is the artificial sound speed at time step n. We set $CFL = 0.6$ for all our simulations. For a small or empty cell, a stable fluid state may not be obtained based on the time step calculated according to the full grid size CFL condition. Therefore, a mixing procedure is introduced to maintain numerical stability [25]. In addition, a wavelet-based adaptive multi-resolution algorithm [17] is adopted for improving computational efficiency.

3. Interface modeling

3.1. Level-set method

The level-set function, φ, which describes the signed distance from the interface to each cell center, is used to track the interface. The zero-level set, i.e. $\varphi = 0$, represents the interface Γ. The entire domain is divided into two sub-domains, characterized by opposite signs of the level set function. Hereafter, the positive sub-domain refers to *fluid*1, and the negative sub-domain refers to *fluid*2. The level-set field is advanced by [13]

$$\frac{\partial\varphi}{\partial t} + \mathbf{u}\cdot\nabla\varphi = 0, \tag{7}$$

where $\mathbf{u}$ represents the velocity for the level set obtained with the interface interaction model [24]. In practice, the level-set is updated only in a narrow band near the interface. Outside of the narrow band it is re-initialized by the following equation [13]

$$\frac{\partial\varphi}{\partial\tau} + \mathrm{sgn}(\varphi)\big(|\nabla\varphi| - 1\big) = 0, \tag{8}$$

in order to maintain the signed-distance property of the level set, where τ is the a pseudo time.

3.2. Interface reconstruction

To solve Eq. (5), the information of the interface associated with the cut-cell, such as volume fraction, cell-face apertures and interface curvature, are reconstructed from the level-set function.

The accuracy of the approach originally proposed in Hu et al. [25] for calculating cell-face aperture and volume fraction can be improved by a subcell-resolution interface-reconstruction scheme. As will be shown in Section 4.7.2, such improvement of accuracy is able to improve numerical stability when non-resolved interface singularities are produced in the solution. In the subcell-resolution interface-reconstruction scheme, cut cells are divided into two types: (i) simple-interface cells in which the interface is a single connected patch, and (ii) complex-interface cells in which the interface possibly has multiple unconnected patches, e.g. the cell is cut by the interface more than once. For a simple-interface cell, the corresponding volume fraction and apertures are computed directly due to its simple geometry. A complex-interface cell is refined recursively into subcells until each subcell is a simple-interface cell or the relative error reaches a certain threshold.

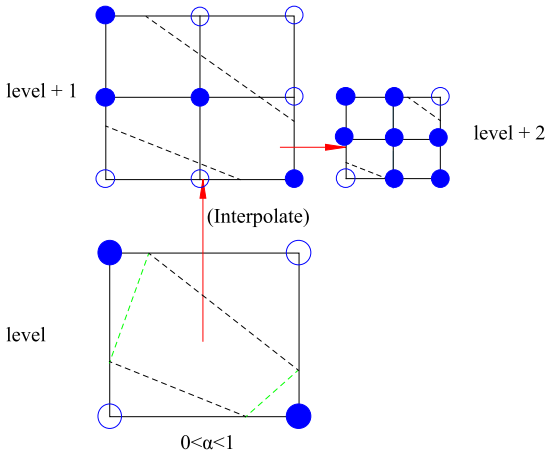

Fig. 2. Schematic for refining the complex-interface-cell in two dimensions. Solid circle and open circle indicate the cell corners with positive and negative values of the level set, respectively. The black dashed line indicates the actual interface, and the green one a possible reconstructed interface. (For interpretation of the references to color in this figure legend, the reader is referred to the web version of this article.)

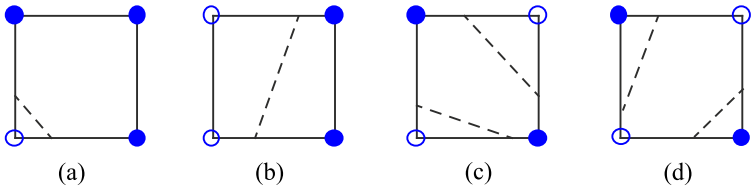

Fig. 3. Four typical cases of cut cells in two-dimensions.

Subsequently, the volume fraction and apertures on the original cut cell are computed by combining the results from all subcells. A complex-interface cell is identified by checking the inconsistency of the local-gradient estimations of the level-set at the cell center, obtained by forward and by backward differences. If these two estimates have opposite signs, the cut-cell is identified as a complex-interface cell.

The procedure of the subcell-resolution reconstruction scheme is sketched in Fig. 2. If a cut cell is identified as a complex-interface cell, it is divided into 4 or 8 equal subcells in two and three dimensions, respectively, and the level set on the centers and corners of subcells is evaluated by bi- or tri-linear interpolation. At the same time, ambiguous topologies are identified by subcell-refinement, as shown in Fig. 2. If a subcell is identified as a complex-interface cell or the relative error of predicted volume fraction is large, it is sub-divided again. Otherwise the refinement is stopped. Since only the cell-face aperture and volume fraction in simple-interface cells are actually computed, very simple algorithms, such as those in Refs. [29] and [23], can be applied. See also the details of an implementation and its extension to three dimensions are described in Appendix A. Note that in this paper the computation of the interface fluxes for complex-interface cells still is preformed at the cell-resolution (not sub-cell) level according to Eq. (5) without further modification.

To validate the subcell-resolution scheme, we consider four typical cases of cut cells including simple-interface cells and complex-interface cells, as shown in Fig. 3. The level set values at cell corners are set as

$$\begin{cases} \text{Case (a)} & (-0.2\sqrt{2}, 0.3\sqrt{2}, 0.3\sqrt{2}, 0.8\sqrt{2.0}) \\ \text{Case (b)} & (0.05\sqrt{5}, 0.25\sqrt{5}, -0.35\sqrt{5}, -0.15\sqrt{5}) \\ \text{Case (c)} & (-0.2\sqrt{2.0}, 0.3\sqrt{2.0}, 0.3\sqrt{2.0}, -0.2\sqrt{2.0}) \\ \text{Case (d)} & (-0.3\sqrt{2.0}, 0.2\sqrt{2.0}, 0.2\sqrt{2.0}, -0.3\sqrt{2.0}). \end{cases} \tag{9}$$

In Table 1 we list the evaluated volume fractions of cut cells with increasing refinement levels. Note that the volume fractions remain the same for the simple-interface cells, while the relative errors for complex-interface cells reduce below 1% at the refinement level of 3. The results suggest second-order convergence. In this paper, the error threshold is set at 1%, so the maximum refinement level of 3 is generally sufficient for all cases.

The interface curvature in a cut cell is defined by $\kappa = \nabla \cdot (\frac{\nabla \varphi}{|\nabla \varphi|})$, which can be rewritten, in three dimensions, as

$$\kappa = \frac{\varphi_{xx} + \varphi_{yy} + \varphi_{zz}}{(\varphi_x^2 + \varphi_y^2 + \varphi_z^2 + \varepsilon)^{1/2}} - \frac{\varphi_x^2 \varphi_{xx} + \varphi_y^2 \varphi_{yy} + \varphi_z^2 \varphi_{zz} + 2(\varphi_x \varphi_y \varphi_{xy} + \varphi_x \varphi_z \varphi_{xz} + \varphi_y \varphi_z \varphi_{yz})}{(\varphi_x^2 + \varphi_y^2 + \varphi_z^2 + \varepsilon)^{3/2}}, \tag{10}$$

where ε is a small positive number to avoid division by zero [44]. Note that the curvature in two dimensions is obtained by setting all derivatives with subscript z to zero. Since all the partial derivatives in Eq. (10) usually are computed at the cell center with standard central difference schemes, the curvature κ is estimated at the cell center. Therefore, this value is

Table 1
Convergence study for the subcell-resolution interface-reconstruction scheme.

Case	Level 0	Level 1	Level 2	Level 3	Level 4
(a)	0.92	0.92	0.92	0.92	0.92
(b)	0.375	0.8	0.375	0.375	0.375
(c)	0.6000	0.7900	0.7558	0.7605	0.7604
(d)	0.4000	0.2100	0.2441	0.2394	0.2395

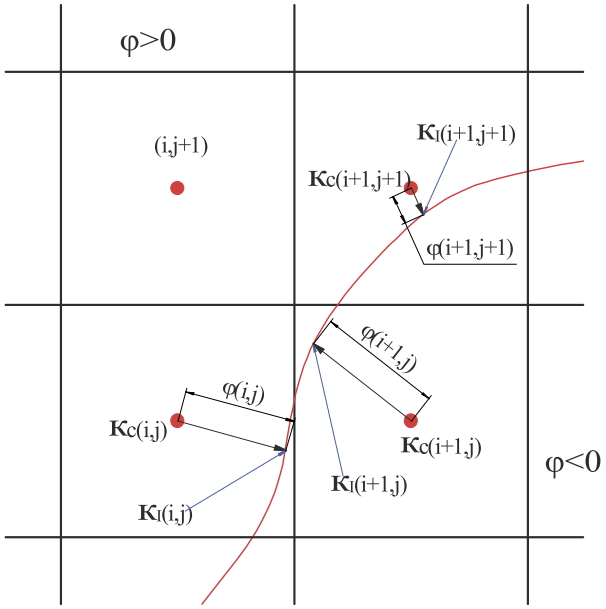

Fig. 4. Correction for interface curvature.

corrected for the distance of the cell center from the interface by approximating the interface locally by a circle or sphere, as shown in Fig. 4, obtaining a corrected curvature as

$$\kappa_I = \frac{(d-1)\kappa}{d-1-\varphi\kappa}, \tag{11}$$

where d is the spatial dimension.

3.3. Viscous flux at the interface

An effective viscosity in the cut cell is constructed to model the viscous flux across the interface, i.e. $\hat{\mathbf{X}}_v$ in Eq. (5), based on two assumptions: (a) in a neighborhood of the interface the velocity distribution is linear within each fluid; (b) the viscous stress is continuous at the interface. Note that, this approach does not follow the jump condition of Kang et al. [28], or Esmaeeli and Tryggvason [12], nevertheless, the continuous-shear-stress assumption proves to be accurate and effective in previous works, such as with front-tracking [56], level-set [52], volume-of-fluid [30] and SPH methods [21]. Consider a simple two-dimensional configuration with two different fluids with viscosity μ_1 for the upper fluid and μ_2 for the lower fluid, as shown in Fig. 5. The volume fractions of the two fluids are α and $1-\alpha$, respectively. Viscous shear stresses at the interface are continuous, thus

$$\mu_I \frac{V_1 - V_2}{1} = \mu_1 \frac{V_1 - V_I}{\alpha} = \mu_2 \frac{V_I - V_2}{1-\alpha}, \tag{12}$$

where μ_I is the effective viscosity, which results as harmonic mean with respect to the volume fractions of the two fluids, i.e.

$$\mu_I = \frac{\mu_1\mu_2}{\alpha\mu_2 + (1-\alpha)\mu_1}. \tag{13}$$

As pointed out by Coward et al. [10], the harmonic average of viscosity is appreciate for the two-layer Couette flow configuration. This expression can be generalized for more general interface orientations cut cells. As now we can obtain viscous stress directly from the velocity difference across the interface. The viscous fluxes across the interface (e.g. in two dimensions) are

$$\hat{\mathrm{X}}_v = (F_{v,x}, F_{v,y}) \cdot (N_x \Delta\Gamma_{i,j}, N_y \Delta\Gamma_{i,j}), \tag{14}$$

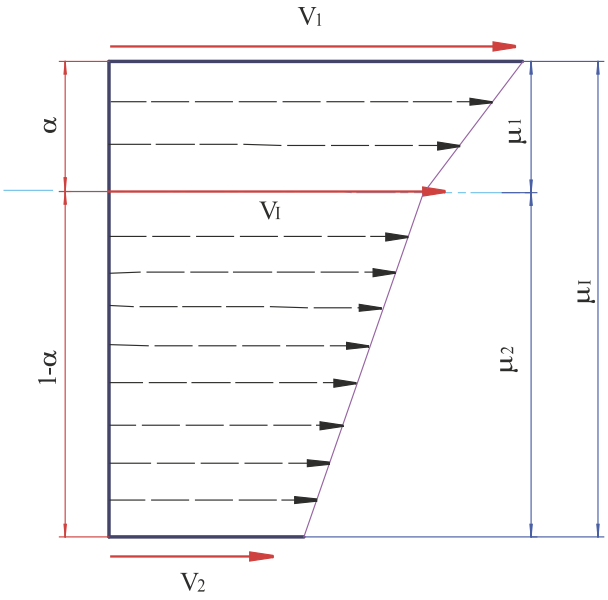

Fig. 5. Simple shear flow with two viscosities in a simplified cut cell.

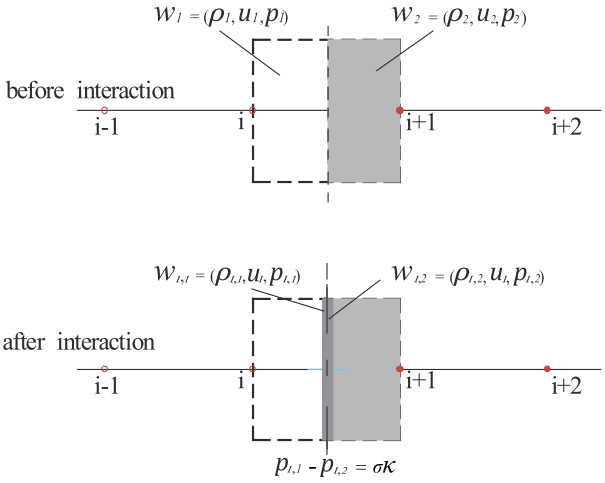

Fig. 6. Schematic for the modified Riemann problem, W_1 and W_2 indicate fluid states for *fluid*1 and *fluid*2, respectively.

where $N_x \Delta \Gamma_{i,j}$ and $N_y \Delta \Gamma_{i,j}$ are the projections of the interface segment in x and y direction, respectively. $F_{v,x} = [\tau_{xx}, \tau_{xy}]^T$ and $F_{v,y} = [\tau_{xy}, \tau_{yy}]^T$ are the components of the viscous stress tensor. The extension to three dimensions is straightforward.

3.4. Surface tension

Surface tension by mechanical equilibrium results in a pressure jump at the interface. It is expressed as

$$[p]_\Gamma = p_{I,1} - p_{I,2} = \sigma\kappa. \tag{15}$$

In order to impose surface tension at the interface, a constrained Riemann problem [1], as sketched in Fig. 6, is solved to impose Eq. (15). Cells with $\varphi < 0$ are defined as on the left and the cells with $\varphi > 0$ as on the right side of the interface. Due to the small Mach number in the weakly compressible model a simple non-iterative linearized Riemann solver is employed [24]. The interface states are obtained as

$$\begin{aligned} u_I &= \frac{\rho_1 c_1 u_1 + \rho_2 c_2 u_2 + p_1 - p_2 - \sigma\kappa}{\rho_1 c_1 + \rho_2 c_2} \\ p_{I1} &= \frac{\rho_1 c_1 (p_2 + \sigma\kappa) + \rho_2 c_2 p_1 + \rho_1 c_1 \rho_2 c_2 (u_1 - u_2)}{\rho_1 c_1 + \rho_2 c_2} \\ p_{I2} &= \frac{\rho_1 c_1 p_2 + \rho_2 c_2 (p_1 - \sigma\kappa) + \rho_1 c_1 \rho_2 c_2 (u_1 - u_2)}{\rho_1 c_1 + \rho_2 c_2}, \end{aligned} \tag{16}$$

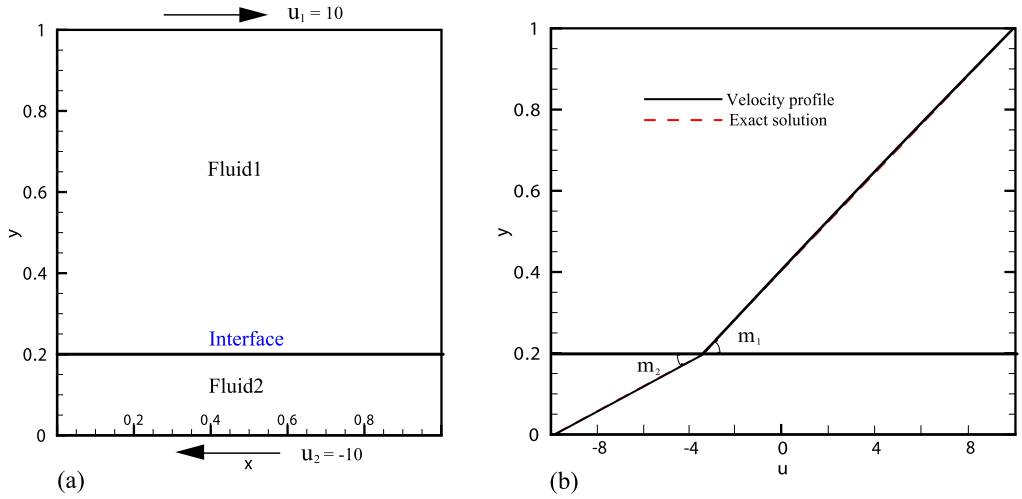

Fig. 7. Viscosity test: (a) Computational domain and initial condition; (b) Velocity profile for fully developed flow.

where u_I is the interface velocity, c_1 and c_2 are the artificial sound speeds, and p_{I1} and p_{I2} the interface pressures for *fluid*1 and *fluid*2, respectively. Other than defining the ghost fluid state as in Ref. [1], the solution of the constrained Riemann problem is used for determining the extra interfacial momentum flux due to surface tension $\hat{\mathbf{X}}_s$ in Eq. (5), which can be integrated into the inviscid momentum flux, i.e. $\hat{\mathbf{X}}$, as

$$\begin{cases} \hat{\mathbf{X}}_1 = -p_{I1}(\Delta\Gamma_{i,j}N_x, \Delta\Gamma_{i,j}N_y) & \text{for } \textit{fluid}1 \\ \hat{\mathbf{X}}_2 = p_{I2}(\Delta\Gamma_{i,j}N_x, \Delta\Gamma_{i,j}N_y) & \text{for } \textit{fluid}2. \end{cases} \tag{17}$$

The extension to three dimensions is straightforward. The above approach also applies to a free surface boundary. Assuming that *fluid*1 represents a fluid subject to the free surface condition, the interfacial condition becomes

$$u_I = u_1 + \frac{p_1 - p_0 - \sigma\kappa}{\rho_1 c_1}, \qquad p_I = p_0 + \sigma\kappa, \tag{18}$$

where p_0 is an external reference pressure.

Note that, due to the non-conservative form of the surface-tension model, the implementation of the pressure jump does not satisfy momentum conservation. However, since the present formulation is based on a conservative sharp-interface method, it maintains the so called zero-order consistency, i.e. a drop with constant curvature or constant pressure jump introduces zero total force acting on the drop.

4. Numerical validation and application examples

The following numerical examples are considered to illustrate the capability of the proposed conservative sharp-interface method to handle viscous forces and surface tension forces: (1) interface separating fluids with different viscosities; (2) static drop with surface tension; (3) parasitic currents; (4) deformed drop oscillation due to surface tension; (5) drop deformation in shear flow; (6) two-fluid Poiseuille flow; (7) liquid-filament contraction.

4.1. Interface separating fluids with different viscosities

A simple shear flow of two viscous horizontal fluid layers is considered to assess the capability of handling discontinuous viscosities. The computational domain is a unit square partitioned by a Cartesian grid with 128×128 cells. The flow is driven with velocities of ± 10 at top and bottom of the domain, respectively. Periodic boundary conditions are applied in the horizontal direction. The interface is located initially at $y = 0.2$, as shown in Fig. 7(a). We consider two fluids with the same densities but different viscosities. The reference velocity is set to $v_f = 10$. Initially, the respective properties of fluids are given by

$$\begin{cases} \rho = 1, \quad p_0 = 10^2, \quad B = 2.0 \times 10^3, \quad \gamma = 7.15, \quad \mu = 2.0 & \textit{fluid}1 \\ \rho = 1, \quad p_0 = 10^2, \quad B = 2.0 \times 10^3, \quad \gamma = 7.15, \quad \mu = 1.0 & \textit{fluid}2 \\ \varphi = y - 0.2 & \text{level-set}. \end{cases} \tag{19}$$

As shown in Fig. 7, the velocity profile of the fully developed flow agrees with the exact solution. A sharp kink appears at the interface in agreement with the exact result, rather than a smooth transition as predicted by a diffuse-interface method [52].

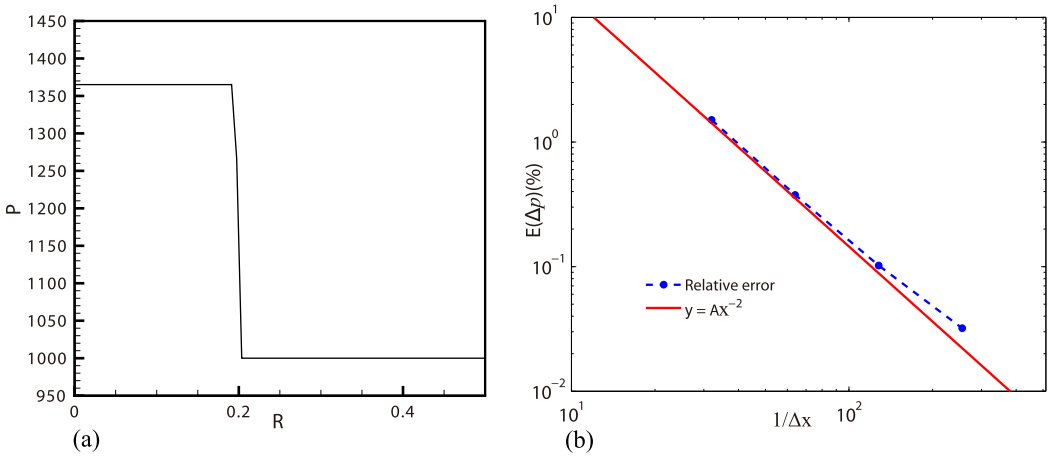

Fig. 8. Laplace law test: (a) Pressure distribution; (b) Relative error according to resolution.

4.2. Static drop with surface tension

We consider a static drop in equilibrium to validate the surface tension model. The computational domain is a unit square with no-slip boundary conditions A liquid drop of radius $R = 0.2$ is placed at the center of the domain, embedded in the air. The surface tension coefficient is $\sigma = 73$. The reference velocity is $v_f = \sqrt{\sigma/\rho R}$, and the initial conditions are

$$\begin{cases} \rho = 1, \quad p_0 = 10^3, \quad B = 10^2, \quad \gamma = 1.4, \quad \mu = 1 & \textit{fluid}1 \\ \rho = 10^3, \quad p_0 = 10^3, \quad B = 10^4, \quad \gamma = 7.15, \quad \mu = 10^2 & \textit{fluid}2 \\ \varphi = -0.2 + \sqrt{(x-0.5)^2 + (y-0.5)^2} & \text{level-set.} \end{cases} \tag{20}$$

Fig. 8(a) shows the steady-state pressure distribution, and Fig. 8(b) depicts the convergence of the relative errors $E(\Delta p) = |\Delta p_{numerical} - \Delta p_{exact}|/\Delta p_{exact}$ with grid refinement. It can be observed that nearly second-order accuracy is obtained.

4.3. Parasitic currents

We consider a 2×2 square computational domain with a drop of diameter $D = 1.0$ placed at its center to evaluate parasitic currents. It is known that parasitic currents exist due to an imbalance between stresses from surface tension and viscosity near the interface, resulting in artificial interface distortions [18,41]. The drop is modeled by a water-like fluid surrounded by a gas-like fluid, and the surface tension is set as $\sigma = 1.0$. The initial conditions are

$$\begin{cases} \rho = 1, \quad p_0 = 10^4, \quad B = 7.0 \times 10^2, \quad \gamma = 1.4, \quad \mu = 1.6 \times 10^{-5} & \text{gas} \\ \rho = 10^3, \quad p_0 = 10^4, \quad B = 10^5, \quad \gamma = 7.15, \quad \mu = 10^{-4} & \text{liquid} \\ \varphi = -0.5 + \sqrt{(x-1)^2 + (y-1)^2} & \text{level-set.} \end{cases} \tag{21}$$

The corresponding Laplace number is $La = \sigma\rho D/\mu^2 = 10^{11}$. First, we consider a drop resting at the center of the computational domain with periodic boundary conditions. Spurious currents for a static configuration manifest themselves as artificial velocity fluctuations. The level of parasitic currents can be measured by the numerical capillary number written as $Ca = U_{\max}\mu/\sigma$, where $U_{\max}$ is the maximum velocity. Fig. 9(a) depicts the time evolution of the capillary number with increasing resolution from 32×32 to 128×128. It is found that after an initial transient the capillary number decays towards a small stationary value, and decreases with increasing resolution. Note that for the method in [1], $La \sim O(10^4)$ was reported as the achievable limit of the method. Instead of reducing viscosity, Chang et al. [8] increased the surface tension coefficient to obtain a capillary number $La = 10^{10}$ with their conservative sharp-interface method. Second, a drop moving at a constant velocity is considered. The setup is the same as for the static drop, except that a constant translation velocity in horizontal direction is inputed as $U_0 = 0.1$. Fig. 9(b) shows the temporal evolution of the capillary number with increasing resolution. It is observed that, while the spurious-current velocity is larger than that for static drop, its normalized magnitude is still very small, on the order of 10^{-5}. Note that for both cases the spurious currents may remain at small finite values due to artificial sound waves formulated by the present weakly compressible model.

4.4. Drop oscillation

The oscillation of a drop under surface tension allows to access the prediction of capillary instabilities [33]. A two-dimensional ellipsoidal drop is filled with a water-like fluid and surrounded by a gas-like fluid. The ellipsoidal drop initially is at rest. Due to the action of surface tension it relaxes in an oscillatory way from ellipsoidal shape to the circular shape.

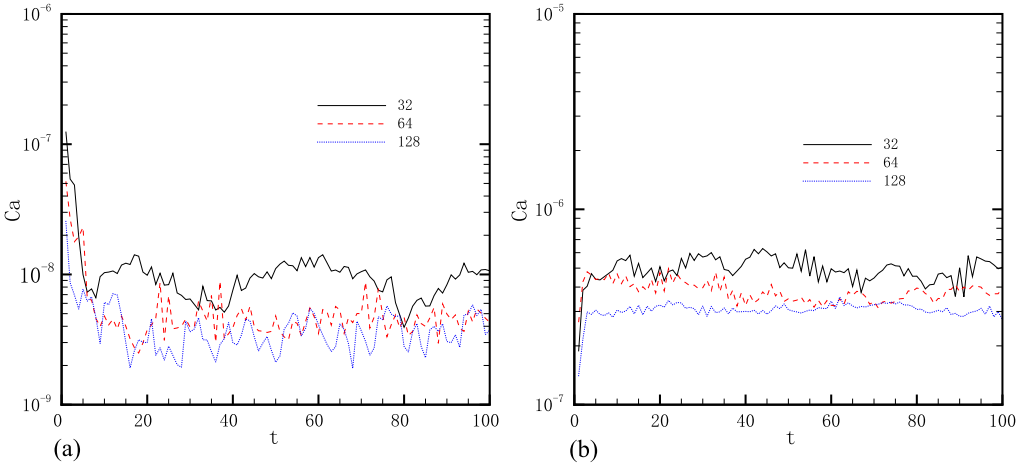

Fig. 9. The evolution of the capillary number with $La = 10^{11}$: (a) A drop fixed at the center of the domain; (b) A moving drop with a constant velocity $U_0 = -0.1$.

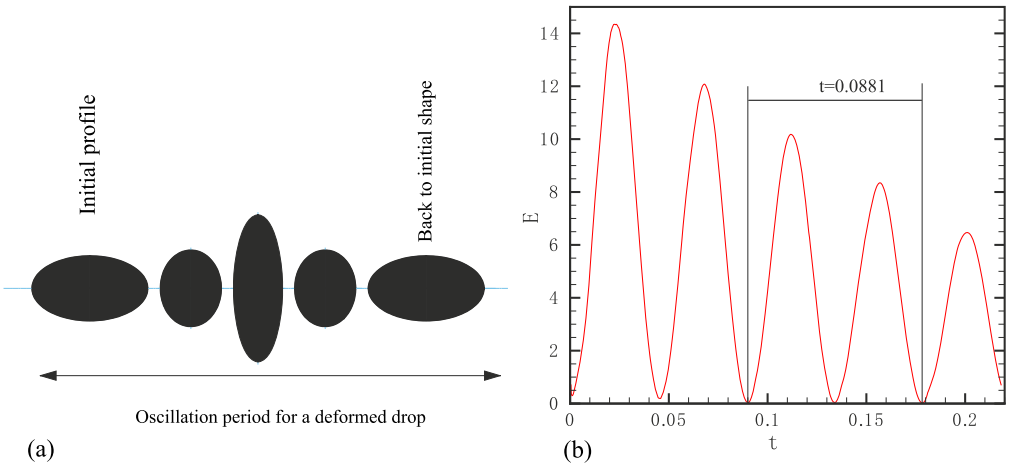

Fig. 10. Oscillations of an ellipsoidal drop: (a) Evolution of deformed shape; (b) Evolution of kinetic energy, $E = \frac{1}{2}\int\int \rho u^2 dxdy$.

The oscillating behavior is associated with a transfer between potential energy and kinetic energy. According to the Rayleigh formula [42,15], the oscillation frequency of a liquid drop with density ρ_l surround by another fluid with density ρ_g is expressed by

$$\omega^2 = \left(o^3 - o\right)\frac{\sigma}{(\rho_l + \rho_g)R^3}, \qquad T = \frac{2\pi}{\omega} \tag{22}$$

where o is an in oscillation mode, and R is the volumetric drop radius. Here, we consider $o = 2$, following [40]. The computational domain is a unit square with no-slip boundary conditions. The ellipsoidal drop is located at the center of the domain, and the surface tension coefficient is $\sigma = 341.642$. The initial conditions are

$$\begin{cases} \rho = 1, \quad p_0 = 10^4, \quad B = 500, \quad \gamma = 1.4 & \text{air} \\ \rho = 10^2, \quad p_0 = 10^4, \quad B = 1.0^5, \quad \gamma = 7.15 & \text{liquid drop} \\ \varphi_0 = -1.0 + \sqrt{(x-0.5)^2/0.2^2 + (y-0.5)^2/0.12^2} & \text{level-set.} \end{cases} \tag{23}$$

Note that φ_0 as defined by Eq. (23) has to be re-initialized by Eq. (8) before the simulation, as it is not a signed distance function. The computation is carried out on a mesh with 128×128 grid points.

As shown in Fig. 10, the oscillation of the liquid drop is well predicted. The theoretical value of the period is $T = 0.0878$ according to Eq. (22), for $R = 0.15825$. Fig. 10(b) shows the evolution of the kinetic energy, from which we can evaluate the predicted oscillation period $T = 0.0881$. The error is about 0.3%, which is less than the 2% error reported in [40], where a diffusive-interface method on a 111×111 grid has been employed.

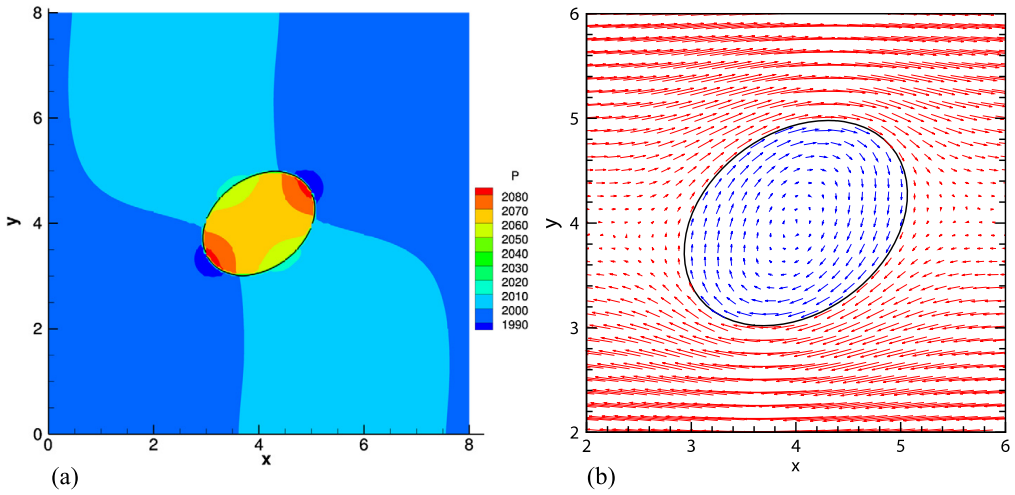

Fig. 11. Drop deformation: (a) The shape of drop in equilibrium and the pressure contour; (b) The velocity field near the interface.

4.5. Drop deformation in shear flow

A drop deforming in a Couette shear flow is computed to validate the present method with coupled effects of viscosity and surface tension. The drop deforms until it reaches a balance between viscous stresses and surface tension. The final shape of the deformed drop is governed by two non-dimensional numbers: the viscosity ratio $\lambda = \mu_c/\mu_d$ and the capillary number $Ca = \mu_c r_0 \dot{\gamma}/\sigma$. $\dot{\gamma}$ is the shear rate, r_0 is the initial drop radius, μ_c and μ_d are viscosities of bulk phase and the drop, respectively. The associated Reynolds number is $Re = \rho \dot{\gamma} r_0^2/\mu_c$. According to linear theory of Taylor [53] the steady equilibrium deformation parameter, for small deformation and small capillary number, is given by

$$D = \frac{L+B}{L-B} = Ca\frac{19\lambda+16}{16\lambda+16}, \tag{24}$$

where L and B represent the semi-major and semi-minor axes of the steady state ellipse, respectively. In the simulation, the deformation parameter is obtained from the relation between the moments of inertia of the ellipse

$$I_1 = \frac{\pi}{4}LB^3, \qquad I_2 = \frac{\pi}{4}L^3B. \tag{25}$$

We consider an initially circular drop with radius $R = 1.0$ centered in the computational domain $8R \times 8R$. A simple shear flow is generated by moving the top and bottom walls with constant velocities ± 4, respectively. Periodic boundary conditions are applied in horizontal direction. The domain is discretized with 256×256 grid points. The surface-tension coefficient is set to $\sigma = 200/3$. Initial conditions are

$$\begin{cases} \rho = 1, \quad p_0 = 2.0 \times 10^3, \quad B = 2.0 \times 10^4, \quad \gamma = 7.15, \quad \mu = 10 & \text{fluids} \\ \varphi = -1 + \sqrt{(x-4)^2 + (y-4)^2} & \text{level-set.} \end{cases} \tag{26}$$

As shown in Fig. 11(a), a distinct pressure jump appears at the drop interface at steady state after the viscous stresses and surface tension have reached a balance. Fig. 11(b) illustrate the velocity field near the interface. It is found that the velocity is continuous across the interface. Fig. 12(a) shows the drop deformation with increasing capillary number. It is observed that our results are in good agreement with those in Hu et al. [22] and Zhou et al. [56]. The evolution of drop deformation obtained with increasing resolution from 64×64 to 512×512 is shown in Fig. 12(b). By measuring the differences between the results of successive resolutions to that of the highest resolution, one can extract the exponent of error-decay $\epsilon \propto \Delta x^p$, as shown in the insert of Fig. 12(b), which implies about second-order convergence.

4.6. Two-fluid Poiseuille flow

A small perturbation introduced at the interface between two viscous horizontal fluid layers [43] in a channel develops a linear instability, where the proper, initially linear growth rate of the instability depends strongly on the accuracy of the interface model. This problem has been widely studied in previous works [3,2,5,10,30]. The set up for this case is shown in Fig. 13. Subscripts 1 and 2 refer to the upper fluid and lower fluid, respectively. As mentioned in [5] the problem is defined by the fluid-height ratio $n = d_2/d_1$, density ratio $r = \rho_2/\rho_1$, viscosity ratio $m = \mu_2/\mu_1$, Reynolds number $Re = \rho_1 d_1 U_0/\mu_1$, surface tension σ and the wave number $\alpha = 2\pi d_1/\lambda$, where λ is wave length of the initial sinusoidal disturbance. The width of the domain is chosen to accommodate one wave length λ, too. The initial velocity field is given by

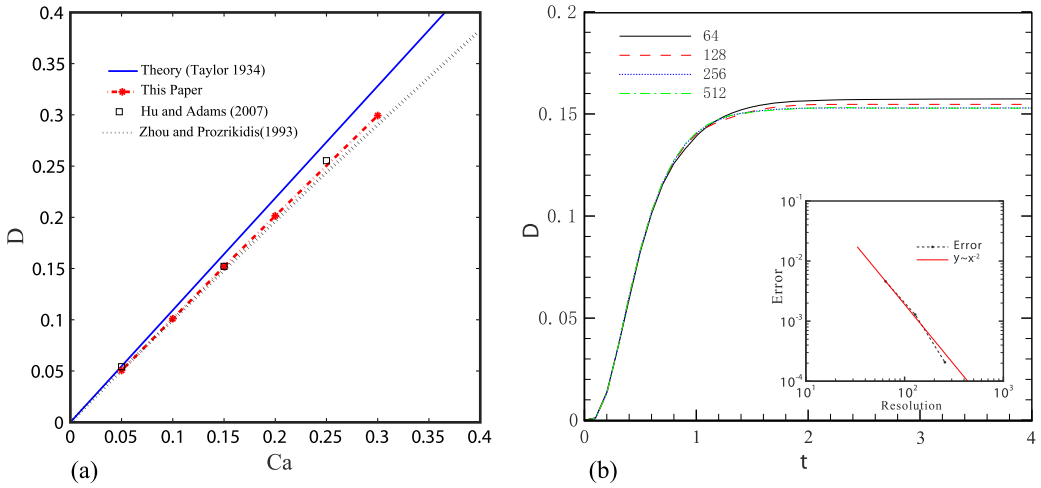

Fig. 12. Drop deformation with (a) capillary numbers (b) different resolutions. The insert in (b) shows the error decay with increasing resolution at $t = 4$.

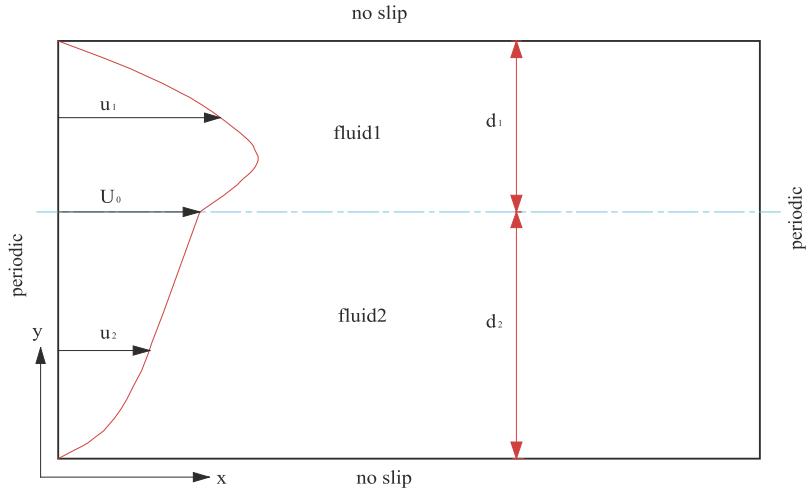

Fig. 13. Set up for viscous Kelvin–Helmholtz simulation.

$$\begin{cases} u_1 = U_0\left[1 + a\left(\dfrac{y-d_2}{d_1}\right) + b\left(\dfrac{y-d_2}{d_1}\right)^2\right] \\ u_2 = U_0\left[1 + \dfrac{a}{m}\left(\dfrac{y-d_2}{d_1}\right) + \dfrac{b}{m}\left(\dfrac{y-d_2}{d_1}\right)^2\right], \\ a = \dfrac{m-n^2}{n(n+1)}, \qquad b = -\dfrac{m+n}{n(n+1)} \end{cases} \tag{27}$$

where U_0 is the interfacial velocity given by

$$U_0 = -\frac{1}{2}\frac{dp}{dx}\frac{d_1 d_2}{\mu_2}\frac{n+1}{m+n}. \tag{28}$$

Note that if periodic boundary conditions are applied in the horizontal direction the constant pressure gradient is expressed as uniform body force [14]

$$f = -\frac{1}{\rho}\frac{dp}{dx}. \tag{29}$$

4.6.1. Linear regime

The growth rate of a small initial single-mode perturbation κ is computed from $A = A_0 e^{kt}$, where A_0 is the initial amplitude. We consider the problem from Nourgaliev et al. [37] without surface tension. The Reynolds number is $Re = 7.1$ and parameters are $\alpha = 2.5133$, $m = 0.5$ and $n = 4$. Initial amplitude of the perturbation is $A_0 = 5.0 \times 10^{-3}$, which is introduced at the interface. Fig. 14 shows that after an initial transient a linear-growth region is recovered with a good convergency by increasing resolution from 256×256 to 1024×1024 grid points. The growth rate is measured by $\ln(A(t_1) -$

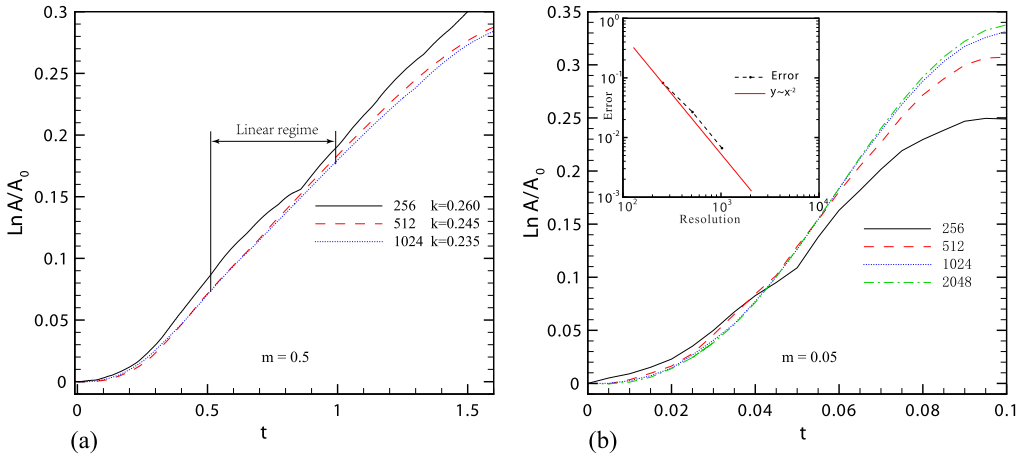

Fig. 14. Linear growth of the perturbation amplitude with different resolutions: (a) The viscosity ratio is set as $m = 0.5$; (a) The viscosity ratio is set as $m = 0.05$. The insert in (b) shows the error decay with increasing resolution at $t = 0.1$.

$A(t_2))/(t_1 - t_2)$, within the line growth regime [5]. We obtain $k \approx 0.235$, which is in good agreement with the exact growth rate of $k = 0.2274$ and the numerical prediction of Nourgaliev et al. [37]. Furthermore, we consider another problem with a viscosity ratio $m = 0.05$. Fig. 14(b) shows the results for increasing resolution from 256×256 to 2048×2048 grid points, which suggests about second-order convergence.

4.6.2. Non-linear regime

For investigating the non-linear region we perform a simulation with an initial sinusoidal perturbation with large amplitude. This problem follows [5], where the initial data are similar to the linear case with $m = 10$, $n = 0.6$, $Re = 5$ and the initial amplitude of perturbation is $A_0 = 0.02$. We consider surface-tension effects with three Weber numbers $We = \infty$, 37.5 and 18.8, where $We = \rho U_0^2 d_v/\sigma$, and d_v is the thickness of the fluid layer with large viscosity. The domain is discretized by a mesh with increasing grid points from 128×128 to 512×512.

The computed interface evolution for all three cases is shown in Fig. 15. We observe that the stretching of filaments increases with increasing *We*. Note that the present results suggest about second-order convergence, and are in very good agreement with the results of Cao et al. [5] and Li et al. [30]. In these works the surface tension is represented as a distributed body force by a smooth Dirac delta function, and also the viscosity is smoothed in a transition region.

4.7. Liquid filament contraction and breakup

The contraction of a stretched liquid filament is simulated to assess the capability of the present method for three dimensional configurations with coupled effects of viscosity and surface tension. The configuration is relevant for several practical applications, such as ink-jet printing. Many theoretical and experimental studies have studied the formation of drops from liquid filaments [6,7,36]. The problem of the contraction of a thin filament, as shown in Fig. 16, has been proposed by Schulkes [47]. The initial shape of the filament is an axisymmetric cylinder with two hemispherical caps at both ends. The half-length of the filament is L, and the hemispherical caps have the same radius R as the cylinder. Whether the filament breaks up into several satellite drops or contracts into a single drop, depends on the aspect ratio of the filament $L_0 = L/R$, and the Ohnesorge number $Oh = \mu/\sqrt{\rho\sigma R}$.

4.7.1. Liquid filament contraction

For liquid filament contraction we follow the experiment by Castrejon-Pita et al. [6]. The initial aspect ratio is $L_0 = 9.0$, and the Ohnesorge number is $Oh = 0.04$ with viscosity 5 m Pa s and surface tension 72 m Nm^{-1}. The initial conditions are

$$\begin{cases} \rho = 1\ \mathrm{kg/m^3}, \quad p_0 = 10^4\ \mathrm{Pa}, \quad B = 7.0 \times 10^2\ \mathrm{Pa}, \\ \gamma = 1.4, \quad \mu = 1.6 \times 10^{-5}\ \mathrm{Pa\,s} \end{cases} \quad \text{air}$$

$$\begin{cases} \rho = 10^3\ \mathrm{kg/m^3}, \quad p_0 = 10^4\ \mathrm{Pa}, \quad B = 1.4 \times 10^5\ \mathrm{Pa}, \\ \gamma = 7.15, \quad \mu = 5.0 \times 10^{-3}\ \mathrm{Pa\,s} \end{cases} \quad \text{liquid filament} \tag{30}$$

$$\varphi = \begin{cases} -0.19 + \sqrt{x^2 + z^2}\ \mathrm{mm} & y < 1.52 \\ -0.19 + \sqrt{x^2 + (y - 1.52)^2 + z^2}\ \mathrm{mm} & y \geq 1.52 \end{cases} \quad \text{level-set.}$$

The computational domain is 1/8 of the physical domain with 2.0 mm in x-direction, 1.0 mm in y-direction and 1.0 mm in z direction, involving $128 \times 64 \times 64$ computational cells.

The computed shape of the contracting filament at several time instants is shown in comparison to the experimental results in Fig. 17. It can be observed that the simulation is in very good agreement with the experiment. When the filament

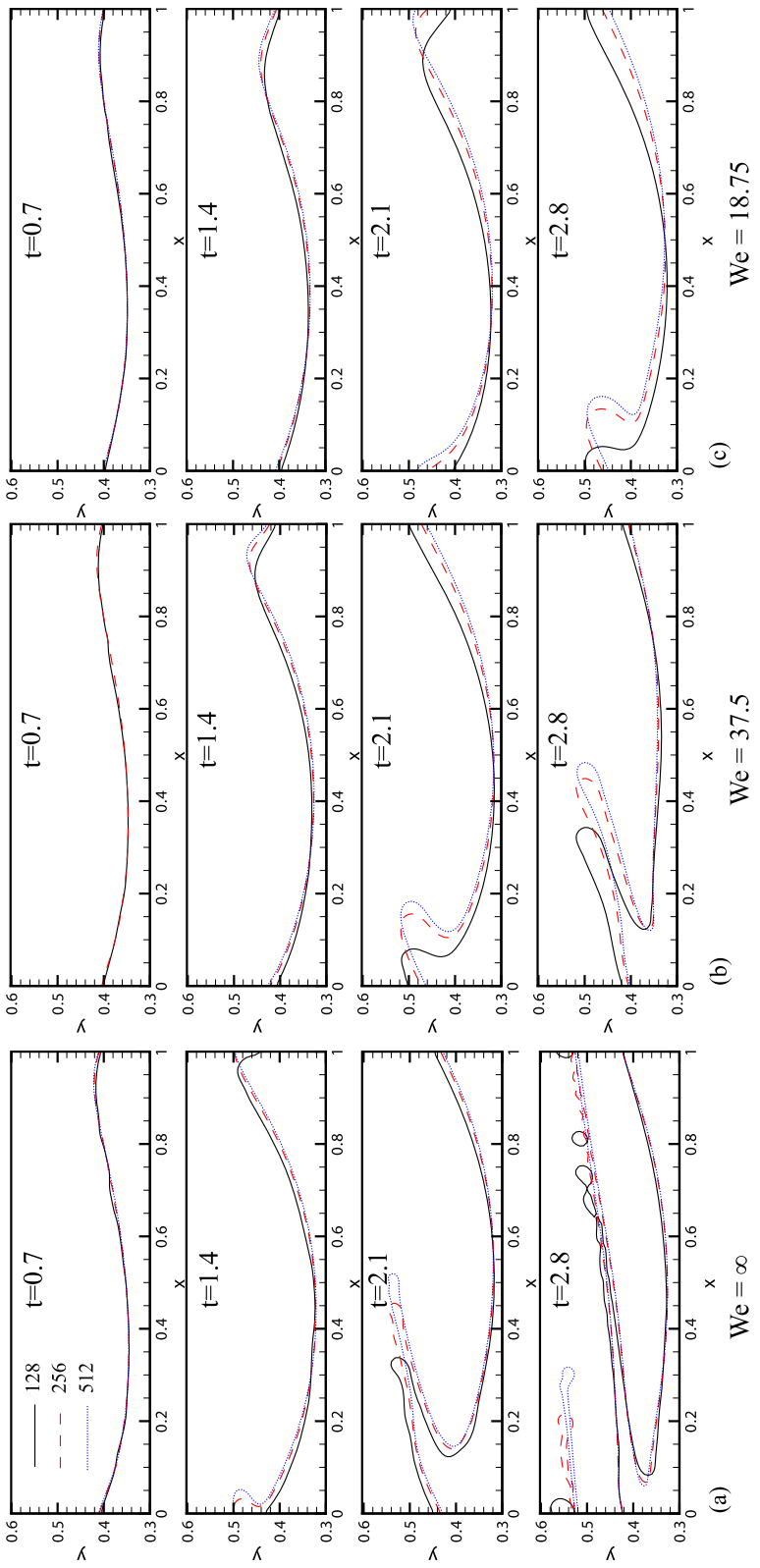

Fig. 15. Time evolution of interfaces for different Weber numbers.

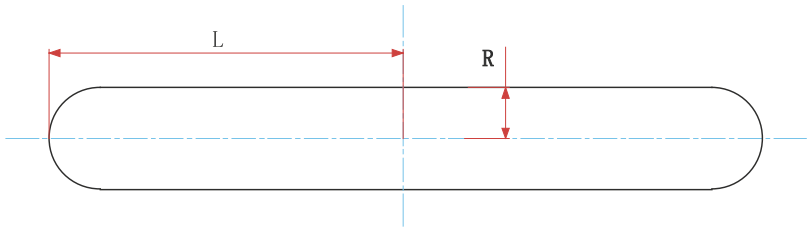

Fig. 16. Geometry of a contracting filament.

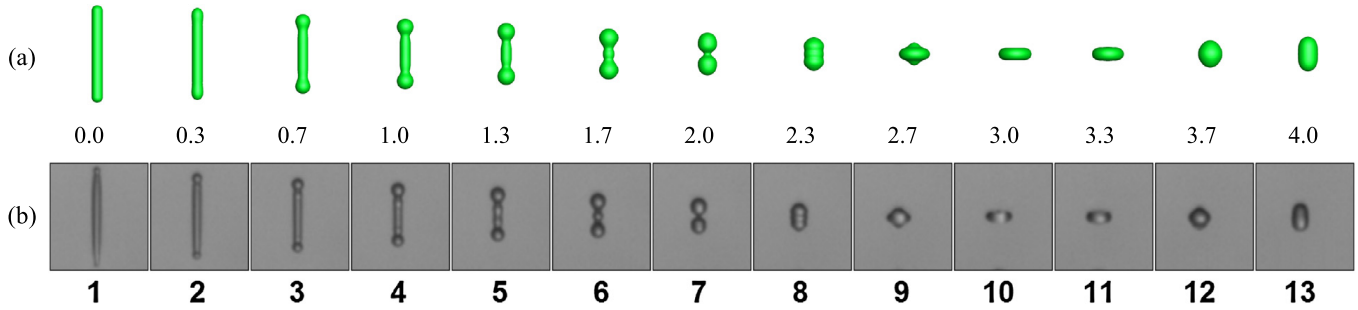

Fig. 17. Evolution of a contract liquid filament: (a) Simulation results; (b) Experiments results in Fig. 4(b) of [6], used with permission.

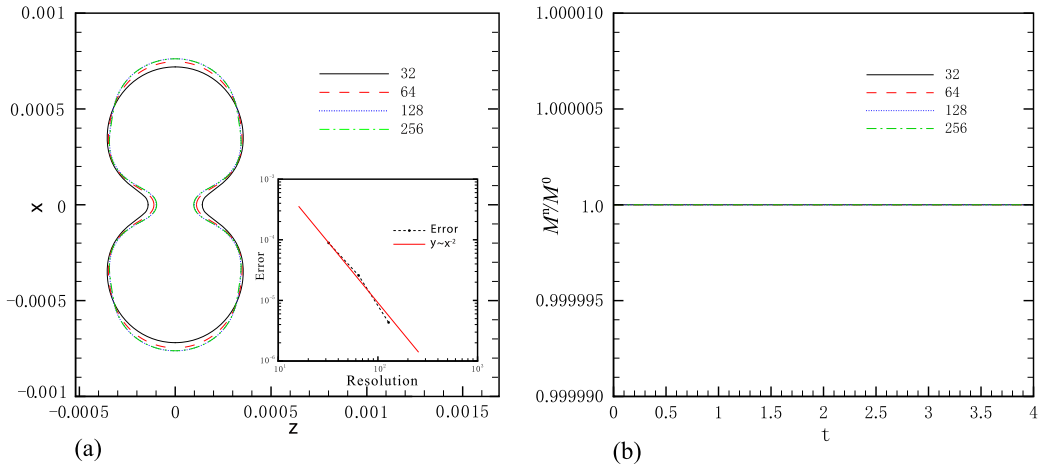

Fig. 18. Convergency and Conservation test: (a) Droplet shapes with various mesh resolution at $t = 2.0$; (b) Time variation of drop mass to its initial value. The insert in (a) shows the error decay with increasing resolution at $x = 0$.

has small aspect ratio, it contracts quickly, due to the fact that the capillary forces are not strong enough to overcome the viscous force to pinch off the neck of filament. Instead, its bulbous ends become larger and expand. Subsequently the filament undergoes a series of oscillations with diminishing amplitudes and finally assumes a spherical drop shape (not shown here). Fig. 18(a) illustrates the droplet shapes with different resolutions at $t = 2.0$, which suggests about second-order convergence. In Fig. 18(b) the relative mass for the filament during the computation is calculated by

$$\frac{M^n}{M^0} = \frac{\sum_{i=0}^{i=N} \alpha^n \rho_i^n}{\sum_{i=0}^{i=N} \alpha^0 \rho_i^0}, \tag{31}$$

where M denotes the total mass of the filament and ρ_i is the cell-averaged mass density of cell i. The superscripts n and 0 represent the nth time step and the initial condition, respectively. It is confirmed that the present method has no conservation error. Additionally, for this case we validate the free surface model proposed in Section 3.4. The liquid filament is regarded as a fluid subjected to the free surface condition, and the external reference pressure is set as the initial air pressure, i.e. $p_0 = 10^4$. The simulation results are the same as that for the case considering the surrounding air. As pointed out by Castrejon-Pita et al. [6], the radius of the filament is much larger than the critical radius ($\mu_{air}\mu_{liquid}/\rho_{liquid}\sigma$), the influence of the air is negligible.

4.7.2. Liquid filament breakup

For the liquid filament breakup, we consider a case with aspect ratio $L_0 = 15$ and Ohnesorge number $Oh = 10^{-2}$, which is taken from [36]. Since the computational domain is quite large for simulating a filament with high aspect ratio, a two-

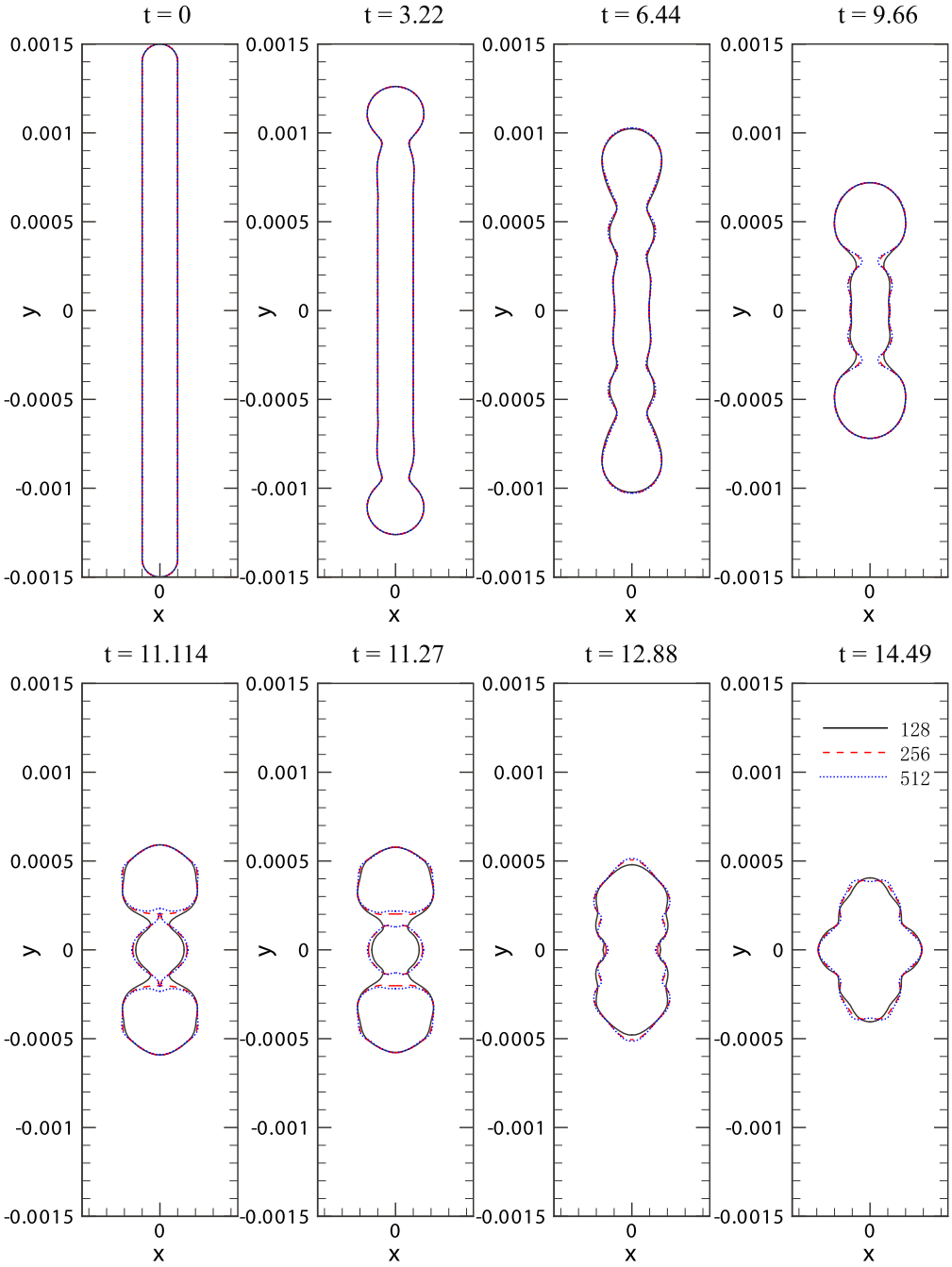

Fig. 19. Evolution of liquid filament breakup.

dimensional axisymmetric model is used to increase computational efficiency. Again the surrounding air is simplified by applying a free-surface boundary condition. The computational domain is 0.4 mm $\times$ 1.6 mm with increasing resolutions from 128×512 to 512×2048. The initial conditions are

$$\begin{cases} \rho = 10^3\ \mathrm{kg/m^3}, \quad p_0 = 10^4\ \mathrm{Pa}, \quad B = 2.8 \times 10^5\ \mathrm{Pa}, \\ \gamma = 7.15, \quad \mu = 10^{-3}\ \mathrm{Pa\,s}, \quad \sigma = 100\ \mathrm{m\,Nm^{-1}} \end{cases} \quad \text{liquid}$$

$$\varphi = \begin{cases} -0.1 + |x|\ \mathrm{mm} & y < 14 \\ -0.1 + \sqrt{x^2 + (y-14)^2}\ \mathrm{mm} & y \geq 14 \end{cases} \quad \text{level-set.} \tag{32}$$

Fig. 19 shows the evolution of the liquid filament. First, bulbous ends form on the contracting filament at $t = 3.22$. Capillary waves appear on the surface of the filament, which give rise to the typical shape before breakup. Because of the thinning neck the capillary force dominates the viscous force and the bulbous ends pinch-off from the filament. Soon after breakup, the drops merge together due to the inertia effects. While the results are in good agreement with Notz et al. [36], they achieve good mesh convergence even after liquid filament breakup, as shown in Fig. 19.

Note that, the method of Notz et al. [36] recovers the evolution only up to the breakup point because the emptying of the thinning necks is inhibited in their finite element model, whereas the present simulation captures the shape after the liquid breakup. For higher resolution of 256×1024 or 512×2048, the filament breaks up at $t = 11.114$, which may generate some complex-interface cells. Without the subcell-resolution reconstruction, the simulation fails due to erroneous evaluation of volume fraction and cell-face apertures.

5. Concluding remarks

In this paper, we have developed a conservative sharp-interface method for incompressible flows using the weakly compressible model. Since the method is constructed based on its compressible version, the original conservative interfacial-flux formulation and simplicity are maintained. By a subcell-resolution approach for evaluating the volume fraction and cell face aperture of computational cell cut by the interface, the accuracy of interface reconstruction is ensured without resorting to complex and time-consuming operations for identifying ambiguous topologies. The viscous stress at the interface is directly imposed on the interfacial-flux to ensure conservation of momentum by a simple formulation of effective viscosity. The pressure jump due to surface tension is imposed consistently after solving the constrained Riemann problem. While the numerical results of a number of validation tests show that the method is robust, accurate, and capable of handling large density and viscosity ratios and high surface tension, extensive simulations of two- and three-dimensional example problems which are compared with experiments or previous results demonstrate the reliability of the proposed method.

Acknowledgements

The first author has partially been financed by China Scholarship Council (No. 2010629044). The authors thank Alfonso Castrejon-Pita (Oxford University) for providing the experimental image on liquid filament contraction.

Appendix A. Algorithm to calculate cell-face aperture and volume fraction

In Lauer et al. [29] the volume fraction is estimated by a sum of triangle areas in two-dimensions and pyramid volumes in three-dimensions for simplicity. For a simple-interface cell in two-dimensions the cell-face apertures are calculated in the same way as in Hu et al. [25], whereas the interface segment-length is evaluated as

$$\Delta\Gamma_{i,j} = \left[(A_{i+1/2,j} - A_{i-1/2,j})^2 + (A_{i,j+1/2} - A_{i,j-1/2})^2\right]^{1/2}. \tag{A.1}$$

As shown in Fig. 20 in two-dimensions, the cut cell is reconstructed through triangles that meet at the cell center. Thus, the volume fraction is the sum of the areas of these triangles,

$$\alpha^m_{i,j} = \frac{1}{2}\left(\frac{1}{2}A_{i-1/2,j} + \frac{1}{2}A_{i,j-1/2} + \frac{1}{2}A_{i+1/2,j} + \frac{1}{2}A_{i,j+1/2} + \Delta\Gamma_{i,j}\varphi_c\right), \tag{A.2}$$

where m indicates the fluid represented by positive level-set value, and φ_c is the level set, representing the distance from the cell center to the interface.

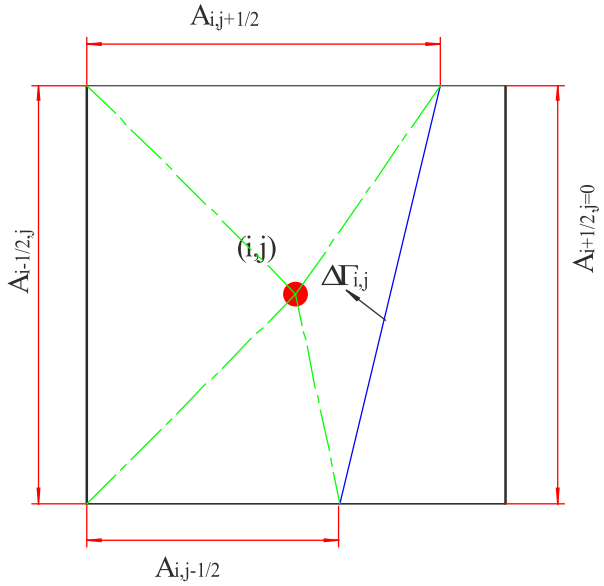

Fig. 20. Scheme for calculating the volume fraction of a cut cell in two dimensions.

This procedure can be extended to three-dimensions in a straightforward way, where the volume fraction is evaluated by a sum of pyramids as

$$\begin{aligned}\Delta\Gamma_{i,j,k} &= \left[(A_{i+1/2,j,k} - A_{i-1/2,j,k})^2 + (A_{i,j+1/2,k} - A_{i,j-1/2,k})^2 \right.\\ &\quad \left. + (A_{i,j,k+1/2} - A_{i,j,k-1/2})^2\right]^{1/2},\\ \alpha^m_{i,j,k} &= \frac{1}{3}\left(\frac{1}{2}A_{i-1/2,j,k} + \frac{1}{2}A_{i+1/2,j,k} + \frac{1}{2}A_{i,j-1/2,k} + \frac{1}{2}A_{i,j+1/2,k}\right.\\ &\quad \left. + \frac{1}{2}A_{i,j,k+1/2} + \frac{1}{2}A_{i,j,k+1/2} + \Delta\Gamma_{i,j,k}\varphi_c\right). \end{aligned} \tag{A.3}$$

Note that, the cell-face apertures in three-dimensions are computed in the same way as the volume fractions in two-dimensions.

References

[1] W. Bo, X. Liu, J. Glimm, X. Li, A robust front tracking method: verification and application to simulation of the primary breakup of a liquid jet, SIAM J. Sci. Comput. 33 (4) (2011) 1505–1524.
[2] Thomas Boeck, Jie Li, Enrique López-Pagés, Philip Yecko, Stéphane Zaleski, Ligament formation in sheared liquid–gas layers, Theor. Comput. Fluid Dyn. 21 (1) (2007) 59–76.
[3] Thomas Boeck, Stéphane Zaleski, Viscous versus inviscid instability of two-phase mixing layers with continuous velocity profile, Phys. Fluids 17 (3) (2005) 032106.
[4] J.U. Brackbill, Douglas B. Kothe, C. Zemach, A continuum method for modeling surface tension, J. Comput. Phys. 100 (2) (1992) 335–354.
[5] Qing Cao, Kausik Sarkar, Ajay K. Prasad, Direct numerical simulations of two-layer viscosity-stratified flow, Int. J. Multiph. Flow 30 (12) (2004) 1485–1508.
[6] Alfonso A. Castrejon-Pita, J.R. Castrejon-Pita, I.M. Hutchings, Breakup of liquid filaments, Phys. Rev. Lett. 108 (7) (2012) 074506.
[7] J.R. Castrejon-Pita, N.F. Morrison, O.G. Harlen, G.D. Martin, I.M. Hutchings, Experiments and Lagrangian simulations on the formation of droplets in continuous mode, Phys. Rev. E 83 (1) (2011) 016301.
[8] Chih-Hao Chang, Xiaolong Deng, Theo G. Theofanous, Direct numerical simulation of interfacial instabilities: a consistent, conservative, all-speed, sharp-interface method, J. Comput. Phys. (2013) 946–990.
[9] Shiyi Chen, Gary D. Doolen, Lattice Boltzmann method for fluid flows, Annu. Rev. Fluid Mech. 30 (1) (1998) 329–364.
[10] A.V. Coward, Y.Y. Renardy, Temporal evolution of periodic disturbances in two-layer Couette flow, J. Comput. Phys. 361 (1997) 346–361.
[11] D. Enright, R. Fedkiw, J. Ferziger, I. Mitchell, A hybrid particle level set method for improved interface capturing, J. Comput. Phys. 183 (1) (2002) 83–116.
[12] Asghar Esmaeeli, Grétar Tryggvason, Computations of film boiling. Part I: Numerical method, Int. J. Heat Mass Transf. 47 (25) (2004) 5451–5461.
[13] Ronald P. Fedkiw, Tariq Aslam, Barry Merriman, Stanley Osher, A non-oscillatory Eulerian approach to interfaces in multimaterial flows (the ghost fluid method), J. Comput. Phys. 152 (2) (1999) 457–492.
[14] H. Foysi, S. Sarkar, R. Friedrich, Compressibility effects and turbulence scalings in supersonic channel flow, J. Fluid Mech. 509 (1) (2004) 207–216.
[15] D.E. Fyfe, E.S. Oran, M.J. Fritts, Surface tension and viscosity with Lagrangian hydrodynamics on a triangular mesh, J. Comput. Phys. 76 (2) (1988) 349–384.
[16] James Glimm, Xiaolin Li, Yingjie Liu, Zhiliang Xu, Ning Zhao, Conservative front tracking with improved accuracy, SIAM J. Numer. Anal. 41 (5) (2003) 1926–1947.
[17] L.H. Han, X.Y. Hu, N.A. Adams, Adaptive multi-resolution method for compressible multi-phase flows with sharp interface model and pyramid data structure, J. Comput. Phys. 262 (4) (2014) 131–152.
[18] D.J.E. Harvie, M.R. Davidson, M. Rudman, An analysis of parasitic current generation in volume of fluid simulations, Appl. Math. Model. 30 (10) (October 2006) 1056–1066.
[19] C.W. Hirt, A.A. Amsden, J.L. Cook, An arbitrary Lagrangian–Eulerian computing method for all flow speeds, J. Comput. Phys. 135 (2) (1997) 203–216.
[20] Cyril W. Hirt, Billy D. Nichols, Volume of fluid (VoF) method for the dynamics of free boundaries, J. Comput. Phys. 39 (1) (1981) 201–225.
[21] X.Y. Hu, N.A. Adams, A multi-phase SPH method for macroscopic and mesoscopic flows, J. Comput. Phys. 213 (2) (2006) 844–861.
[22] X.Y. Hu, N.A. Adams, An incompressible multi-phase SPH method, J. Comput. Phys. 227 (1) (2007) 264–278.
[23] X.Y. Hu, N.A. Adams, M. Herrmann, G. Iaccarino, Multi-scale modeling of compressible multi-fluid flows with conservative interface method, in: Proceedings of the Summer Program, Center for Turbulence Research, 2010, pp. 301–311.
[24] X.Y. Hu, B.C. Khoo, An interface interaction method for compressible multifluids, J. Comput. Phys. 198 (1) (2004) 35–64.
[25] X.Y. Hu, B.C. Khoo, N.A. Adams, F.L. Huang, A conservative interface method for compressible flows, J. Comput. Phys. 219 (2) (2006) 553–578.
[26] Didier Jamet, David Torres, J.U. Brackbill, On the theory and computation of surface tension: the elimination of parasitic currents through energy conservation in the second-gradient method, J. Comput. Phys. 182 (1) (2002) 262–276.
[27] G.S. Jiang, C.W. Shu, Efficient implementation of weighted ENO schemes, J. Comput. Phys. 126 (1996) 202–228.
[28] M. Kang, R.P. Fedkiw, X.D. Liu, A boundary condition capturing method for multiphase incompressible flow, J. Sci. Comput. 15 (3) (2000) 323–360.
[29] E. Lauer, X.Y. Hu, S. Hickel, N.A. Adams, Numerical modelling and investigation of symmetric and asymmetric cavitation bubble dynamics, Comput. Fluids 69 (2012) 1–19.
[30] Jie Li, Yuriko Y. Renardy, Michael Renardy, A numerical study of periodic disturbances on two-layer Couette flow, Phys. Fluids 10 (1998) 3056.
[31] H. Liu, S. Krishnan, S. Marella, H.S. Udaykumar, Sharp interface Cartesian grid method ii: A technique for simulating droplet interactions with surfaces of arbitrary shape, J. Comput. Phys. 210 (1) (2005) 32–54.
[32] William E. Lorensen, Harvey E. Cline, Marching cubes: a high resolution 3D surface construction algorithm, in: ACM Siggraph Computer Graphics, vol. 21, ACM, 1987, pp. 163–169.
[33] T.S. Lundgren, N.N. Mansour, Oscillations of drops in zero gravity with weak viscous effects, J. Fluid Mech. 194 (1988) 479–510.
[34] T. Menard, S. Tanguy, A. Berlemont, Coupling level set/Vof/ghost fluid methods: validation and application to 3D simulation of the primary break-up of a liquid jet, Int. J. Multiph. Flow 33 (5) (2007) 510–524.
[35] Joe J. Monaghan, Simulating free surface flows with SPH, J. Comput. Phys. 110 (2) (1994) 399–406.
[36] P.K. Notz, O.A. Basaran, Dynamics and breakup of a contracting liquid filament, J. Fluid Mech. 512 (1) (2004) 223–256.

[37] R.R. Nourgaliev, M.S. Liou, T.G. Theofanous, Numerical prediction of interfacial instabilities: sharp interface method (SIM), J. Comput. Phys. 227 (8) (2008) 3940–3970.
[38] R.R. Nourgaliev, T.G. Theofanous, S. Wiri, Short communications: Direct numerical simulations of two-layer viscosity-stratified flow, by Qing Cao, Kausik Sarkar, Ajay K. Prasad, IJMF (2004) 30, 1485–1508, Int. J. Multiph. Flow 33 (2007) 786–796.
[39] Stanley Osher, Ronald P. Fedkiw, Level set methods: an overview and some recent results, J. Comput. Phys. 169 (2) (2001) 463–502.
[40] G. Perigaud, R. Saurel, A compressible flow model with capillary effects, J. Comput. Phys. 209 (1) (2005) 139–178.
[41] S. Popinet, S. Zaleski, A front-tracking algorithm for accurate representation of surface tension, Int. J. Numer. Methods Fluids 793 (6) (1999) 775–793.
[42] Rayleigh Lord, On the capillary phenomena of jets, Proc. R. Soc. Lond. 29 (196–199) (1879) 71–97.
[43] Yuriko Y. Renardy, Jie Li, Comment on a numerical study of periodic disturbances on two-layer Couette flow, Phys. Fluids 11 (1999) 3189.
[44] David Salac, Wei Lu, A local semi-implicit level-set method for interface motion, J. Sci. Comput. 35 (2) (2008) 330–349.
[45] Ruben Scardovelli, Stphane Zaleski, Direct numerical simulation of free-surface and interfacial flow, Annu. Rev. Fluid Mech. 31 (1) (1999) 567–603.
[46] Felix S. Schranner, Xiangyu Y. Hu, Nikolaus A. Adams, A physically consistent weakly compressible high-resolution approach to underresolved simulations of incompressible flows, Comput. Fluids (2013) 109–124.
[47] R.M.S.M. Schulkes, The contraction of liquid filaments, J. Fluid Mech. 309 (1996) 277–300.
[48] Chi-Wang Shu, Stanley Osher, Efficient implementation of essentially non-oscillatory shock-capturing schemes, J. Comput. Phys. 77 (2) (1988) 439–471.
[49] Vincenzo Sibillo, Gilberto Pasquariello, Marino Simeone, Vittorio Cristini, Stefano Guido, Drop deformation in microconfined shear flow, Phys. Rev. Lett. 97 (5) (2006) 054502.
[50] M. Sussman, K.M. Smith, M.Y. Hussaini, M. Ohta, R. Zhi-Wei, A sharp interface method for incompressible two-phase flows, J. Comput. Phys. 221 (2) (2007) 469–505.
[51] Mark Sussman, Elbridge Gerry Puckett, A coupled level set and volume-of-fluid method for computing 3D and axisymmetric incompressible two-phase flows, J. Comput. Phys. 162 (2) (2000) 301–337.
[52] Mark Sussman, Peter Smereka, Stanley Osher, A level set approach for computing solutions to incompressible two-phase flow, J. Comput. Phys. 114 (1) (1994) 146–159.
[53] G.I. Taylor, The formation of emulsions in definable fields of flow, Proc. R. Soc. Lond., Ser. A 146 (858) (1934) 501–523.
[54] Salih Ozen Unverdi, Gratar Tryggvason, A front-tracking method for viscous, incompressible, multi-fluid flows, J. Comput. Phys. 100 (1) (1992) 25–37.
[55] Z. Wang, J. Yang, F. Stern, An improved particle correction procedure for the particle level set method, J. Comput. Phys. 228 (16) (2009) 5819–5837.
[56] Hua Zhou, C. Pozrikidis, The flow of suspensions in channels: single files of drops, Phys. Fluids A, Fluid Dyn. 5 (1993) 311.

Appendix B:

Article II

J. Luo, X.Y. Hu N.A. Adams

Curvature boundary condition for a moving contact line

In *Journal of Computational Physics*,Volume 310, 1 Apirl 2016, pp. 329-341, DOI http://dx.doi.org/10.1016/j.jcp.2016.01.024.

II

Contribution: My contribution to this work was the development of the method and the corresponding computer code for its implementation. I performed simulations and analyzed the results, and wrote the manuscript for the publication.

ELSEVIER LICENSE
TERMS AND CONDITIONS

Aug 09, 2016

This Agreement between Jian Luo ("You") and Elsevier ("Elsevier") consists of your license details and the terms and conditions provided by Elsevier and Copyright Clearance Center.

License Number	3924740521580
License date	Aug 09, 2016
Licensed Content Publisher	Elsevier
Licensed Content Publication	Journal of Computational Physics
Licensed Content Title	Curvature boundary condition for a moving contact line
Licensed Content Author	J. Luo,X.Y. Hu,N.A. Adams
Licensed Content Date	1 April 2016
Licensed Content Volume Number	310
Licensed Content Issue Number	n/a
Licensed Content Pages	13
Start Page	329
End Page	341
Type of Use	reuse in a thesis/dissertation
Portion	full article
Format	both print and electronic
Are you the author of this Elsevier article?	Yes
Will you be translating?	No
Order reference number	
Title of your thesis/dissertation	Conservative sharp interface methods for incompressible multi-phase flow
Expected completion date	Apr 2016
Estimated size (number of pages)	100
Elsevier VAT number	GB 494 6272 12
Requestor Location	Jian Luo Youyi West Road 127 P.O. Box 638 Xi'an, Shaanxi 710072 China Attn: Jian Luo
Total	0.00 EUR
Terms and Conditions	

Journal of Computational Physics 310 (2016) 329–341

Contents lists available at ScienceDirect

Journal of Computational Physics

www.elsevier.com/locate/jcp

Curvature boundary condition for a moving contact line

J. Luo, X.Y. Hu *, N.A. Adams

Institute of Aerodynamics and Fluid Mechanics, Technische Universität München, 85747 Garching, Germany

ARTICLE INFO

Article history:
Received 8 December 2014
Received in revised form 19 January 2016
Accepted 21 January 2016
Available online 25 January 2016

Keywords:
Moving contact line
Dynamic contact angle
Surface tension
Conservative sharp-interface method
Level-set method

ABSTRACT

Effective wall boundary conditions are very important for simulating multi-phase flows involving a moving contact line. In this paper we present a curvature boundary condition to circumvent the difficulties of previous approaches on explicitly imposing the contact angle and with respect to mass-loss artifacts near the wall boundary. While employing the asymptotic theory of Cox for imposing an effective curvature directly at the wall surface, the present method avoids a mismatch between the exact and the numerical contact angles. Test simulations on drop spreading and multi-phase flow in a channel show that the present method achieves grid-convergent results and ensures mass conservation, and delivers good agreement with theoretical, numerical and experimental data.

1. Introduction

Wetting or dewetting of a solid surface occurs in a number of applications, such as coating, lamination, inkjet printing and spray painting [44,33,35]. A phenomenon common to these applications is the moving contact line, where one fluid displaces the other. A fundamental difficulty in the numerical treatment of the contact line arises with the conventional no-slip boundary condition, as it leads to inconsistent, grid-dependent results [10,34].

Various approaches have been proposed to alleviate this problem, such as the slip model [39,37], the precursor film model [28], the diffusive interface model [45], and the multi-scale model combining molecular dynamics and diffusive interface [22]. Convergence of results is controlled by prescribed parameters in these models, such as the slip length in the slip model, the film thickness in the precursor film model, and the interface thickness in the diffusive interface model. With the slip model, a slip length is introduced to replace the no-slip boundary condition. For grid convergence, the mesh size needs to be smaller than the introduced slip length [41]. However, experimental studies suggest that the physical slip length is on the order of the intermolecular distance [8], which is far beyond what can be achieved with acceptable grid resolution [7]. An efficient approach for circumventing extremely small grid sizes is to model the microscopic region near the contact line based on hydrodynamic theories and to resolve only the macroscopic region away from the contact line. Schönfeld and Hardt [29] obtained almost grid-independent results by a combined model with a macroscopic length and a near-wall body force. Similar results are obtained in [1] of Afkhami and Zaleski by modeling the dynamic contact angle based on an analog to Cox's theory. Sui and Spelt [36] revisited and extended this method by considering higher-order terms in Cox's theory.

One difficulty of such methods based on Cox's theory is to solve the complex, implicit integral function relating the microscopic angle to the macroscopic angle, which is either replaced by a simplified form [1,7] or obtained numerically [36]. Another issue associated with the boundary condition is how to compute curvature at the contact line. In numerical simu-

* Corresponding author.
E-mail address: Xiangyu.Hu@tum.de (X.Y. Hu).

http://dx.doi.org/10.1016/j.jcp.2016.01.024
0021-9991/

lations, imposing a contact angle explicitly at the wall is a common way to define the interface in the vicinity of the contact line [2,25,17,20,42]. Afkhami and Zaleski reconstructed a height function at the contact line based on the contact angle for their Volume-of-Fluid method [1]. Also, in Sui and Spelt's approach, an iterative procedure is used to impose the contact angle for their level-set method [36]. Note that, since in these cases the contact angle is defined on the numerical grid, undesirable artifacts can occur due to a mismatch with the exact contact angle which is defined on a length scale much smaller than the grid size. For example, imposing the contact angle explicitly can spuriously displace the zero level-set and the location of contact line, and thus induce large mass-conservation errors [40,26].

In this paper, we rather impose a curvature boundary condition for predicting moving contact lines. An effective curvature is formulated explicitly based on the asymptotic theories of Cox [4], which avoids solving complex, implicit integral function. For simulating incompressible multi-phase flow, we adopt the conservative sharp-interface method, where surface tension and viscosity jump are treated without numerical smearing [18]. Since the present method does not impose the contact angle explicitly on the level-set function representing the interface, it avoids a mismatch between the exact and numerically imposed contact angles and hence spurious level-set displacement and the corresponding mass-conservation errors. Several multi-phase flow problems, including drop spreading on the wall, steady Couette and Poiseuille flows, are considered to demonstrate the ability of the present method. The numerical results suggest grid-convergence and good agreement with previous theoretical, numerical and experimental results.

2. Weakly compressible model

We use a weakly compressible model for incompressible multiphase flows [30,3,19]. The mass and momentum conservation for a weakly compressible flow can be described as

$$\frac{\partial \mathbf{U}}{\partial t} + \nabla \cdot \mathbf{F} = \mathbf{S}, \tag{1}$$

where $\mathbf{U}$ is the density of mass and momentum and $\mathbf{F}$ represents the convective fluxes. On the right-hand side $\mathbf{S} = 0$ for the density component of $\mathbf{U}$, and $\mathbf{S} = \nabla \cdot \mathbf{F}_v + \mathbf{a}_s + \rho \mathbf{g}$ for the momentum components. Here, $\mathbf{F}_v$ are the viscous fluxes. The surface-tension force is given by

$$\mathbf{a}_s = \sigma \kappa \delta_n \mathbf{N} \tag{2}$$

where σ, κ, $\mathbf{N}$ are surface tension, curvature and normal direction of the interface, respectively. δ_n is the Dirac delta distribution

$$\delta(x) = \begin{cases} +\infty & \varphi = 0 \\ 0 & \varphi \neq 0 \end{cases}, \quad \int_{-\infty}^{+\infty} \delta(x) dx = 1, \tag{3}$$

defined in the normal direction of the interface. $\mathbf{g}$ is the gravitational acceleration. To close Eq. (1) an artificial equation of state relating pressure and density is used. Here, we employ Tait's equation

$$\begin{aligned} p &= B[(\frac{\rho}{\rho_0})^\gamma - 1] + p_0 \\ B &= \frac{\rho_0 |v_f|^2}{\gamma M^2} \end{aligned}, \tag{4}$$

where M is the Mach number, γ is an artificial specific heat ratio, v_f denotes a characteristic flow velocity, ρ_0 and p_0 are density and pressure of the fluids at the reference condition, respectively. The artificial sound speed is $c = \sqrt{\frac{\gamma B}{\rho}}$. To impose incompressibility of the fluids, we choose the parameters γ, B and ρ_0 such that the Mach number satisfies $M = \frac{|v_f|}{c} \approx 0.1$.

For weakly compressible multiphase flows, the above governing equation is solved within a framework of the conservative sharp interface method [12], where the underlying conservative scheme on a Cartesian grid is modified for computational cells being cut by the interface. Specifically, the viscosity jump at the interface is directly imposed on the momentum flux across the interface, so that momentum conservation is ensured. A constrained Riemman problem is solved to impose a pressure jump condition due to surface tension. We refer to Luo et al. [18] for details.

For capturing the phase-interface, we use the level-set function φ, which describes the signed distance from the interface to each cell center [21]. The zero-level-set, i.e. $\varphi = 0$, represents the interface Γ. The entire domain is divided into two sub-domains, characterized for two fluids by opposite signs of the level-set function. The level-set field is advanced by

$$\frac{\partial \varphi}{\partial t} + \mathbf{u} \cdot \nabla \varphi = 0, \tag{5}$$

where $\mathbf{u}$ represents the velocity for the level-set obtained from the fluid field [9]. To update the flow field, the governing equations are discretized by a 5th-order WENO-LLF scheme [15] and a 2nd-order TVD Runge–Kutta time integration [31] for individual fluids. The time-step is set according to [38],

$$\Delta t = \mathrm{CFL} \cdot \min\left(\frac{\Delta}{|u|+c}, \frac{\rho\Delta^2}{\mu}, \sqrt{\frac{\rho}{8\pi\sigma}}\Delta^{\frac{3}{2}}\right), \tag{6}$$

where Δ is grid size and μ is dynamic viscosity. We set CFL $= 0.6$ for all the simulations. In addition, a wavelet-based adaptive multi-resolution algorithm is adopted for improving computational efficiency [11].

3. Curvature boundary condition

The boundary condition for a moving contact line is presented in the following. As in Ref. [1] the no-slip boundary condition is employed for fluid fields by defining velocities of the so-called "ghost cells" within the wall with

$$v_g = 2U_w - v, \tag{7}$$

where v is the tangential velocity in the cell adjacent to the wall and U_w is the velocity of the wall. Within a level-set framework the interface curvature in a cut-cell sufficient far away from the moving contact line can be obtained directly from the level-set function. The curvature in a cut-cell with moving contact line is provided by the new curvature boundary condition, since the stencil of the central-difference curvature approximation for this cell is incomplete.

3.1. Curvature far away from the contact line

The curvature of the interface in a cut cell is defined by $\kappa = \nabla \cdot \left(\frac{\nabla\varphi}{|\nabla\varphi|}\right)$, which can be rewritten as

$$\begin{aligned} \kappa &= \frac{\varphi_x^2\varphi_{xx} + \varphi_y^2\varphi_{yy} - 2\left(\varphi_x\varphi_y\varphi_{xy}\right)}{\left(\varphi_x^2+\varphi_y^2+\epsilon\right)^{3/2}} \qquad \text{(2D)} \\ \kappa &= \frac{n_r}{r} + \frac{\varphi_z^2\varphi_{zz} + \varphi_r^2\varphi_{rr} - 2\left(\varphi_z\varphi_r\varphi_{zr}\right)}{\left(\varphi_z^2+\varphi_r^2+\epsilon\right)^{3/2}} \quad \text{(axisymmetric)}, \end{aligned} \tag{8}$$

where ϵ is a small positive number to avoid division by zero [27]. r is the radial coordinate of the cell center, n_r is the component of the normal direction of the interface in the radial direction, defined as $n_r = \varphi_r/(\varphi_r^2+\varphi_z^2)^{1/2}$. Since all the partial derivatives in Eq. (8) usually are computed at the cell center with standard central difference schemes, the curvature κ is estimated at the cell center. The cell-center value is corrected for the distance of the cell center from the interface by approximating the level-set locally by a concentric circle or sphere [18], resulting in

$$\kappa_I = \frac{(N_d-1)\kappa}{N_d - 1 - \varphi\kappa}, \tag{9}$$

where N_d is the number spatial dimensions.

3.2. Effective curvature at the contact line

The curvature at the contact line cannot be obtained directly through Eq. (8) since the stencil of central differences for cells adjacent to the wall would contain ghost cells in the wall. Therefore, we propose an effective curvature for a moving contact line based on the asymptotic theories of Cox [4].

Close to the contact line, which is located in a cut cell adjacent to the wall, the balance between viscous stresses and capillary forces primarily determines the interface profile. Cox provided a general hydrodynamic description of a moving contact line under the condition of a small capillary number Ca_{cl}, where the interface profile and Ca_{cl} follow a logarithmic relation

$$g(\theta_d) = g(\theta_m) + Ca_{cl}\ln(\alpha h). \tag{10}$$

θ_d is the macroscopic contact angle, θ_m is the microscopic angle, α is a prefactor depending on higher-order terms and on the microscopic length scale [4,36]. The function $g(\theta)$ is defined by

$$\begin{aligned} g(\theta) &= \int_0^\theta \frac{\mathrm{d}\theta}{f(\theta,\lambda)} \quad \text{and} \\ f(\theta,\lambda) &= \frac{2\sin\beta\{\lambda^2(\beta^2-\sin^2\beta) + 2\lambda\left(\beta(\pi-\beta)+\sin^2\beta\right) + \left((\pi-\beta)^2-\sin^2\beta\right)\}}{\lambda(\beta^2-\sin^2\beta)\left((\pi-\beta)+\cos\beta\sin\beta\right) + \left((\pi-\beta)^2-\sin^2\beta\right)(\theta-\cos\beta\sin\beta)}, \end{aligned} \tag{11}$$

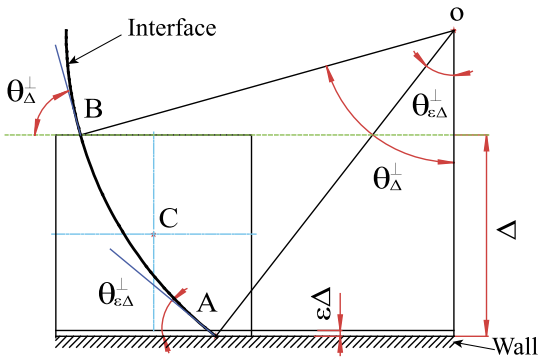

Fig. 1. Schematic of estimating the curvature in a cut cell with contact line.

where λ is the viscosity ratio, and d represents the distance to the contact line. Hence, we can find a macroscopic contact angle at the height $\varepsilon\Delta$ of a thin layer above the wall from Eq. (10)

$$g(\theta^{\perp}_{\varepsilon\Delta}) = g(\theta_m) + Ca_{cl}\ln(\alpha\varepsilon\Delta), \tag{12}$$

where ε is a length scale parameter ($\varepsilon \ll 1$) and the distance to the contact line is $d = \varepsilon\Delta$, which is assumed to be much larger than the intermolecular distance and much smaller than the grid size. Note that, for the non-degenerate cases where the contact angle is sufficient far from 0° or 180°, the thin layer spans only a region much smaller than the mesh size. Therefore, it is natural and reasonable to impose the boundary condition within a single cut-cell adjacent to the wall.

The average curvature in the cut cell containing the contact line can be estimated from the macroscopic contact angles. As in Ref. [5], assuming that the angle $\theta^{\perp}_{\varepsilon\Delta}$ close to the wall changes to the angle $\theta^{\perp}_{\Delta}$ where the phase-interface cuts through the upper cell face, as shown in Fig. 1, the average curvature in this cell adjacent to the wall can be approximated as

$$\begin{aligned}
\kappa_{cl} &= \frac{\cos(\theta^{\perp}_{\Delta}) - \cos(\theta^{\perp}_{\varepsilon\Delta})}{\Delta} \qquad \text{(2D)} \\
\kappa_{cl} &= \frac{n_r}{r} + \frac{\cos(\theta^{\perp}_{\Delta}) - \cos(\theta^{\perp}_{\varepsilon\Delta})}{\Delta} \quad \text{(axisymmetric)},
\end{aligned} \tag{13}$$

where $\theta^{\perp}_{\Delta}$ is estimated directly from the level-set function. For the macroscopic contact angle, $\cos(\theta^{\perp}_{\varepsilon\Delta})$ can be calculated explicitly from Eq. (12) by using the derivative

$$\mathrm{d}g(\theta) = g'(\theta)\mathrm{d}\theta = -\frac{g'(\theta)}{\sin(\theta)}\mathrm{d}\cos(\theta) = -\frac{1}{f(\theta,\lambda)\sin(\theta)}\mathrm{d}\cos(\theta). \tag{14}$$

Combining Eqs. (14) and (12) yields the relationship,

$$\cos(\theta^{\perp}_{\varepsilon\Delta}) \approx \cos(\theta_m) - f(\theta_m,\lambda)\sin(\theta_m)Ca_{cl}\ln(\alpha\varepsilon\Delta). \tag{15}$$

Note that Eq. (15) is valid for different viscosity ratios and for $\lambda = 1$ recovers the simplified relationship of [1]

$$\cos(\theta_{num}) = \cos(\theta_{app}) - 5.63Ca_{cl}\ln(2\Delta/K), \tag{16}$$

where θ_{num} is a contact angle employed as boundary condition for the moving contact line, θ_{app} is a static contact angle, and K is a constant with a dimension of length. From Eq. (13) and Eq. (15) one can define an effective curvature in the cut-cell adjacent to the wall as

$$\begin{aligned}
\kappa_{cl} &= \frac{\cos(\theta^{\perp}_{\Delta}) - \cos(\theta_m) + f(\theta_m,\lambda)\sin(\theta_m)Ca_{cl}\ln(A\Delta)}{\Delta} \qquad \text{(2D)} \\
\kappa_{cl} &= \frac{n_r}{r} + \frac{\cos(\theta^{\perp}_{\Delta}) - \cos(\theta_m) + f(\theta_m,\lambda)\sin(\theta_m)Ca_{cl}\ln(A\Delta)}{\Delta} \quad \text{(axisymmetric)},
\end{aligned} \tag{17}$$

where $A = 2/K$ is introduced as a parameter instead of $\alpha\varepsilon$, and will be discussed further in Secs. 4.2 and 4.4. Also note that the logarithmic term in Eq. (17) can be explained as a curvature correction, which is introduced in accordance to Cox's theory. It is possible to extend the curvature boundary condition to $3D$. Similarly to the axisymmetric case, the effective mean curvature at the contact line can be approximated as

$$\kappa_{cl} = \kappa_w\sqrt{1-(\mathbf{n}_c\cdot\mathbf{n}_w)^2} + \frac{\cos(\theta^{\perp}_{\Delta}) - \cos(\theta_m) + f(\theta_m,\lambda)\sin(\theta_m)Ca_{cl}\ln(A\Delta)}{\Delta}, \tag{18}$$

where κ_w is the contact line curvature, $\mathbf{n}_w$ is the normal direction of the wall and $\mathbf{n}_c$ is the normal direction of the interface near the contact line. Note that estimating Ca_{cl} may be more involved than that in the 2D and axisymmetric cases [16].

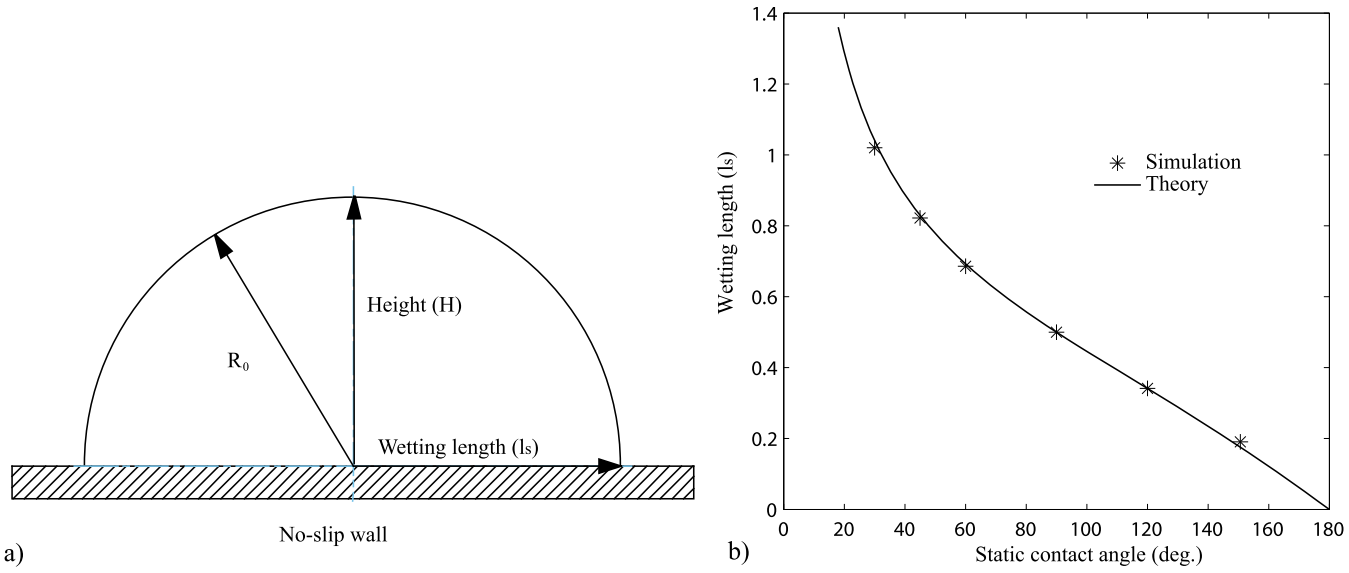

Fig. 2. The equilibrium shape of a drop without gravity: (a) Setup for the drop spreading; (b) Comparison of wetting length (l_s) with the theory.

The procedure of imposing the curvature boundary condition can be summarized as follows:

1. Calculate the curvature κ_I in all cut-cells except those adjacent to the wall from Eqs. (8), (9). For cut-cells adjacent to the wall (containing a contact line), the effective curvature κ_{cl}, is computed from Eq. (17). Note that both κ_I and κ_{cl} are limited by $1/\Delta$ to avoid large erroneous surface tension forces,
2. Solve the interface interaction involving surface tension to obtain the interface condition and the momentum flux at the interface with the sharp interface method of Luo et al. [18].
3. Maintain no-slip boundaries along the wall by Eq. (7), and update the flow field by Eq. (1) with the conservative interface method proposed in [12].
4. Advance the level-set field by Eq. (5) where the advection velocity is obtained from the interface condition [14,18]; level-set values are extrapolated linearly to the ghost cells.

Imposing the exact dynamic contact angle, according to Cox's theory, for simulation of multi-phase flows with moving contact lines, requires to solve the implicit Eqs. (10) and (11) for this angle and then calculate the curvature at contact line. In the present method the effective curvature in a cut-cell with a contact line is approximated directly by Eq. (17), without the need for reconstructing the near-wall interface profile according to the dynamic contact angle. Since the curvature boundary condition does not explicitly impose a contact angle or require the exact location of the contact line, unlike Refs. [40,26], the level-set data at the ghost cells are not modified, and a spurious displacement of the zero level set is avoided. Together with the conservative sharp-interface method [18], mass conservation thus is ensured without extra mass conservation correction [25].

4. Numerical validation and examples

In the following numerical examples are considered to illustrate the capability of the present method for handling moving contact lines. Simulations have been performed in $2D$ (plane or axisymmetric) configurations where analytical solutions, previous numerical results or experimental data are available. We first consider the equilibrium shape of a water drop on a wall to demonstrate that the presented method recovers the static contact angle, when the curvature correction in Eq. (17) vanishes. Then we show spatial convergence for two channel flows, displacement flow and Couette flow. Both of them involve two immiscible fluids and moving contact lines. Finally, we consider drop spreading on a wall and compare the simulation results with experiments to validate the present method. Also, mass conservation is validated by this case.

4.1. Equilibrium shape of a water drop resting on a wall

An equilibrium water drop on a horizontal wall is considered to validate the present boundary condition for problems with a static contact angle. The final shape of the water drop is determined by two parameters, the static contact angle and the Eötvös number $Eo = \rho g R_0^2/\sigma$, where R_0 is the initial radius of the drop. The water drop is initially assumed to be a semi-circle of $R_0 = 0.5$ with the contact angle 90°, resting on the wall, as illustrated in Fig. 2(a). It deforms due to the difference between the transient contact angle and the preset static angle. Also, the presence of gravity flattens the water drop. The computational domain is a 2×2 square with no-slip boundary conditions and discretized by 128×128

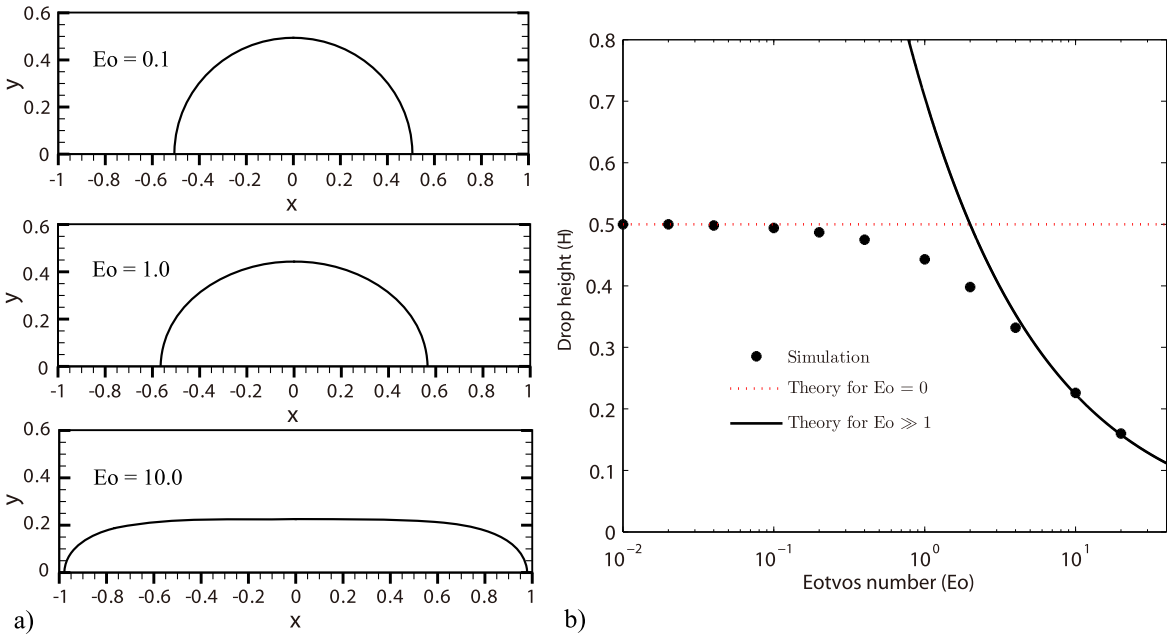

Fig. 3. The equilibrium shape of drop with gravity: (a) The shape of drop with different Eötvös numbers; (b) Drop height as a function of Eötvös number.

grid points. The drop is modeled by a water-like fluid surrounded by a gas-like fluid, and the surface-tension coefficient is set to $\sigma = 7.5$. The initial conditions are

$$\begin{cases} \rho = 10^{-3},\ p_0 = 10^3,\ B = 1.0 \times 10^2,\ \gamma = 1.4,\ \mu = 4.0 \times 10^{-3} & \text{gas} \\ \rho = 1,\ p_0 = 10^3,\ B = 1.0 \times 10^4,\ \gamma = 7.15,\ \mu = 0.25 & \text{drop} \\ \varphi = -0.5 + \sqrt{x^2 + y^2} & \text{level-set} \end{cases}. \tag{19}$$

In the absence of gravity ($Eo = 0$), the equilibrium shape of the water drop is a circular cap that respects the preset static contact angle at the wall, where surface tension on the entire drop reaches a balance [6]. Due to the volume conservation of the water drop in $2D$, the wetting length is expressed as

$$l_s = R_0 \sin\theta_s \sqrt{\frac{\pi/2}{\theta_s - \sin\theta_s \cos\theta_s}}, \tag{20}$$

where θ_s is the static contact angle. In our simulations, unless stated otherwise, the microscopic contact angle in Eq. (12) is assumed to be equal to the static contact angle, i.e. $\theta_m = \theta_s$. Fig. 2(b) shows the numerical results of the wetting length compared with the theoretical results from Eq. (20). We observe that overall the simulation results agree with the theoretical values quite well, except for small discrepancies for very small or large static contact angles. These small discrepancies appear due to the error on estimating the curvature at small or large static contact angles near the contact line [7].

In the presence of gravity the shape of the water drop is determined by a balance between surface tension and gravity [6]. When $Eo \ll 1$, the drop assumes a circular cap shape. The drop height H is given by

$$H = R_0(1 - \cos\theta_s) \sqrt{\frac{\pi/2}{\theta_s - \sin\theta_s \cos\theta_s}}. \tag{21}$$

When $Eo \gg 1$, gravity deforms the water drop until it forms a puddle. The height of the drop is given by

$$H = 2\sqrt{\frac{\sigma}{\rho g}} \sin(\theta_s/2) = \frac{2R_0}{\sqrt{E_0}} \sin(\theta_s/2). \tag{22}$$

For simplicity, the static contact angle is set to $\theta_s = 90°$, so the drop height is $H = R_0 = 0.5$ if gravity is ignored. Fig. 3(a) shows the shapes of a drop at $E_0 = 0.1$, $E_0 = 1.0$, $E_0 = 10.0$, where the water drop resembles a circular cap at small E_0 and a puddle at large E_0. The comparison between simulation and theory for the drop height as function of the Eötvös number is illustrated in Fig. 3(b). The simulation results are in good agreement with the asymptotic solutions given by Eq. (21) and Eq. (22) at small and large E_0 values, respectively. Note that a transition region is observed for moderate values of E_0.

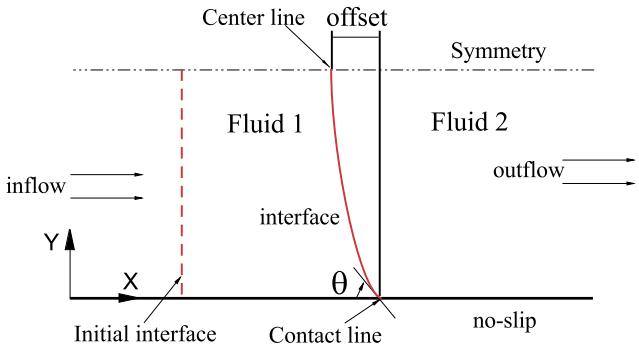

Fig. 4. Definition of displacement flow in a tube.

4.2. Displacement flow in a channel

The simple test of displacement flows in a two-dimensional channel is considered, as shown in Fig. 4. The size of computational domain is 1×8, which is sufficiently long for the interface to develop a steady shape. A symmetry boundary condition is applied at the top of the domain and a no-slip boundary condition at the bottom of the domain. A fully developed Poiseuille flow with an averaged velocity $U = 0.2$ is applied at the left of the domain as inlet boundary condition. At the right of the domain, a zero normal velocity gradient is used as outflow boundary condition.

For simplicity, both *fluid* 1 and *fluid* 2 have the same density and viscosity, i.e. $\rho_1/\rho_2 = 1$, $\lambda = \mu_1/\mu_2 = 1$. The microscopic contact angle is defined from the displacing fluid, which is assumed to be the static advancing angle and set as $\theta_m = 60°$. The initial velocity condition in the channel is set as a fully-developed Poiseuille flow. The initial interface profile is flat, which has no effect on the steady shape [36]. The fluids are both modeled as water-like fluids, and the surface-tension coefficient is set to $\sigma = 1.0$. The initial conditions are

$$\begin{cases} \rho = 1,\ p_0 = 2.0 \times 10^3,\ B = 2.0 \times 10^4,\ \gamma = 7.15,\ \mu = 0.1 & \text{fluids} \\ u = 0.4 \times (1.0 - y^2),\ v = 0 & \text{velocity} \\ \varphi = x - 3.0 & \text{level-set} \end{cases}. \tag{23}$$

The parameter A in Eq. (17) is set to $A = 10^3$ corresponding to a realistic nanometer slip length if the channel radius is on the order of a millimeter [36]. The contact line velocity, U_{cl}, is calculated from the weighted average of fluid velocities,

$$U_{cl} = \frac{\rho_1 u_1 \alpha + \rho_2 u_2 (1-\alpha)}{\rho_1 \alpha + \rho_2 (1-\alpha)}, \tag{24}$$

where α is the volume fraction corresponding to *fluid* 1 in a cut cell, and N_x is the component of the interface normal direction. The capillary number is thereby estimated as

$$Ca_{cl} = \frac{\mu U_{cl}}{\sigma}. \tag{25}$$

Simulations are carried out to investigate grid convergence. Fig. 5(a) shows the steady interface profile of the fully developed flow. The initial flat interface profile develops a meniscus due the motion of the contact line. The interface profile can be characterized by the horizontal distance between the ends of the meniscus curve, denoted as *offset*, as shown in Fig. 4. Fig. 5(b) illustrates the temporal evolution of the interface profile with mesh refinement. It can be seen that second-order mesh convergence is obtained not only for the steady state, but also for the moving contact line.

We further consider an axisymmetric displacement flow in a tube, which is taken from Sui and Spelt [36]. The viscosity and density ratios of the fluids are both set to 0.05, and the microscopic contact angle is set as $\theta_m = 45°$. The initial conditions are

$$\begin{cases} \rho = 1,\ p_0 = 2.0 \times 10^3,\ B = 2.0 \times 10^4,\ \gamma = 7.15,\ \mu = 0.1 & \text{fluid 1} \\ \rho = 0.05,\ p_0 = 2.0 \times 10^3,\ B = 2.0 \times 10^2,\ \gamma = 7.15,\ \mu = 0.005 & \text{fluid 2} \end{cases}. \tag{26}$$

Other parameters are the same as with the above example, but with an axisymmetric setup. The computation is carried out on a mesh with 128×128 grid points. To investigate the effect of parameter A, we simulate this case with $A = 10^3$, 10^4, 3×10^4 and 10^5. Fig. 6(a) shows the interface evolution with different parameters, and Fig. 6(b) shows the steady interface profiles at $t = 8.0$. We compare our numerical results with the theory predicted by Ramé [23] and the numerical result in Sui and Spelt [36]. As shown in Fig. 6(b), there is almost no visible difference between the present result with $A = 3 \times 10^4$ and those predicted by Ramé [23] and Sui and Spelt [36].

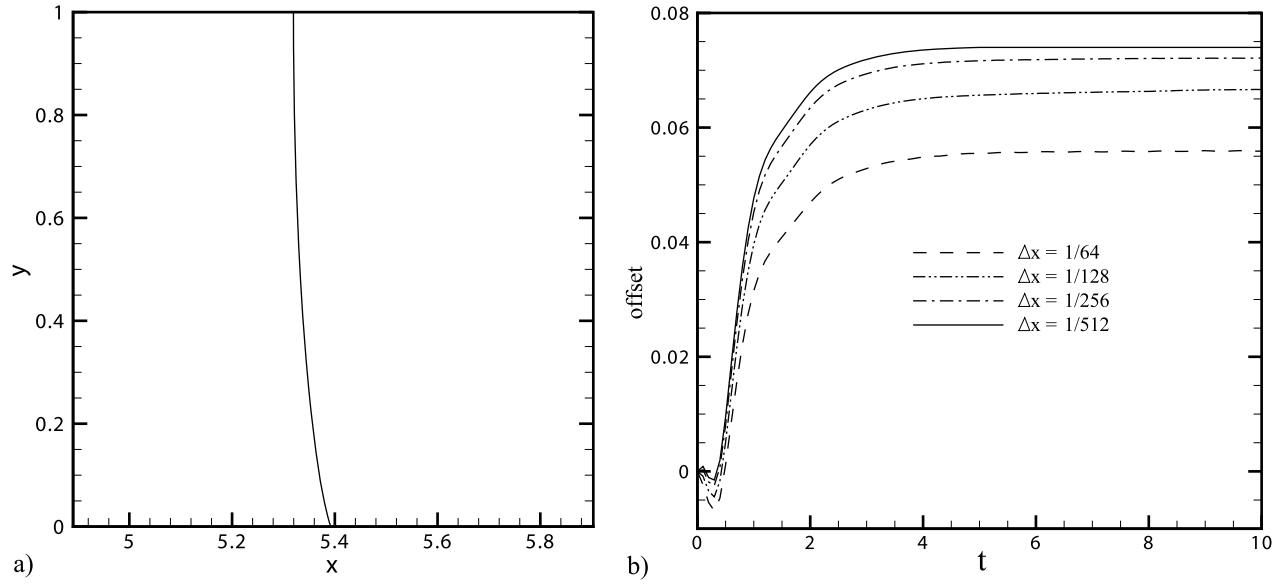

Fig. 5. Evolution of the interface with different grid size.

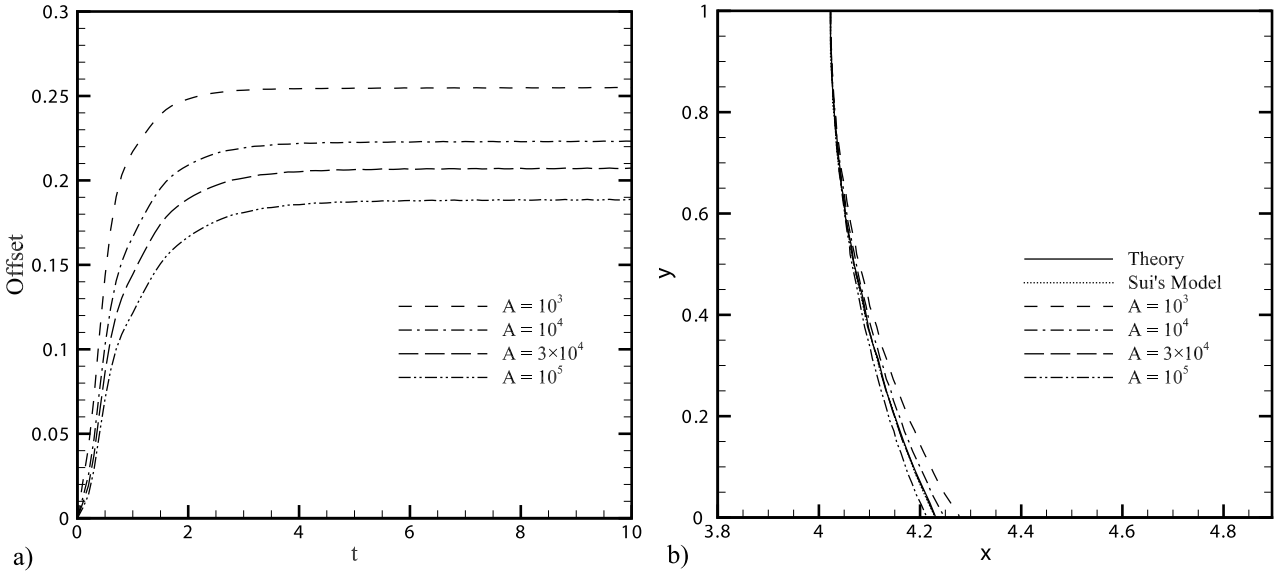

Fig. 6. Interface evolution and steady interface shapes with different parameters: (a) evolution of the offset; (b) steady interface profiles at $t = 8.0$, compared with Ramé [23] and Sui and Spelt [36]; the dotted line represents the result of Sui and Spelt with $\lambda = 10^{-6}$ and $\alpha = 10$ in their method.

4.3. Couette flow

We consider a Couette flow in a channel, where a shear flow is formed between two moving parallel walls. *Fluid* 1 is located in the middle of the channel, surrounded by *Fluid* 2, as shown in Fig. 7. The fully developed interface profile assumes a stationary shape which is determined by the velocity of the moving walls $\pm V_{wall}$ and the microscopic contact angle [22]. Periodic boundary conditions are used in the x direction. The size of the computational domain is 4×1, which is sufficiently long for the interface to develop a steady state.

For simplicity, the two fluids have the same density and viscosity ($\lambda = 1$), and the microscopic contact angle is set to $\theta_m = 90°$. The fluids are both modeled as water-like fluids, and the surface-tension coefficient is set to $\sigma = 2.0$. The initial conditions are

$$\begin{cases} \rho = 1,\ p_0 = 1.0 \times 10^1,\ B = 4.0 \times 10^1,\ \gamma = 7.15,\ \mu = 0.1 & \text{fluids} \\ u = 0,\ v = 0 & \text{velocity} \\ \varphi = \begin{cases} 1.5 - x & \text{if } x < 1.5 \\ x - 2.5 & \text{if } x > 2.5 \\ \max(1.5 - x, x - 2.5) & \text{else} \end{cases} & \text{level-set} \end{cases} . \tag{27}$$

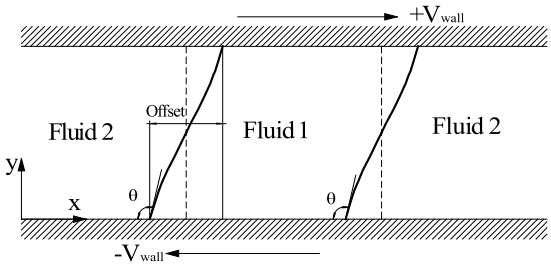

Fig. 7. Steady Couette flow with contact line.

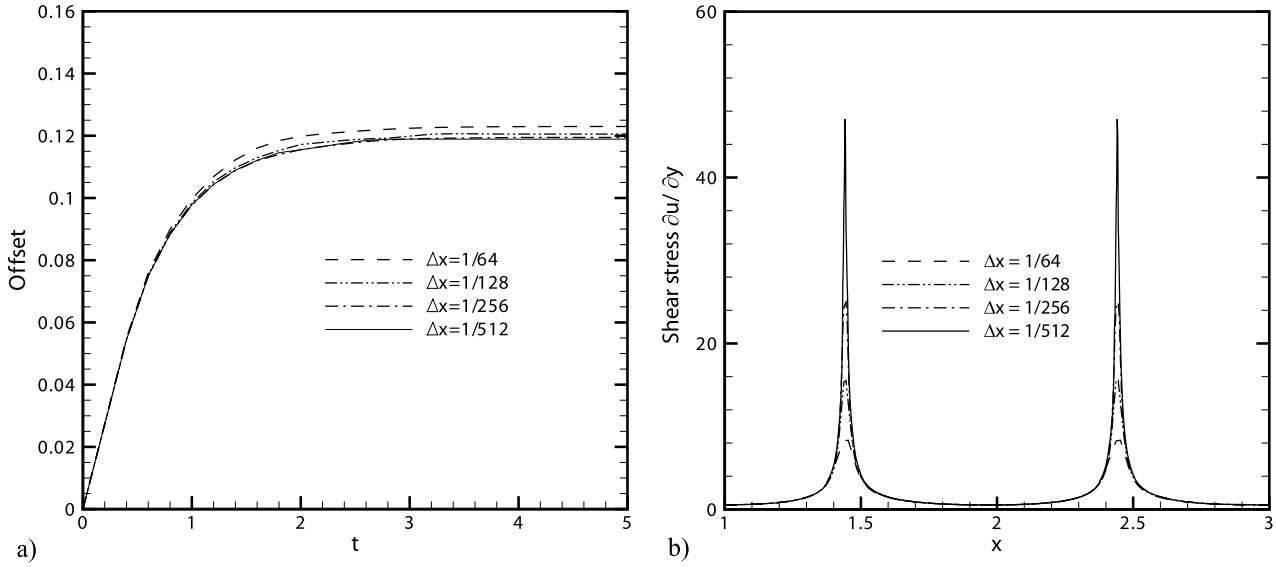

Fig. 8. Couette flow in a channel with the Capillary number $Ca = 0.005$: (a) Convergence test with the mesh refinement; (b) Shear stress along the tube wall with mesh refinement.

The velocity of the moving wall are set to $V_{wall} = 0.1$, with the associated Capillary numbers $Ca = 0.005$. The parameters A in Eq. (17) is set as $A = 10^3$, and the instantaneous capillary number is obtained as follows,

$$Ca_{cl} = \mu U_{cl}/\sigma, U_{cl} = U_I - V_{wall}$$
$$U_I = \frac{\rho_1 u_1 \alpha + \rho_2 u_2 (1-\alpha)}{\rho_1 \alpha + \rho_2 (1-\alpha)} \quad . \tag{28}$$

The velocity of the interface, U_I, is estimated from the weighted average of fluid velocities along the wall.

To investigate grid convergence of the present model, the computational domain is discretized with increasing resolutions from 256×64 to 2048×512 grid points. Fig. 8(a) shows that the simulation results exhibit convergence with mesh refinement, where the offset is defined in Fig. 7. As expected from Ref. [36], the shear stress near the contact line approaches to singularity, as shown in Fig. 8(b), because the microscopic inner region is not resolved. This is only an apparent contradiction to the good convergence properties of the computed interface position and the moving contact angle. The magnitude of curvature correction, as shown in Eqs. (15), (17) and (18), indeed increases with mesh resolution and does not converge. The reason that such diverging quantities do not contaminate the convergence of interface position and moving contact angle can be explained by the force balance between both increasing surface tension and the shear stress [13]. Note that convergence is obtained under the condition that Cox's assumption is valid in a thin layer with thickness much less than the mesh size.

We further conduct two tests with viscosity ratios $\lambda = 1/2$ and $\lambda = 2$, respectively. Unlike imposing a contact angle at the contact line, for which one needs to solve the complex, implicit integral function Eq. (10) and its inverse, with the present method an effective curvature can be formulated explicitly based on $f(\theta, \lambda)$ in Eq. (17). It is shown in Fig. 9(a) that the offset increases with increasing viscosity ratios. In addition, we perform a simulation with $\lambda = 1$ and a larger Capillary number $Ca = 0.01$, which also shows good convergence with mesh refinement in Fig. 9(b). We find about second-order convergence.

4.4. Drop spreading

The last test is the spontaneous spreading of a drop on a wall. We first investigate grid convergence, and then compare the simulation results with experimental data to validate the present method.

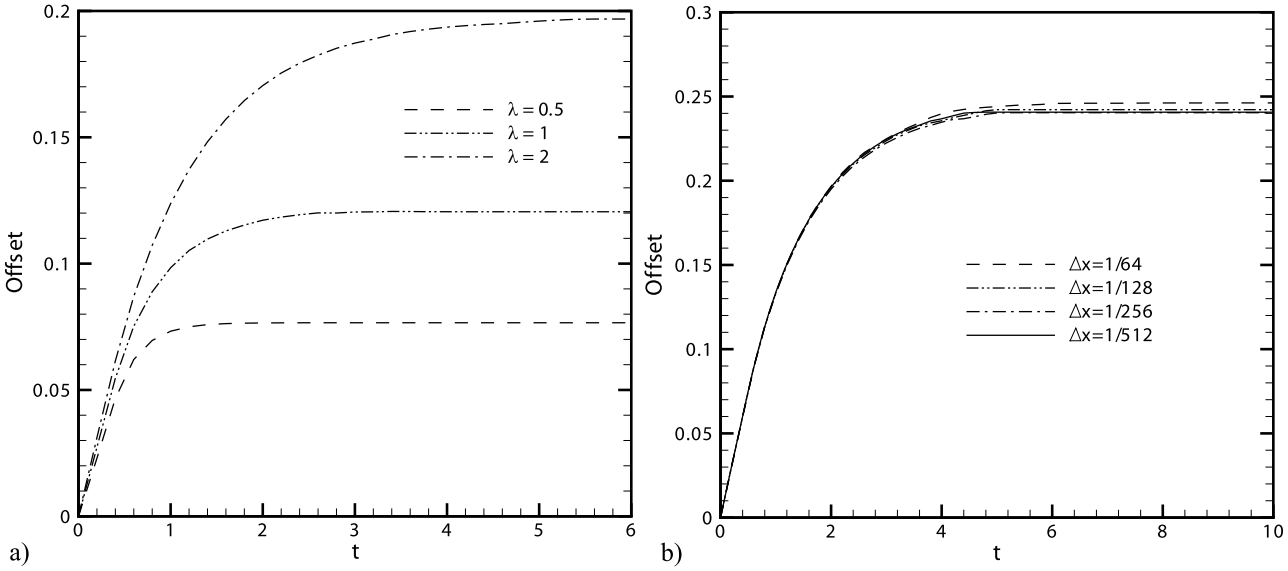

Fig. 9. Couette flow in a channel with different viscosity ratios and Capillary number: (a) $\lambda = 1/2$, $\lambda = 1$, $\lambda = 2$ and $Ca = 0.005$; (b) $\lambda = 1$ and $Ca = 0.01$.

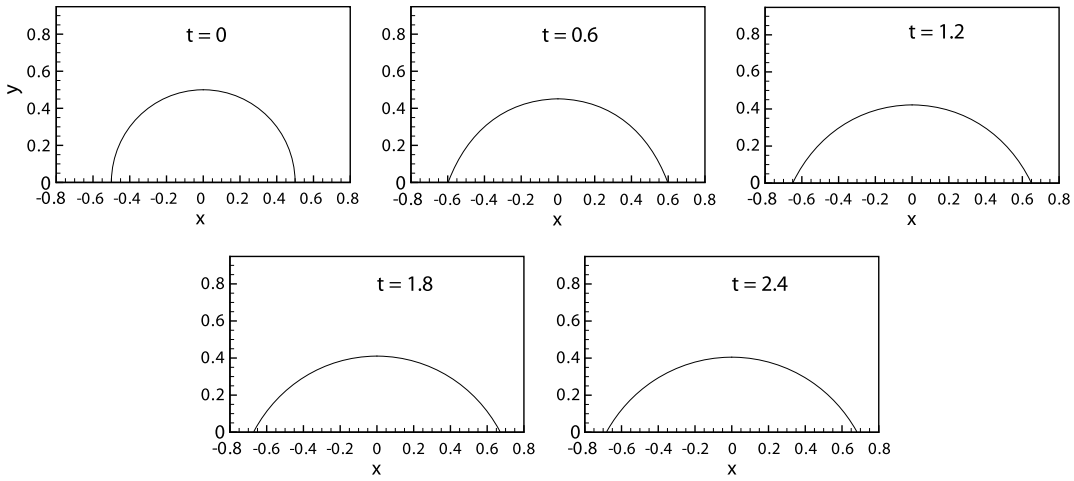

Fig. 10. Drop spreading with static angle $\theta_S = 60°$.

For the grid convergence test, the setup is the same as for the equilibrium test in Sec. 4.1. The water drop is initially assumed to be a semi-circle of $R_0 = 0.5$ with the contact angle 90°, resting on the wall, as illustrated in Fig. 2(a). *Re* and *Ca*, based on the maximum velocity of the flow and the initial radius of the drop R_0, are approximately 2 and 0.03, respectively. The drop spreads until it reaches a static balance at which the contact angle is the static contact angle. The microscopic contact angle is set to the static contact angle, i.e. $\theta_m = \theta_s = 60°$, and the parameters A in Eq. (17) is set to $A = 10^3$. Eq. (24) and Eq. (25) serve to calculate the instantaneous capillary number. The initial conditions are defined by Eq. (19).

Fig. 10 shows the interface profile at several time instants. At time $t = 2.4$ it reaches the steady state, where the macroscopic angle equals the static contact angle. The mesh convergence test in Fig. 11(a), shows that the computed wetting length agrees well with Tanner's law, i.e. $ls \propto t^{1/10}$. Additionally, we investigate the mass conservation of present method in this case. Fig. 11(b) illustrates time variation of drop mass to its initial value. M is defined as $M = \Sigma_{i=1}^{N} \rho_i \alpha_i$, where N the number of cells contained in the drop. M_0 is the value of M at the initial condition. Note that mass conservation is satisfied exactly as expected.

To validate the present method, we conduct a numerical simulation of the drop spreading in axisymmetric coordinates and compare with the experiment in [46]. A drop of radius $R = 1.5$ mm is initially placed on a wall with its center at a height of 1.48 mm above the wall. The corresponding initial contact angle is slightly smaller than 180°. The computational domain is 3.5 mm × 3.5 mm with no slip boundary conditions. Since capillary effects dominate the flow, gravity is neglected. According to the experiment, the microscopic contact angle is set to $\theta_m = 60°$ and the surface-tension coefficient is $\sigma =$ 32 mN/m. The initial conditions are

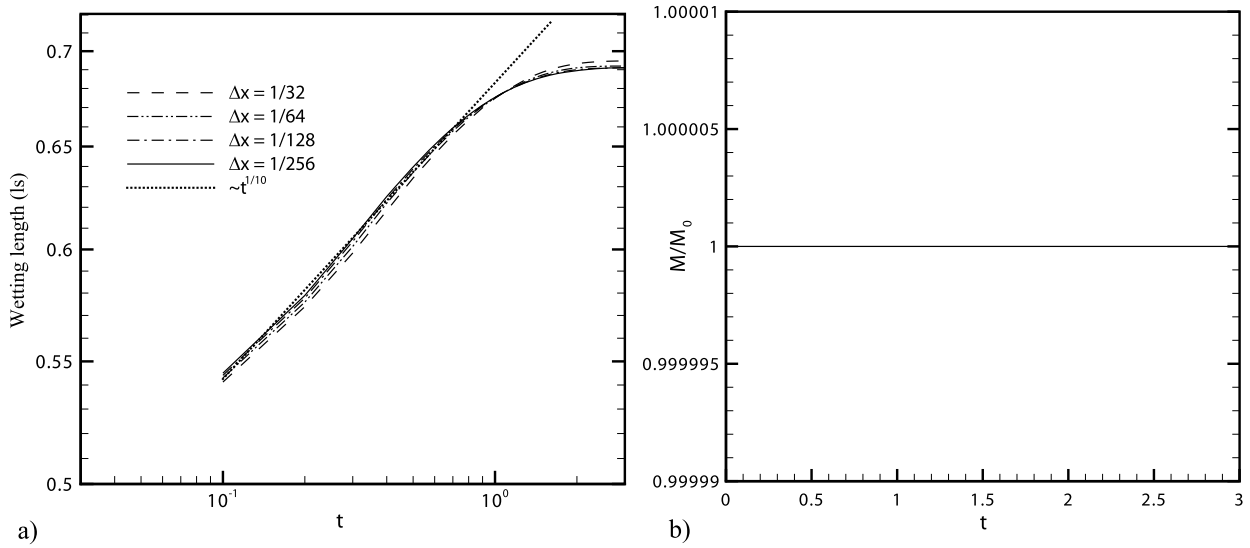

Fig. 11. Convergence and conservation test: (a) Evolution of the wetting length with mesh refinement; (b) Time variation of the drop mass normalized by the initial value.

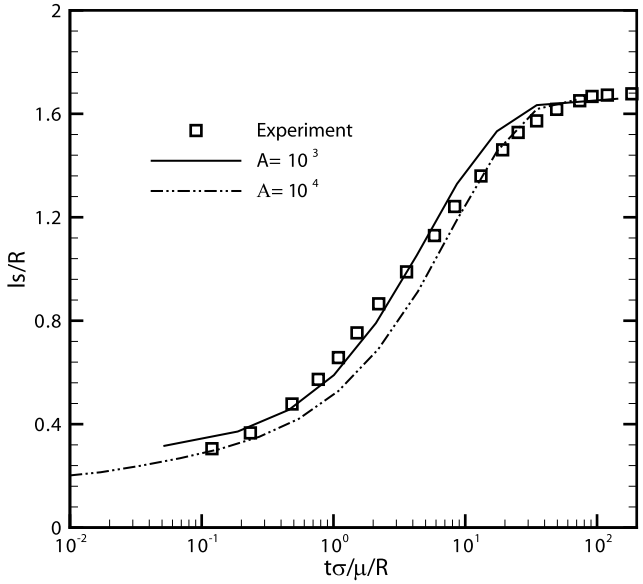

Fig. 12. Drop spreading: comparison between the numerical simulations and experiments.

$$\begin{cases} \rho = 1\ \text{kg/m}^3,\ p_0 = 10^3\ \text{Pa},\ B = 1.0\times 10^2\ \text{Pa}, & \\ \gamma = 1.4,\ \mu = 1.8\times 10^{-5}\ \text{Pa s} & \text{air} \\ \rho = 10^3\ \text{kg/m}^3,\ p_0 = 10^3\ \text{Pa},\ B = 2.0\times 10^4\ \text{Pa}, & \\ \gamma = 7.15,\ \mu = 0.25\ \text{Pa s} & \text{liquid drop} \\ \varphi = -1.5 + \sqrt{x^2 + (y-1.48)^2}\ \text{mm} & \text{level-set} \end{cases} . \tag{29}$$

To investigate the effect of the parameter A on the numerical results, we use $A = 10^3$ and $A = 10^4$ respectively. As addressed in [46], the curves of drop-spreading length ls/R vs. spreading time t for the different liquids collapse onto a master curve by normalizing spreading time with $t\sigma/\mu/R$. In Fig. 12, the normalized numerical results are shown in comparison to the experiment, where the master curve is reproduced from Fig. 7 of [46]. It can be observed that the value of the parameter A determines the speed of drop spreading but has no effect on the equilibrium state. The numerical result for $A = 10^3$ agrees better with the experiment than $A = 10^4$. From this point of view, A can be regarded, similarly as α in Eq. (10), as an adjustable parameter that determines the speed of the contact line. The presence of a small discrepancy may be due to the simple assumption that the microscopic contact angle is the constant static angle, i.e. $\theta_m = \theta_s$. In fact, the microscopic angle rather varies with capillary number [32,43] and kinetic energy dissipation [24].

5. Concluding remarks

A curvature boundary condition is presented for simulating multi-phase flow problems with moving contact line. The boundary condition, which is derived from the theory of Cox, is explicitly defined and valid for variable viscosity ratios. Furthermore, since the present method does not prescribe the value of the contact angle explicitly, the contact-line evolution is determined by the flow field directly, and artifacts by mass-conservation errors are avoided. The numerical model has been tested by comparison with analytical solutions, previous numerical simulations or experiments for several typical problems, including the equilibrium shape of a drop on a wall, displacement flow in a channel, Couette flow in a channel and drop spreading on a wall. The simulation results show that the present method leads to grid-convergent results and ensures mass conservation. Furthermore, while the simulation with the present method is in good agreement with experimental data, the results suggest that further improvement is possible by a model for the microscopic contact angle, which is subject of future studies.

Acknowledgements

The first author has partially been financed by China Scholarship Council (No. 2010629044).

References

[1] S. Afkhami, S. Zaleski, M. Bussmann, A mesh-dependent model for applying dynamic contact angles to VOF simulations, J. Comput. Phys. 228 (15) (2009) 5370–5389.
[2] J.U. Brackbill, Douglas B. Kothe, C. Zemach, A continuum method for modeling surface tension, J. Comput. Phys. 100 (2) (1992) 335–354.
[3] Shiyi Chen, Gary D. Doolen, Lattice Boltzmann method for fluid flows, Annu. Rev. Fluid Mech. 30 (1) (1998) 329–364.
[4] R.G. Cox, The dynamics of the spreading of liquids on a solid surface. Part 1. Viscous flow, J. Fluid Mech. 168 (1986) 169–194.
[5] G. Della Rocca, G. Blanquart, A level set based method to simulate contact line motion and dynamic contact angles for multiphase flow, in: Seventh International Conference on Computational Fluid Dynamics, ICCFD7, Big Island, Hawaii, July 9–13, 2012, p. 2106.
[6] S. Dong, On imposing dynamic contact-angle boundary conditions for wall-bounded liquid–gas flows, Comput. Methods Appl. Mech. Eng. 247–248 (November 2012) 179–200.
[7] Jean-Baptiste Dupont, Dominique Legendre, Numerical simulation of static and sliding drop with contact angle hysteresis, J. Comput. Phys. 229 (7) (2010) 2453–2478.
[8] Jens Eggers, Howard A. Stone, Characteristic lengths at moving contact lines for a perfectly wetting fluid: the influence of speed on the dynamic contact angle, J. Fluid Mech. 505 (April 2004) 309–321.
[9] Ronald P. Fedkiw, Tariq Aslam, Barry Merriman, Stanley Osher, A non-oscillatory Eulerian approach to interfaces in multimaterial flows (the ghost fluid method), J. Comput. Phys. 152 (2) (1999) 457–492.
[10] Michael Griebel, Margrit Klitz, Simulation of droplet impact with dynamic contact angle boundary conditions, in: Michael Griebel (Ed.), Singular Phenomena and Scaling in Mathematical Models, Springer International Publishing, 2014, pp. 297–325.
[11] L.H. Han, X.Y. Hu, N.A. Adams, Adaptive multi-resolution method for compressible multi-phase flows with sharp interface model and pyramid data structure, J. Comput. Phys. 262 (April 2014) 131–152.
[12] X.Y. Hu, B.C. Khoo, N.A. Adams, F.L. Huang, A conservative interface method for compressible flows, J. Comput. Phys. 219 (2) (2006) 553–578.
[13] X.Y. Hu, N.A. Adams, Moving contact line with balanced stress singularities, in: IUTAM Symposium on Advances in Micro- and Nanofluidics, Springer, 2009, pp. 87–94.
[14] X.Y. Hu, B.C. Khoo, An interface interaction method for compressible multifluids, J. Comput. Phys. 198 (1) (2004) 35–64.
[15] G.S. Jiang, C.W. Shu, Efficient implementation of weighted ENO schemes, J. Comput. Phys. 126 (1996) 202–228.
[16] Nicklas Linder, Antonio Criscione, Ilia V. Roisman, Holger Marschall, Cameron Tropea, 3d computation of an incipient motion of a sessile drop on a rigid surface with contact angle hysteresis, Theor. Comput. Fluid Dyn. (2015) 1–18.
[17] H. Liu, S. Krishnan, S. Marella, H.S. Udaykumar, Sharp interface Cartesian grid method II: a technique for simulating droplet interactions with surfaces of arbitrary shape, J. Comput. Phys. 210 (1) (2005) 32–54.
[18] J. Luo, X.Y. Hu, N.A. Adams, A conservative sharp interface method for incompressible multiphase flows, J. Comput. Phys. 284 (2015) 547–565.
[19] Joe J. Monaghan, Simulating free surface flows with SPH, J. Comput. Phys. 110 (2) (1994) 399–406.
[20] C. Narayanan, D. Lakehal, Simulation of filling of microfluidic devices using a coarse-grained continuum contact angle model, in: Technical Proceedings of the 2006 NSTI Nanotechnology Conference and Trade, vol. 2, 2006, pp. 493–496.
[21] Stanley Osher, Ronald P. Fedkiw, Level set methods: an overview and some recent results, J. Comput. Phys. 169 (2) (2001) 463–502.
[22] Tiezheng Qian, Xiao-Ping Wang, Ping Sheng, Molecular scale contact line hydrodynamics of immiscible flows, Phys. Rev. E 68 (1) (2003) 016306.
[23] E. Ramé, On an approximate model for the shape of a liquid–air interface receding in a capillary tube, J. Fluid Mech. 342 (1997) 87–96.
[24] Weiqing Ren, Dan Hu, E. Weinan, Continuum models for the contact line problem, Phys. Fluids 22 (10) (2010) 102103.
[25] Michael Renardy, Yuriko Renardy, Jie Li, Numerical simulation of moving contact line problems using a volume-of-fluid method, J. Comput. Phys. 171 (1) (2001) 243–263.
[26] G. Della Rocca, G. Blanquart, Level set reinitialization at a contact line, J. Comput. Phys. 265 (May 2014) 34–49.
[27] David Salac, Wei Lu, A local semi-implicit level-set method for interface motion, J. Sci. Comput. 35 (2) (2008) 330–349.
[28] N. Savva, S. Kalliadasis, Dynamics of moving contact lines: a comparison between slip and precursor film models, Europhys. Lett. 94 (6) (2011) 64004.
[29] Friedhelm Schönfeld, Steffen Hardt, Dynamic contact angles in CFD simulations, Comput. Fluids 38 (4) (2009) 757–764.
[30] F.S. Schranner, X.Y. Hu, N.A. Adams, A physically consistent weakly compressible high-resolution approach to underresolved simulations of incompressible flows, Comput. Fluids 86 (2013) 109–124.
[31] Chi-Wang Shu, Stanley Osher, Efficient implementation of essentially non-oscillatory shock-capturing schemes, J. Comput. Phys. 77 (2) (1988) 439–471.
[32] Jacco H. Snoeijer, Bruno Andreotti, Moving contact lines: scales, regimes, and dynamical transitions, Annu. Rev. Fluid Mech. 45 (2013) 269–292.
[33] Yangsoo Son, Chongyoup Kim, Doo Ho Yang, Dong June Ahn, Spreading of an inkjet droplet on a solid surface with a controlled contact angle at low Weber and Reynolds numbers, Langmuir 24 (6) (2008) 2900–2907.
[34] J.E. Sprittles, Y.D. Shikhmurzaev, Finite element simulation of dynamic wetting flows as an interface formation process, J. Comput. Phys. 233 (1) (2013) 34–65.
[35] Youngho Suh, Gihun Son, A level-set method for simulation of a thermal inkjet process, Numer. Heat Transf., Part B, Fundam. 54 (2) (2008) 138–156.

[36] Y. Sui, Peter D.M. Spelt, An efficient computational model for macroscale simulations of moving contact lines, J. Comput. Phys. 242 (2013) 37–52.
[37] M. Sussman, A method for overcoming the surface tension time step constraint in multiphase flows II, Int. J. Numer. Methods Fluids 68 (11) (2012) 1343–1361.
[38] Mark Sussman, Elbridge Gerry Puckett, A coupled level set and volume-of-fluid method for computing 3D and axisymmetric incompressible two-phase flows, J. Comput. Phys. 162 (2) (2000) 301–337.
[39] L.H. Tanner, The spreading of silicone oil drops on horizontal surfaces, J. Phys. D, Appl. Phys. 12 (9) (1979) 1473.
[40] Claudio Walker, Bernhard Müller, Contact line treatment with the sharp interface method, MekIT 11 (2013) 451–462.
[41] O. Weinstein, L.M. Pismen, Scale dependence of contact line computations, Math. Model. Nat. Phenom. 3 (2008) 98–107.
[42] Martin Wörner, Numerical modeling of multiphase flows in microfluidics and micro process engineering: a review of methods and applications, Microfluid. Nanofluid. 12 (6) (2012) 841–886.
[43] Yasufumi Yamamoto, Katsunori Tokieda, Tatsuro Wakimoto, Takahiro Ito, Kenji Katoh, Modeling of the dynamic wetting behavior in a capillary tube considering the macroscopic–microscopic contact angle relation and generalized Navier boundary condition, Int. J. Multiph. Flow 59 (February 2014) 106–112.
[44] K. Yokoi, D. Vadillo, J. Hinch, I. Hutchings, Numerical studies of the influence of the dynamic contact angle on a droplet impacting on a dry surface, Phys. Fluids 21 (2009) 72102.
[45] P. Yue, J.J. Feng, Can diffuse-interface models quantitatively describe moving contact lines?, Eur. Phys. J. Spec. Top. 197 (1) (August 2011) 37–46.
[46] A. Zosel, Studies of the wetting kinetics of liquid drops on solid surfaces, Colloid Polym. Sci. 271 (7) (1993) 680–687.

Appendix C:

Article III

J. Luo, X.Y. Hu N.A. Adams

Efficient formulation of scale separation for multi-scale modeling of interfacial flows

In *Journal of Computational Physics*, Volume 308, 1 March 2016, pp. 411-420, DOI http://dx.doi.org/10.1016/j.jcp.2015.11.044.

Contribution: My contribution to this work was the development of the method and the corresponding computer code for its implementation. I performed simulations and analyzed the results, and wrote the manuscript for the publication.

ELSEVIER LICENSE
TERMS AND CONDITIONS

Aug 09, 2016

This Agreement between Jian Luo ("You") and Elsevier ("Elsevier") consists of your license details and the terms and conditions provided by Elsevier and Copyright Clearance Center.

License Number	3924740725696
License date	Aug 09, 2016
Licensed Content Publisher	Elsevier
Licensed Content Publication	Journal of Computational Physics
Licensed Content Title	Efficient formulation of scale separation for multi-scale modeling of interfacial flows
Licensed Content Author	J. Luo,X.Y. Hu,N.A. Adams
Licensed Content Date	1 March 2016
Licensed Content Volume Number	308
Licensed Content Issue Number	n/a
Licensed Content Pages	10
Start Page	411
End Page	420
Type of Use	reuse in a thesis/dissertation
Intended publisher of new work	other
Portion	full article
Format	both print and electronic
Are you the author of this Elsevier article?	Yes
Will you be translating?	No
Order reference number	
Title of your thesis/dissertation	Conservative sharp interface methods for incompressible multi-phase flow
Expected completion date	Apr 2016
Estimated size (number of pages)	100
Elsevier VAT number	GB 494 6272 12
Requestor Location	Jian Luo Youyi West Road 127 P.O. Box 638 Xi'an, Shaanxi 710072 China Attn: Jian Luo
Total	0.00 EUR
Terms and Conditions	

Journal of Computational Physics 308 (2016) 411–420

Contents lists available at ScienceDirect

Journal of Computational Physics

www.elsevier.com/locate/jcp

Efficient formulation of scale separation for multi-scale modeling of interfacial flows

J. Luo [a,b], X.Y. Hu [a,*], N.A. Adams [a]

[a] Institute of Aerodynamics and Fluid Mechanics, Technische Universität München, 85747 Garching, Germany
[b] School of Mechanical Engineering, Northwestern Polytechnical University, 710072 Xi'an, China

ARTICLE INFO

Article history:
Received 24 March 2015
Received in revised form 12 November 2015
Accepted 20 November 2015
Available online 18 December 2015

Keywords:
Multi-scale
Multi-phase
Interfaces
Scale separation
Level-set method

ABSTRACT

We propose an efficient formulation of the scale-separation approach which has been developed by Han et al. [10] for multi-scale sharp interface modeling of multi-phase flows based on the level-set technique. Instead of shifting the entire level-set field twice as in the original method, the improved method identifies the non-resolved interface structures from two auxiliary level-sets close to the interface. Non-resolved structures are separated from the interface by a localized re-distancing method, which increases the computational efficiency considerably compared to the original global reinitialization procedure. Several tests for two-phase flow problems, involving simple and complex interface structures, are carried out to show that the present method maintains sharper interface structures than the original method, and achieves effective scale-separation.

1. Introduction

Simulations of two-phase flow, such as bubble interaction [17], drop impact [7] and spray atomization [2,15], need to resolve length scales that can span several orders of magnitude, which poses a great computational challenge. Adaptive mesh refinement (AMR) [23] and multi-resolution (MR) methods [11,9], even with local time stepping, do not sufficiently reduce computational cost to enable accurate routine simulations of complex interfacial flows. A promising approach to improve efficiency is offered by multi-scale sharp-interface methods [18,14,10]. One essential procedure in multi-scale modeling is scale separation. For a given spatial resolution with grid size h, the interface segments with characteristic size δ can be categorized as resolved if $\delta > h$, or non-resolved if $\delta < h$. In previous work, two approaches have been proposed for scale separation: one is based on the refined level-set grid method (RLSG) [13,18,14], the other is the constrained stimulus–response procedure (CSRP) [10]. While RLSG requires a two-grid system where a higher-resolution grid is used for representing the interface, CSRP uses a single grid for representing both the interface and the individual fluids. CSRP identifies the resolved and non-resolved interface segments based on the different responses they exhibit when subjected to a small shift of the level-set field, and separates these scales with a two-step level-set re-initialization procedure. Although CSRP is effective, in particular the additional re-initialization operation significantly increases computational cost.

In this paper, an improved scale-separation method is proposed to increase computational efficiency. Using two auxiliary level-set fields instead of level-set shifting, the new method identifies non-resolved interface structures by examining the topological consistency between the auxiliary and zero level-sets. Non-resolved structures are subsequently separated by

* Corresponding author.
E-mail address: Xiangyu.Hu@tum.de (X.Y. Hu).

http://dx.doi.org/10.1016/j.jcp.2015.11.044
0021-9991/

a localized re-distancing approach to avoid additional re-initialization operations. The performance of the new method is evaluated through several tests, including single-vortex flow, underwater explosion, shock–bubble interaction, and liquid-filament breakup.

2. Sharp-interface method

The governing flow equations can be written as

$$\frac{\partial \mathbf{U}}{\partial t} + \nabla \cdot \mathbf{F} = \nabla \cdot \mathbf{F}_v, \tag{1}$$

where $\mathbf{U}$ represents the density of mass, momentum and total energy; $\mathbf{F}$ the convective fluxes, and $\mathbf{F}_v$ the viscous fluxes.

To close the governing equations, an equation of states (EOS) must be defined. For an ideal gas, the pressure is determined from

$$p = (\gamma - 1)\rho e, \tag{2}$$

where γ is the ratio of specific heats, ρ is mass density and e internal energy density. For water-like fluids, we use Tait's equation to provide a relation,

$$p = B[(\frac{\rho}{\rho_0})^{\gamma} - 1] + p_0, \tag{3}$$

where ρ_0 and p_0 are the density and pressure of the liquid at the reference condition, respectively, and B is a parameter. For two-phase flows the above governing equations are solved by a conservative-sharp interface method [17,22], where the underlying conservative scheme on a Cartesian grid is modified by considering computational cells cut by the interface. These methods are not only able to cope with violent compressible flows involving strong interface interactions, but also can handle incompressible flow with large density and viscosity ratios and surface tension effects.

For tracking the phase-interface we employ the level-set function, φ, which describes the signed distance from the interface to each cell center [6]. The zero-level-set, $\varphi = 0$, represents the interface Γ. The entire domain is divided into two sub-domains, for two fluids indicated by different signs of the level-set function. The level-set field is propagated by

$$\frac{\partial \varphi}{\partial t} + \mathbf{u} \cdot \nabla \varphi = 0, \tag{4}$$

where $\mathbf{u}$ represents the evolution velocity of the level-set [17]. In practice, the level-set is updated only in a narrow band near the interface, which usually includes nearest cell-layers within $|\varphi| < 4h$. The entire level-set field is re-initialized at every time-step by the following equation [6]

$$\frac{\partial \varphi}{\partial \tau} + \mathrm{sgn}\,(\varphi)\,(|\nabla \varphi| - 1) = 0, \tag{5}$$

in order to maintain the signed-distance property of the level-set, where τ is a fictitious time. To update the flow field, the governing equations of each fluid are discretized by a 5th-order WENO-LLF scheme [19] and a 2nd-order TVD Runge–Kutta time integration [27]. Advection and reinitialization of the level-set field are discretized, respectively, by a 5th-order WENO upwind scheme and a 1st-order upwind scheme [6]. The time-step is set according to Ref. [31],

$$\Delta t = CFL \cdot \min\left(\frac{h}{|u| + c}, \frac{\rho h^2}{\mu}, \sqrt{\frac{\rho}{8\pi\sigma}h^{\frac{3}{2}}}\right), \tag{6}$$

where c is the sound speed. We set CFL = 0.6 for all our simulations. In addition, a wavelet-based adaptive multi-resolution algorithm is adopted for improving computational efficiency [9]. Due to the application of a storage-and-operation-splitting pyramid data structure, this method is able to achieve high memory and computational efficiency. All computations have been conducted on a workstation with 4 quad-core Intel Xeon Processor $E5620$ processors (12M Cache, 2.4 GHz) with 24 GB of RAM. The Intel Threading Building Blocks (TBB) library [4] is used to map logical tasks to physical threads.

3. Scale separation

Non-resolved interface segments are generated during the interface evolution, and are prone to introduce numerical fluctuations or even numerical instabilities, especially for high-resolution simulations of inviscid compressible multi-phase flow problems using the sharp-interface model [10]. They can also lead to unphysical results due to scale-dependent dynamics [18]. An effective approach is to separate them from the resolved scales and treat them differently. For example, in Ref. [10], the well-resolved interface is handled by a sharp interface method, non-resolved interface segments are converted into Lagrangian particles, or they are merged into the opposite phase to maintain mass conservation, or they are deleted.

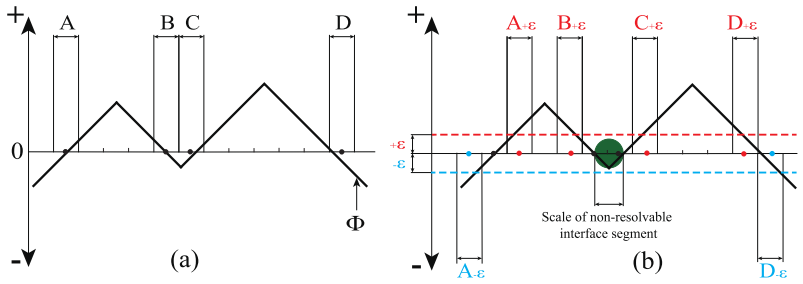

Fig. 1. Schematic of identifying the non-resolved interface segments in one dimension: (a) initial interface level set field and cut cells (block solid dots); (b) corresponding auxiliary cut cells crossed by $\Gamma_{+\varepsilon}$ (red solid dots) and by $\Gamma_{-\varepsilon}$ (blue solid dots). The tick marks indicate the cell faces, and the green mark the non-resolved interface segment. (For interpretation of the references to color in this figure legend, the reader is referred to the web version of this article.)

Similarly to Han et al. [10], the present method applies scale separation as an additional operation just before the reinitialization step of the underlying level set method. Note that the scale-separation operation is independent of the specific choice of the numerical schemes for level-set advection and reinitialization. Therefore, one can use scale-separation also with other level-set schemes, such as those in Enright et al. [5].

3.1. Identifying non-resolved structures

Non-resolved interface segments often manifest themselves as drops and thin filaments with a characteristic length scale of about the grid size h. In the level set field they share a common property, that is the lack of topological consistency among the level-sets near the interface. Such a property corresponds to the large discrepancies induced by the non-resolved interface segments when the reinitialization operations are subjected to a small constant shift of the level set field [10].

Based on this criterion we now develop a new identification method, first in one dimension and then in two dimensions. Assuming a distribution of the level set field on cells near the interface, as sketched in Fig. 1(a), cut cells are those that contain segments of the zero level-set, i.e. A, B, C and D. Other than shifting the entire level-set field by ε as in Ref. [10], we use two auxiliary level-sets, $\varphi = +\varepsilon$ and $\varphi = -\varepsilon$, as shown in Fig. 1(b). As pointed out in Ref. [10], all small interface segments with length scale less than h should be removed, so we also choose $\varepsilon = 0.6h$. We can define two types of cut cells associated with the auxiliary level-sets, the positive auxiliary cut cells $A_{+\varepsilon}, B_{+\varepsilon}, C_{+\varepsilon}, D_{+\varepsilon}$ containing segments of $\varphi = +\varepsilon$ and the negative auxiliary cut cells $A_{-\varepsilon}, D_{-\varepsilon}$ containing segments of $\varphi = -\varepsilon$, as shown in Fig. 1(b).

The cut cells associated with non-resolved interface segments can be identified by checking the auxiliary cut cells in its neighborhood, i.e. the topological consistency between nearby level sets. For a cut cell associated with resolved interface segment, such as Cell A or D in Fig. 1, there are both positive and negative auxiliary cut cells as the nearest neighbors, i.e. topologically consistent between nearby level sets. For a cut cell associated with a non-resolved interface segment, such as Cell B or C, however, there is only either a positive or negative auxiliary cut cell as its nearest neighbor, i.e. topologically inconsistent between nearby level sets. Therefore, the cut cells containing the interface segment marked by a green circle in Fig. 1(b) are uniquely identified.

The extension of such an identification algorithm to two dimensions is illustrated in Fig. 2. First, let S be defined as cut cells crossed by the zero level-set Γ_0,

$$S = \{X_{i,j} | \exists \varphi_{i\pm1/2,j\pm1/2} > 0 \wedge \exists \varphi_{i\pm1/2,j\pm1/2} < 0\}, \tag{7}$$

where $\varphi_{i\pm1/2,j\pm1/2}$ is the level set value at the cell corner approximated by

$$\begin{aligned}
\varphi_{i+1/2,j+1/2} &= \frac{1}{4}\left(\varphi_{i,j} + \varphi_{i+1,j} + \varphi_{i,j+1} + \varphi_{i+1,j+1}\right)\\
\varphi_{i+1/2,j-1/2} &= \frac{1}{4}\left(\varphi_{i,j} + \varphi_{i+1,j} + \varphi_{i,j-1} + \varphi_{i+1,j-1}\right)\\
\varphi_{i-1/2,j+1/2} &= \frac{1}{4}\left(\varphi_{i,j} + \varphi_{i-1,j} + \varphi_{i,j+1} + \varphi_{i-1,j+1}\right)\\
\varphi_{i-1/2,j-1/2} &= \frac{1}{4}\left(\varphi_{i,j} + \varphi_{i-1,j} + \varphi_{i,j-1} + \varphi_{i-1,j-1}\right).
\end{aligned} \tag{8}$$

In Fig. 2(a), S is indicated by cells with back solid dots. Now we define P containing auxiliary cut cells crossed by $\Gamma_{+\varepsilon}$ and N by $\Gamma_{-\varepsilon}$,

$$\begin{aligned}
P &= \{X_{i,j} | \exists \varphi_{i\pm1/2,j\pm1/2} - \varepsilon > 0 \wedge \exists \varphi_{i\pm1/2,j\pm1/2} - \varepsilon < 0\}\\
N &= \{X_{i,j} | \exists \varphi_{i\pm1/2,j\pm1/2} + \varepsilon > 0 \wedge \exists \varphi_{i\pm1/2,j\pm1/2} + \varepsilon < 0\},
\end{aligned} \tag{9}$$

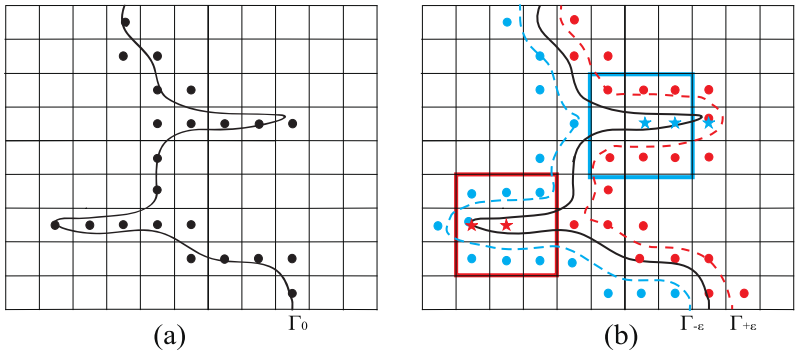

Fig. 2. Identification of the non-resolved interface segments in two dimensions: (a) the initial interface Γ_0 (black solid line) and corresponding cut cells (black solid dots); (b) the auxiliary level-sets $\Gamma_{+\varepsilon}$ (red dash line) and $\Gamma_{-\varepsilon}$ (blue dash line), and corresponding auxiliary cut cells crossed by $\Gamma_{+\varepsilon}$ (red solid dots) and by $\Gamma_{-\varepsilon}$ (blue solid dots). Cut cells whose neighbors contain no red solid dots are indicated by a red star, and Cut cells whose neighbors contain no blue solid dots are indicated by a blue star. (For interpretation of the references to color in this figure legend, the reader is referred to the web version of this article.)

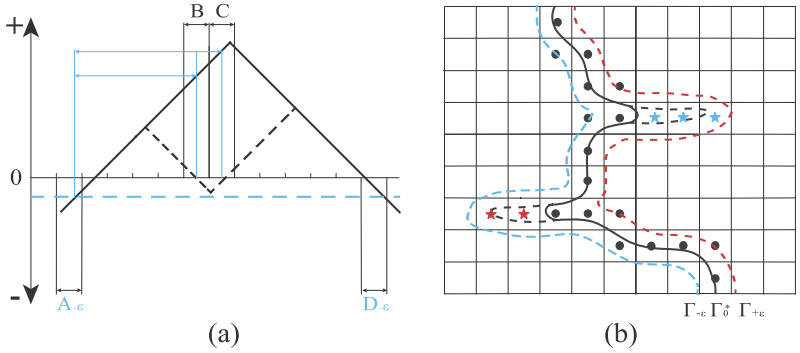

Fig. 3. Interface reconstruction in one and two dimensions: (a) level-set values for the cut cells B and C are calculated from auxiliary cut cell $A_{-\varepsilon}$, (b) level-set values of the cells marked with red stars are calculated from $\Gamma_{+\varepsilon}$ and level-set values of the cells marked with blue stars are calculated from $\Gamma_{-\varepsilon}$. (For interpretation of the references to color in this figure legend, the reader is referred to the web version of this article.)

where ε is $0.75h$ as in Ref. [10]. P and N are indicated with red solid dots and blue solid dots in Fig. 2(b), respectively. Now we can identify a cut cell containing a non-resolved interface segment when its neighbors contain either positive or negative auxiliary cells only

$$S1 = \{X_{i,j} | (X_{i,j} \in S \wedge \forall i_0, j_0 \in \{-1, 0, 1\}), X_{i+i_0, j+j_0} \notin P \vee X_{i+i_0, j+j_0} \notin N\}. \tag{10}$$

Finally, the cut cells associated with resolved interface segments are defined as

$$S2 = S \setminus S1. \tag{11}$$

3.2. Interface reconstruction

After the cut cells containing non-resolved interface segments are identified, one should assign reasonable level-set values for these cells to reconstruct a resolved interface in the corresponding region. In Ref. [12], the level-set value of these cells are simply set as the original level-set values with opposite sign. Such a procedure may introduce artificial disturbances to the interface. We avoid this problem by estimating the level-set value of non-resolved cut cells directly from a re-distancing method. First, the set $S1$ is split into two disjoint subsets, $S1_{\nexists P}$ and $S1_{\nexists N}$. The cut cells are in set $S1_{\nexists P}$,

$$S1_{\nexists P} = \{X_{i,j} | X_{i,j} \in S1 \wedge (\forall (i_0, j_0) \in \{-1, 0, 1\}, X_{i+i_0, j+j_0} \notin P)\}, \tag{12}$$

if their nearest neighbors do not contain any cells in P. The cut cells are in set $S1_{\nexists N}$,

$$S1_{\nexists N} = \{X_{i,j} | X_{i,j} \in S1 \wedge (\forall (i_0, j_0) \in \{-1, 0, 1\}, X_{i+i_0, j+j_0} \notin N)\}, \tag{13}$$

if their nearest neighbors do not contain any cells in N. The level set values for cut cells in $S1_{\nexists P}$ and $S1_{\nexists N}$ are assigned from an estimate of their distance to $\Gamma_{+\varepsilon}$ and $\Gamma_{-\varepsilon}$, respectively. In one dimension, as shown in Fig. 3(a), Cells B and C are in set $S1_{\nexists N}$ and their the level-set values can be estimated from the minimum distance to Cell $A_{-\varepsilon}$ and to $D_{-\varepsilon}$. For the setup in Fig. 3(a), we can obtain corrected level set values $\varphi_B = i_B - i_{A-\varepsilon} + \varphi_{A-\varepsilon}$ and $\varphi_C = i_C - i_{A-\varepsilon} + \varphi_{A-\varepsilon}$, where i_B, i_C and $i_{A-\varepsilon}$ are the indexes of Cells B, C and $A_{-\varepsilon}$, respectively. In two dimensions, the level-set value of cut cells that contain

non-resolved interface segments can be estimated from the minimum distance to the corresponding auxiliary level-sets. To find the minimum distance we define a search region as 9×9 grid cells around the considered cut cell. Assuming that the considered cut cell is in $S1_{\nexists P}$, the distance from this cut cell to the intersection point between the auxiliary level set $\Gamma_{+\varepsilon}$ and the ray cast from the auxiliary cut cell along the normal direction is calculated by

$$d = \sqrt{(i_{s1} - i_p + (\varphi - \varepsilon)N_x)^2 + ((j_{s1} - j_p + (\varphi - \varepsilon)N_y)^2}, \tag{14}$$

where (i_{s1}, j_{s1}) and (i_p, j_p) are the indexes of the considered cut cell in $S1_{\nexists P}$ and the auxiliary cut cell in P, respectively. (N_x, N_y) is the unit normal vector and φ is the level-set value of the auxiliary cut cell (i_p, j_p). The level-set value of the considered cut cell results as

$$\varphi_{i_s, j_s} = -(d_{min} - \varepsilon), \tag{15}$$

where d_{min} is the minimum distance obtained by Eq. (14) for the respective research regions. If there is no auxiliary cut cell within the search region, it indicates that the non-resolved structure is outside of the narrow band beside the well-resolved interface. Note that for a cut cell in $S1_{\nexists N}$ the level set is constructed in the same way, but with $-\varepsilon$ in Eq. (14) and negative sign on the right side of Eq. (15). By correcting the level set values of all cells in S_1, and a well-resolved interface, indicated by a black solid line in Fig. 3(b), is obtained.

The overall procedure of the present method can be summarized as follows:

1. Calculate the level-set values at the cell corners for the entire field from Eq. (8), and identify cells cut by the zero level-set from Eq. (7).
2. Generate two sets of auxiliary cut cells with level set value $\varphi = \pm\varepsilon$ from Eq. (9).
3. Identify whether the cut cells contain non-resolved interface segments from Eq. (10), and classify them into two subsets $S1_{\nexists P}$ and $S1_{\nexists N}$ from Eq. (12) and (13), respectively.
4. Calculate the distance from cut cells that are in $S1_{\nexists P}$ or in $S1_{\nexists N}$ to the corresponding auxiliary level-sets from (14), and correct their level-set values by Eq. (15).

Note that the present method can be extended directly to three dimensions. Also note that, since the present method does not apply level-set shifting and re-initialization of the entire level-set field as in Ref. [10], the computational efficiency is increased considerably.

4. Numerical validation and examples

The following numerical examples are considered to illustrate the capability of the present method to handle interface-scale separation. First, a canonical advection test of a circle in a single-vortex flow is carried out to examine the smoothing effect of the current approach on the interface as well as computational cost. Subsequently, two flow configurations serve to study the fully coupled problem: one is an underwater explosion problem with relatively simple interface evolution; the other is a shock–bubble interaction problem with complex interface evolution. Finally, we conduct a numerical simulation of liquid filament breakup to verify mesh convergence and physical sensibility of the present method. Here, the non-resolved interface segments are simply deleted after they are separated from the main interface. One can refer Han et al. [10] for alternative treatments.

4.1. Two-dimensional single-vortex flow

We consider a pure interface-transport case, where the interface deforms by a single-vortex flow [1]. A circle of radius $R_0 = 0.15$ is located at $(0.5, 0.75)$ in a unit square computational domain, as shown in Fig. 4 at the initial time. To compare the results with those in Ref. [10], the same grid resolution is set as 512×512. The velocity field is given by

$$\begin{aligned} u &= 2\sin^2(\pi x)\sin(\pi y)\cos(\pi y) \\ v &= -2\sin^2(\pi y)\sin(\pi x)\cos(\pi x). \end{aligned} \tag{16}$$

Under this solenoidal velocity field, the circular interface is stretched into a long filament around the vortex center.

Fig. 4 compares the evolution of the interface to that obtained by the constrained stimulus–response procedure of Ref. [10] (denoted as CSRP) and the level-set method without scale separation. In the early stage, since the interface is well-resolved, the three results coincide. After the interface has deformed, a thin filament appears at the cusp. The scale separation procedure is active when the length scale of the interface structure is less than the threshold (ε). As shown in Fig. 4, CSRP removes more interface segments or area at the cusp than the present method, since the level set values of some cells containing well-resolved interface segments are also updated by the re-initialization [10]. The area loss can be measured by

$$\frac{A}{A^0} = \frac{\Sigma_{i=0}^{i=N} \alpha_i^t}{\Sigma_{i=0}^{i=N} \alpha_i^0}. \tag{17}$$

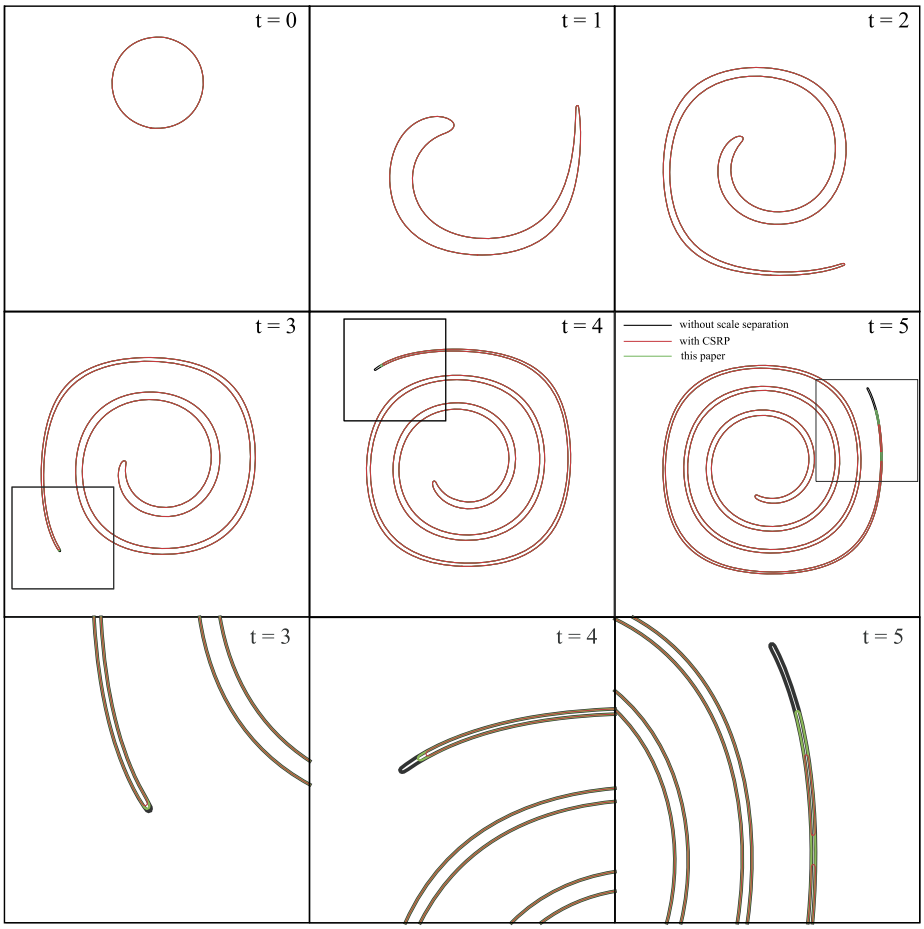

Fig. 4. Single-vortex flow: the evolution of interface deformation (first and second row) without scale separation (black line) and with CSRP (red line), and the method in this paper (green line). The third row shows zooms of the interfaces as indicated at times $t = 3,\ 4$ and 5. (For interpretation of the references to color in this figure legend, the reader is referred to the web version of this article.)

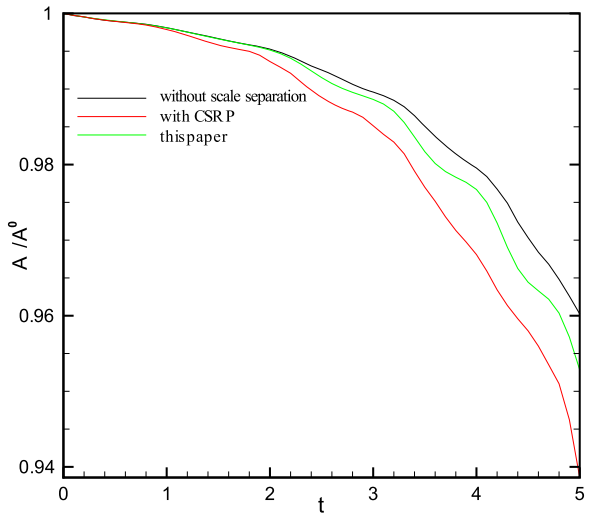

Fig. 5. Single-vortex flow: variation of the total area.

where A denotes the total area of the disk and α_i is the cell area on cell i, and the superscript 0 represents the initial condition. The results given in Fig. 5 show that the present method achieves less area loss than the CSRP. Furthermore, our experiment shows that the present method achieves a speed up factor of 2.3 compared to the CSRP method for the scale-separation operations.

Note that, since the level-set method generally lacks area/volume conservation, the area/volume loss is inevitable even when the flow is incompressible and the interface is well resolved. However, if the level-set method is coupled with the

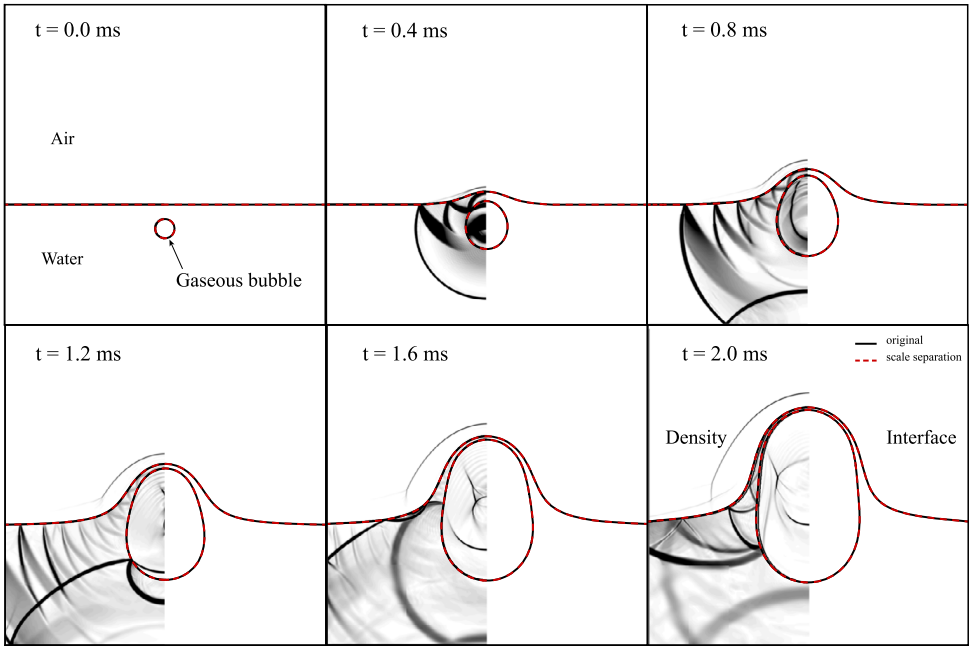

Fig. 6. Underwater explosion: Schlieren-type image for density (the left half) and interface position (the right half) at different time instances.

conservative sharp-interface method (see Ref. [21] and Sec. 4.4), area/volume conservation can be achieved due to the inherent mass-conservation property.

4.2. Underwater explosion

To demonstrate that the present method has no effect on the well-resolved interface structure, we carry out a two-dimensional simulation of an underwater-explosion problem. This case has been investigated by Hu et al. [16], Han et al. [9,10], and Shyue [28]. For this case, the non-dimensional initial condition is

$$\begin{cases} \rho = 1.2 \times 10^{-3}, u = 0, v = 0, p = 1, \gamma = 1.4 & \text{air} \\ \rho = 1.25, u = 0, v = 0, p = 1, \gamma = 1.4 & \text{gaseous bubble} \\ \rho = 1, u = 0, v = 0, p = 1, p_0 = 1, B = 3310, \gamma = 7.15, & \text{water} \\ \varphi = \begin{cases} 1.5 - y & y > 1.35 \\ -0.12 + \sqrt{(x-2)^2 + (y-1.2)^2} & y \le 1.35 \end{cases} & \text{level-set} \end{cases} . \tag{18}$$

The dimensional references are given by the state of water at 1 atmosphere and length scale 1 m. The level set $\varphi > 0$ represents water described by a Tait's equation of state, and $\varphi < 0$ represents air and the gaseous explosive products described by an ideal-gas equation of state. An underwater gaseous bubble of radius 0.12 is located at $(2, 1.2)$ in a rectangular domain 4×4, and the air–water interface is at $y = 1.5$. A solid-wall boundary is applied at the bottom and an outflow condition with zero gradient is applied at the other boundaries. The computational domain is discretized by 1024×1024 grid points, which is the same as in Ref. [9].

Fig. 6 shows the interface evolution as well as Schlieren-type images of density at several different time instances. The results are identical to those in Ref. [9]. As shown in Fig. 6, one can observe that, since the interface is smooth and well-resolved, no interface segments are removed by the present scale separation method. Compared to the CSRP method, our results show that the present method achieves a speed up factor of 2.5.

4.3. Shock–bubble interaction

To validate the present method with respect to handling complex interfaces, we consider a shock–bubble interaction problem. This case involves a weak shock wave of Mach 1.22 in air impacting a cylindrical bubble of Refrigerant-22 (R22), which is a canonical test for multi-phase numerical methods [9,24,26,29]. The corresponding experiments were carried out by Haas and Sturtevant [8]. With dimensional references given by the state of air at 1 atmosphere and 1 m, the initial condition is

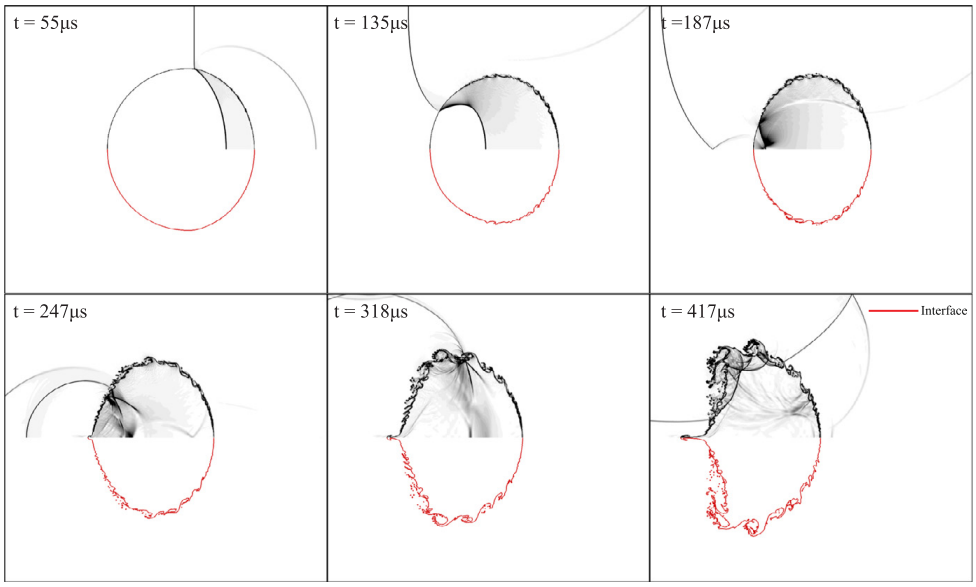

Fig. 7. Shock–bubble interaction: Schlieren-type images of density (the top half) and interface position (the bottom half) at different time instances.

$$\begin{cases} \rho = 1, u = 0, v = 0, p = 1, \gamma = 1.4 & \text{pre-shocked air} \\ \rho = 1.3764, u = -0.3947, v = 0, p = 1.5698, \gamma = 1.4, & \text{post-shocked air} \\ \rho = 3.154, u = 0, v = 0, p = 1.0, \gamma = 1.249, & \text{R22 bubble} \\ \varphi = -0.025 + \sqrt{(x - 0.245)^2 + y^2} & \text{level-set} \end{cases}. \tag{19}$$

The level set $\varphi > 0$ represents air and $\varphi < 0$ represents R22 respectively. Both are described by ideal-gas equation of state. A R22 bubble of radius 0.25 is located at $(0.245, 0.0445)$ in a rectangular domain 0.445×0.089. An incident shock wave, initially at $x = 0.295$, travels from right to left and interacts with the $R22$ bubble. To compare the current results with those in Ref. [10], the computational domain is discretized by the same grid with 8192×2048 points, where 1150 cells are distributed along the bubble diameter.

Fig. 7 shows the Schlieren-type images of density gradient $|\Delta\rho|$ at the several time instants. It can be observed that the results are in good agreement with previous numerical work of Refs. [9,24,26,29] and the experiment [8]. In the early stage, the interface is well-resolved as same as in Ref. [9,10]. Due to the vorticity induced by incident shock impact, the interface begins to roll up and produces small filaments, as shown in Fig. 7 at $t = 187{,}247$ μs. As time moves on, the filaments become thin and breakup into droplets. When these filaments are non-resolved by the current resolution grids, they are removed by the scale separation procedure. Compared with the results in Fig. 8 of Ref. [10], more droplets and thin filaments are preserved at the late stage, e.g. $t = 318{,}417$ by the present method. Furthermore, the present method achieves a speed up factor of 2.7. Note that, when the scale separation is switched off, numerical instability prevents the simulation from continuing after small filaments and droplets have been generated.

4.4. Liquid-filament breakup under gravity

To verify the ability of the present method on capturing the behavior near interface singularity, we consider a case of liquid-filament breakup under gravity and capillary effects. This problem has been studied both experimentally [32,3] and numerically [25,30,10]. The set-up of the simulation is the same as in Ref. [25] but the surface-tension coefficient is increased to $\sigma = 225$ to reduce computation cost. As pointed out by Castrejon-Pita et al. [3], the effect of air around the filament can be neglected.

A conservative sharp interface method for incompressible multiphase flows [22] is applied. The surface tension term $\mathbf{a}_s$ and gravity term $\rho\mathbf{g}$ are added in the momentum equation of Eq. (1). The surface-tension force is given by

$$\mathbf{a}_s = \sigma\kappa\delta_n\mathbf{N} \tag{20}$$

where σ, κ, $\mathbf{N}$ are surface-tension coefficient, curvature and normal direction of the interface, respectively. δ_n is a Dirac delta function defined in the normal direction of the interface. The initial condition for the axisymmetric liquid drop is given by

$$\begin{cases} \rho = 10^3, u = 0, v = 0, p_0 = 10^4, B = 10^5, \gamma = 7.15, & \text{Liquid} \\ \varphi = -0.25 + \sqrt{x^2 + (z - 3.0)^2} & \text{level-set} \end{cases}. \tag{21}$$

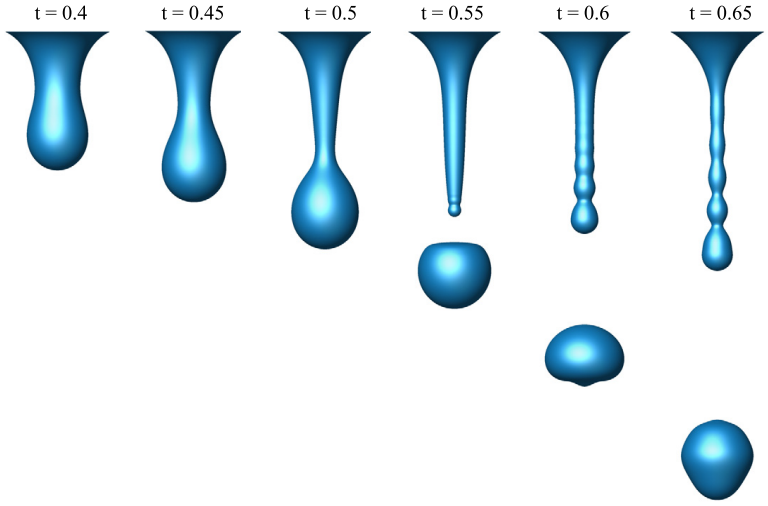

Fig. 8. Liquid-filament breakup: evolution of the interface.

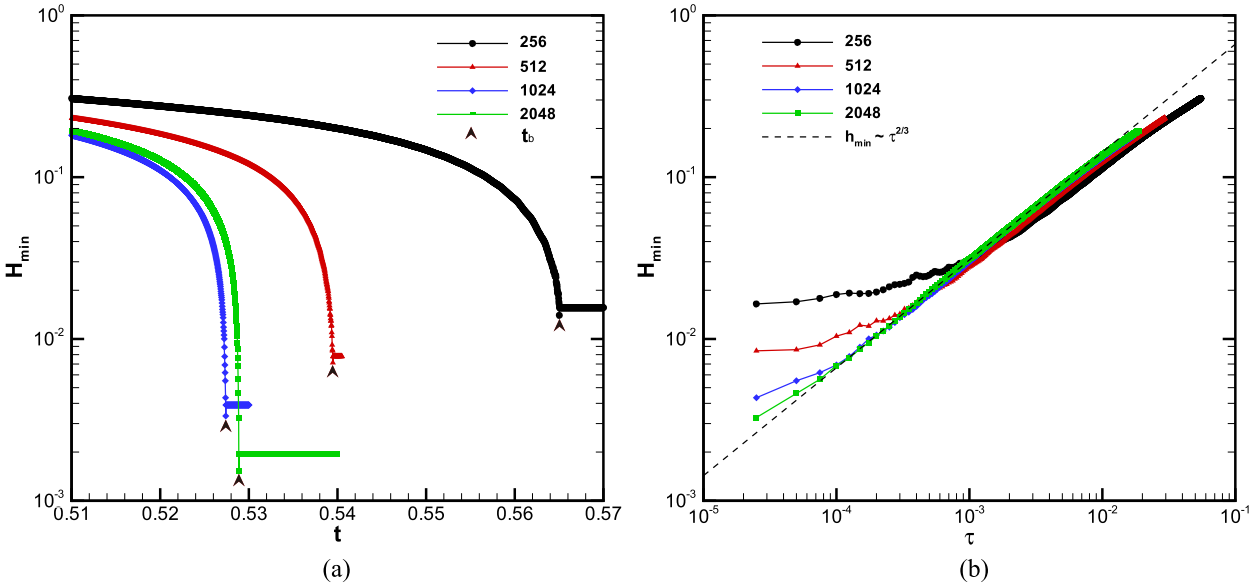

Fig. 9. Liquid-filament breakup at different resolutions: (a) evolution of the neck diameter h_{min} with time t; (b) evolution of h_{min} with the dimensionless time τ and the potential flow scaling law $h_{min} \sim \tau^{2/3}$.

The level set $\varphi < 0$ represents liquid drop described by a Tait's equation of state, and $\varphi < 0$ represents air which is neglected by the free surface model. The drop radius is 0.25 m with its center located at $(0.0, 3.1)$ in a axisymmetric domain of 0.5×3.0, g 25 m/s^2. The cap initially rests on the upper wetting wall due to surface tension. To handle the moving contact line, we adopt the effective curvature boundary condition at the wall [21]. The static contact angle is taken as $\theta = 25°$. In order to investigate grid convergence, the computational domain is discretized by increasing the resolution from 256×1536 to $2048 \times 12{,}288$.

Fig. 8 shows the interface at several time instants of the simulation with the resolution 1024×6144. As reported in Ref. [25], the liquid cap is quickly distorted but still is attached to the wall due to surface tension ($t = 0.4$). Subsequently, the drop deforms and a filament appears ($t = 0.45, 0.5$). When the thickness of the filament neck reduces to the size of about one cell, the scale separation method takes effect and the filament breaks up into two parts ($t = 0.55$). While the lower part is falling down and recovers to a circular shape, the upper part develops the typical shape for second breakup due to the capillary waves acting on the surface of the filament ($t = 0.6, 0.65$).

The evolution of the neck diameter is shown in Fig. 9. Since the Ohnesorge number $Oh = \mu/\sqrt{\rho R^3 \sigma} \ll 1$ in this case, it is expected that the dynamics follows potential-flow theory when h_{min} becomes sufficiently small, i.e. $h_{min} \sim \tau^{2/3}$ [20]. h_{min} is the neck diameter normalized with the drop radius R. τ is defined as $\tau = t - t_b$, where t is time, and t_b is the breakup time non-dimensionalized by the capillary time, $t_c = \sqrt{\rho R^3/\sigma}$. Fig. 9(a) illustrates the breakup times with different resolution, which implies about second order convergence with mesh refinement. Furthermore, the results recover the expected potential-flow scaling law, as shown in Fig. 9.

5. Concluding remarks

We have developed a new formulation for scale separation to improve the computational efficiency for multi-scale sharp interface modeling of multi-phase flows. Based on the observation that there is lack of topological consistency between the auxiliary and zero level-sets for the non-resolved interface segments, the cut cell associated with non-resolved interface segments are identified explicitly by checking the auxiliary cut cells in its neighborhood. Non-resolved structures are removed and the corresponding level-set field is reconstructed by a localized re-distancing method. Several typical numerical examples are simulated to validate the performance of the present scale separation method. The results show that the current approach is able to handle complex interface evolution. Compared to Han et al. [10], the present method decreases the over-smoothing effect of the original method and achieves a considerable computational speed up. Furthermore, the simulations of the filament-breakup case on with increasing grid resolutions verifies the physical consistency of the present scale-separation method.

Acknowledgements

The first author has partially been financed by China Scholarship Council (No. 2010629044).

References

[1] John B. Bell, Phillip Colella, Harland M. Glaz, A second-order projection method for the incompressible Navier–Stokes equations, J. Comput. Phys. 85 (2) (1989) 257–283.
[2] N. Bremond, E. Villermaux, Atomization by jet impact, J. Fluid Mech. 549 (1) (February 2006) 273.
[3] J.R. Castrejón-Pita, A.A. Castrejón-Pita, E.J. Hinch, J.R. Lister, Ian M. Hutchings, Self-similar breakup of near-inviscid liquids, Phys. Rev. E 86 (1) (2012) 15301.
[4] Gilberto Contreras, Margaret Martonosi, Characterizing and improving the performance of Intel threading building blocks, in: IEEE International Symposium on Workload Characterization, 2008, IISWC 2008, IEEE, 2008, pp. 57–66.
[5] Douglas Enright, Ronald Fedkiw, Joel Ferziger, Ian Mitchell, A hybrid particle level set method for improved interface capturing, J. Comput. Phys. 183 (1) (2002) 83–116.
[6] Ronald P. Fedkiw, Tariq Aslam, Barry Merriman, Stanley Osher, A non-oscillatory eulerian approach to interfaces in multimaterial flows (the ghost fluid method), J. Comput. Phys. 152 (2) (1999) 457–492.
[7] Daniel Fuster, Gilou Agbaglah, Numerical simulation of droplets, bubbles and waves: state of the art, Fluid Dyn. Res. 41 (6) (December 2009) 065001.
[8] J.F. Haas, B. Sturtevant, Interaction of weak shock waves with cylindrical and spherical gas inhomogeneities, J. Fluid Mech. (1987) 41–76.
[9] L.H. Han, X.Y. Hu, N.A. Adams, Adaptive multi-resolution method for compressible multi-phase flows with sharp interface model and pyramid data structure, J. Comput. Phys. 262 (April 2014) 131–152.
[10] L.H. Han, X.Y. Hu, N.A. Adams, Scale separation for multi-scale modeling of free-surface and two-phase flows with the conservative sharp interface method, J. Comput. Phys. 280 (January 2015) 387–403.
[11] Babak Hejazialhosseini, Diego Rossinelli, Michael Bergdorf, Petros Koumoutsakos, High order finite volume methods on wavelet-adapted grids with local time-stepping on multicore architectures for the simulation of shock–bubble interactions, J. Comput. Phys. 229 (22) (2010) 8364–8383.
[12] M. Herrmann, Refined level set grid method for tracking interfaces, Annual Research Briefs, Center for Turbulence (2005).
[13] M. Herrmann, A balanced force refined level set grid method for two-phase flows on unstructured flow solver grids, J. Comput. Phys. 227 (4) (2008) 2674–2706.
[14] M. Herrmann, A parallel Eulerian interface tracking/Lagrangian point particle multi-scale coupling procedure, J. Comput. Phys. 229 (3) (February 2010) 745–759.
[15] Marcus Herrmann, On simulating primary atomization using the refined level set grid method, At. Sprays 21 (4) (2011) 283.
[16] X.Y. Hu, N.A. Adams, G. Iaccarino, On the HLLC Riemann solver for interface interaction in compressible multi-fluid flow, J. Comput. Phys. 228 (17) (2009) 6572–6589.
[17] X.Y. Hu, B.C. Khoo, N.A. Adams, F.L. Huang, A conservative interface method for compressible flows, J. Comput. Phys. 219 (2) (2006) 553–578.
[18] X.Y. Hu, N.A. Adams, M. Herrmann, G. Iaccarino, Multi-scale modeling of compressible multi-fluid flows with conservative interface method, in: Proceedings of the Summer Program, 2010, p. 301.
[19] G.S. Jiang, C.W. Shu, Efficient implementation of weighted eno schemes, J. Comput. Phys. 126 (1996) 202–228.
[20] John R. Lister, Howard A. Stone, Capillary breakup of a viscous thread surrounded by another viscous fluid, Phys. Fluids 10 (11) (1998) 2758–2764.
[21] J. Luo, X.Y. Hu, N.A. Adams, A curvature boundary condition for moving contact line (2015), submitted for publication.
[22] J. Luo, X.Y. Hu, N.A. Adams, A conservative sharp interface method for incompressible multiphase flows, J. Comput. Phys. 284 (March 2015) 547–565.
[23] Francesco Miniati, Phillip Colella, Block structured adaptive mesh and time refinement for hybrid, hyperbolic n-body systems, J. Comput. Phys. 227 (1) (2007) 400–430.
[24] Robert R. Nourgaliev, Truc-Nam Dinh, Theo G. Theofanous, Adaptive characteristics-based matching for compressible multifluid dynamics, J. Comput. Phys. 213 (2) (2006) 500–529.
[25] G. Perigaud, R. Saurel, A compressible flow model with capillary effects, J. Comput. Phys. 209 (1) (2005) 139–178.
[26] Shiv Kumar Sambasivan, H.S. UdayKumar, Sharp interface simulations with local mesh refinement for multi-material dynamics in strongly shocked flows, Comput. Fluids 39 (9) (2010) 1456–1479.
[27] Chi-Wang Shu, Stanley Osher, Efficient implementation of essentially non-oscillatory shock-capturing schemes, J. Comput. Phys. 77 (2) (1988) 439–471.
[28] Keh-Ming Shyue, A wave-propagation based volume tracking method for compressible multicomponent flow in two space dimensions, J. Comput. Phys. 215 (1) (2006) 219–244.
[29] K.K. So, X.Y. Hu, N.A. Adams, Anti-diffusion interface sharpening technique for two-phase compressible flow simulations, J. Comput. Phys. 231 (11) (2012) 4304–4323.
[30] Youngho Suh, Gihun Son, A sharp-interface level-set method for simulation of a piezoelectric inkjet process, Numer. Heat Transf., Part B, Fundam. 55 (4) (2009) 295–312.
[31] Mark Sussman, Elbridge Gerry Puckett, A coupled level set and volume-of-fluid method for computing 3d and axisymmetric incompressible two-phase flows, J. Comput. Phys. 162 (2) (2000) 301–337.
[32] D.R. Webster, E.K. Longmire, Jet pinch-off and drop formation in immiscible liquid–liquid systems, Exp. Fluids 30 (1) (2001) 47–56.